



NTNU – Trondheim
Norwegian University of
Science and Technology

Impeller Stage Instabilities

Håvard S Skjefstad

Master of Science in Mechanical Engineering

Submission date: June 2015

Supervisor: Lars Eirik Bakken, EPT

Norwegian University of Science and Technology
Department of Energy and Process Engineering

EPT-M-2015-81

MASTER THESIS

for

Student Håvard Skjefstad

Spring 2015

Impeller Stage Instabilities*Ustabilitet i Løpehjulstrinn***Background and objective**

Major challenges are related to efficient utilization of existing infrastructure and exploration of new fields in the North Sea. Increased production of gas demands new field development based on sub-sea production, including bulk separation and wet gas compression. The wet gas compression represents an energy-intensive production segment in which limited research has been invested. Specifically this relates to the wet gas compression fundamentals.

In order to reveal the wet gas compressor performance fundamentals it is of vital importance to develop models and validate experimental test data from the NTNU test rig. The compressor and system behaviour under unsteady operating conditions have to be explored and analysed.

The following tasks are to be considered:

Based on literature review and experimental work at the wet gas compressor rig focus is given to the impeller stage instabilities. Of specific interest is the impeller flow regime, fluid accumulation and back flow phenomena at the inlet tip area. This relates both to dry and wet operating conditions.

1. Based on tests establish and document the flow regime at the impeller inlet tip area.
2. From literature and experiments establish secondary flow phenomena within the impeller channels. Any flow separation and/or boundary layer impact at low flow conditions are of specific interest.
3. Document interactions between the inlet pipe, impeller and diffuser at low flow conditions.

-- ” --

Within 14 days of receiving the written text on the master thesis, the candidate shall submit a research plan for his project to the department.

When the thesis is evaluated, emphasis is put on processing of the results, and that they are presented in tabular and/or graphic form in a clear manner, and that they are analyzed carefully.

The thesis should be formulated as a research report with summary both in English and Norwegian, conclusion, literature references, table of contents etc. During the preparation of the text, the candidate should make an effort to produce a well-structured and easily readable report. In order to ease the evaluation of the thesis, it is important that the cross-references are correct. In the making of the report, strong emphasis should be placed on both a thorough discussion of the results and an orderly presentation.

The candidate is requested to initiate and keep close contact with his/her academic supervisor(s) throughout the working period. The candidate must follow the rules and regulations of NTNU as well as passive directions given by the Department of Energy and Process Engineering.


Risk assessment of the candidate's work shall be carried out according to the department's procedures. The risk assessment must be documented and included as part of the final report. Events related to the candidate's work adversely affecting the health, safety or security, must be documented and included as part of the final report. If the documentation on risk assessment represents a large number of pages, the full version is to be submitted electronically to the supervisor and an excerpt is included in the report.

Pursuant to "Regulations concerning the supplementary provisions to the technology study program/Master of Science" at NTNU §20, the Department reserves the permission to utilize all the results and data for teaching and research purposes as well as in future publications.

The final report is to be submitted digitally in DAIM. An executive summary of the thesis including title, student's name, supervisor's name, year, department name, and NTNU's logo and name, shall be submitted to the department as a separate pdf file. Based on an agreement with the supervisor, the final report and other material and documents may be given to the supervisor in digital format.

- Work to be done in lab (Water power lab, Fluids engineering lab, Thermal engineering lab)
 Field work

Department of Energy and Process Engineering, 14. January 2015



Olav Bolland
Department Head



Lars E Bakken
Academic Supervisor

Research Advisors:
Veronica Ferrara
Øyvind Hundseid
Tor Bjørge

ABSTRACT

Since the discovery of Ekofisk in 1969 the Norwegian petroleum industry has been an important part of Norway's economical growth and industrial development. Today, Norway is the third largest gas exporter in the world, and the growth in gas production is expected to continue.

To ensure continued growth and sustainability of the Norwegian oil and gas industry, recovery rate from existing fields must be increased, and development of smaller, more remote discoveries, must be made profitable. This requires development of new cost effective extraction solutions.

Wellstream boosting allows for enlarged output rates, prolonged operation and increased transport distances. The reservoir streams are characterized by a low liquid content of 0-5% on a volume basis, rendering the use of traditional dry gas compressors unfavourable. For this reason, ongoing research aims to develop a compressor capable of operating in wet conditions while maintaining satisfactory performance and operational range.

This thesis documents compressor stage instabilities for a low pressure ratio, one-stage air-water multiphase centrifugal compressor. A detailed investigation of instability onset has been carried out, and the effect wet gas operation inflicts on occurring phenomena has been thoroughly documented. Volute pressure buildup appears as an initiating factor for dry gas instability, as a stationary stall region is observed prior to surge onset. Addition of a liquid phase has been found to delay instability onset, which is characterized by a direct transition into modified surge. Possible effects causing a delayed onset has been investigated, including phase segregation in the impeller channels and a delayed pressure buildup in the volute circumference. The previously documented phenomenon of an annulus ring of liquid forming at impeller inlet prior to instability onset in wet conditions has been further investigated, showing a significant impact of labyrinth leakage on detected inlet flow phenomenon.

SAMMENDRAG

Den norske petroleumsindustrien har siden oppdagelsen av Ekofisk i 1969 vært svært viktig for Norges økonomiske vekst og industrielle framskritt. Norge er i dag verdens 3. største eksportør av gass, og mengden eksportert gass er forventet å øke i årene framover.

For å sikre en framtidig vekst i den Norske olje- og gassnæringen er det viktig med kontinuerlige framskritt. Utviklingen av fjerntliggende, mindre felter må bli gjort lønnsomt, samt at utvinningsgraden må økes for felt i produksjon. Dette krever utvikling av nye og mer effektive ekstraksjonsløsninger.

En foreslått løsning er å komprimere brønnstrømningen på havbunnen, noe som vil resultere i økt utvinninggrad samt mulighet for lengre transportdistanser. Brønnstrømmer er kjent for å inneholde en liten del væske, 0-5% på en volumbasis, noe som gjør at bruken av tradisjonelle tørrgasskompressorer er ugunstig. Det er derfor iverksatt et pågående forskningsprosjekt som har til hensikt å utvikle en kompressor som kan operere under våte forhold, samtidig som den opprettholder tilfredstillende ytelse og arbeidsområde.

Denne oppgaven dokumenterer ustabilitetsfenomener som oppstår i en lavtrykks-sentrifugalkompressor. Kompressoren er en en-steps maskin, og komprimerer en flerfaseblanding bestående av luft og vann. Det har blitt gjennomført en grundig undersøkelse av forekommende tørrgass-ustabilitetsfenomener, samt hvordan disse blir påvirket av et skifte til våtgassstrømning. En stasjonær ustabilitetsregion har blitt observert ved innsuget til løpehjulet, noe som indikerer en trykkoppbygning i spiraltrømmen som opphav til ustabiliteten. En utsatt oppstart av ustabilitet er dokumentert for våtgasskompresjon, som viste en direkte overgang til modifisert surge. Bakgrunnen for den utsatte ustabiliteten har blitt undersøkt, og en dokumentert faseegresjon i løpehjulskanalen samt en indikert senere trykkoppbygning i spiraltrømmen er av interesse. Dannelsen av en væskering ved innsuget til løpehjulet er et tidligere dokumentert fenomen i forbindelse med våtgass-ustabilitet. Dette fenomenet har blitt videre undersøkt, og resultater viser at lekkasje fra labyrinttetningen har en betydelig påvirkning.

Where oil is first found is in the minds of men

— Wallace Pratt

ACKNOWLEDGEMENTS

The work presented in this thesis has been performed at the Norwegian University of Science and Technology, Department of Energy and Process Engineering, spring 2015. This thesis is a continuation of my previous project thesis, and concludes my NTNU Master of Science degree program.

I would like to thank my supervisor Professor Lars E. Bakken for great consultation throughout my final year. I would also like to thank my co-supervisors Veronica Ferrara and Øyvind Hundseid for invaluable help and input during the semester.

In addition, I would like to thank Engineer Erik Langørgen for his great insight and shared experience regarding the NTNU wet gas compressor rig.

At last I would like to thank my fellow students, Martin Bakken, Sindre Garpestad Tønnessen and Harald Relling Nielsen for a great work environment and many interesting discussions.

Håvard Slettahjell Skjefstad,
June 10, 2015

CONTENTS

i	INTRODUCTION AND TEST RIG SPECIFICATIONS	1
1	INTRODUCTION	3
1.1	Background and motivation	3
1.2	Multiphase flow	4
1.2.1	Advantages	6
1.2.2	Challenges	6
1.2.3	Previous work	7
1.3	Project scope	7
1.4	Report structure	8
2	TEST RIG	9
2.1	Specifications	9
2.2	Instrumentation	11
ii	THEORY AND LITERATURE REVIEW	13
3	CENTRIFUGAL COMPRESSOR FLOW DYNAMICS	15
3.1	Boundary layer theory	16
3.1.1	Boundary layer separation	18
3.2	Impeller channel flow	19
3.2.1	Force balance	19
3.2.2	Secondary flow	22
3.2.3	Slip	24
3.2.4	Multiphase effects	26
3.3	Vaneless diffuser	28
3.3.1	Flow analysis	28
3.3.2	Multiphase effects	31
3.4	Volute	32
3.4.1	Multiphase effects	34
3.5	Component interaction	35
3.6	Summary and test rig considerations	36
4	CENTRIFUGAL COMPRESSOR INSTABILITIES	39
4.1	Stall	39
4.2	Surge	42
4.3	Shock formation	44
4.4	Multiphase effects	45
4.5	Summary and test rig considerations	45
5	FLOW VISUALIZATION TECHNIQUES	47
5.1	Pressure sensors	47
5.1.1	Static pressure sensors	47
5.1.2	Differential pressure sensors	47

5.1.3	Multi-hole probes	48
5.1.4	High-response pressure sensors	48
5.1.5	Test rig installations	49
5.2	Direct visualization	49
5.2.1	Foreign material injection	50
5.2.2	Thread attachment	50
5.2.3	Stroboscope	50
5.2.4	Test rig installations	50
5.3	Coating	51
5.4	Other techniques	51
5.4.1	Optical techniques	51
5.4.2	Vibroacoustic measurements	52
iii	TEST DESIGN AND EXPERIMENTAL RESULTS	53
6	EXPERIMENTAL SETUP AND PROCEDURE	55
6.1	3-hole probe measurements	55
6.1.1	Accuracy	57
6.2	Thread attachment	59
6.3	High-response pressure readings	60
6.4	Impeller coating	62
6.5	Labyrinth injection	63
6.6	Stroboscope and visual observation	66
7	EXPERIMENTAL RESULTS	69
7.1	Dry operation	70
7.1.1	Power spectral analysis	70
7.1.2	Instability classification	76
7.1.3	Flow regime	78
7.2	Wet operation	82
7.2.1	Power spectral analysis	82
7.2.2	Multiphase flow regime	87
8	CONCLUSION AND RECOMMENDED WORK	97
8.1	Dry operation	97
8.1.1	Instability onset	97
8.1.2	Flow regime	97
8.2	Wet operation	98
8.2.1	Multiphase instability onset	98
8.2.2	Multiphase flow regime	98
8.3	Recommended further work	98
iv	APPENDIX	101
A	PIPE AND INSTRUMENTATION DIAGRAM	103
B	CALCULATIONS	105
B.1	Mass flow calculation	105
B.2	Volume flow calculation	106

B.3 Non dimensional flow coefficient calculation	106
C SENSOR ACCURACY	107
C.1 Differential pressure sensors	107
C.2 Remaining sensors	110
D CERTIFICATES	111
E GHANT CHART	115
F EXCERPT OF RISK ASSESSMENT REPORT	117
BIBLIOGRAPHY	119

LIST OF FIGURES

Figure 1	Historical production of oil and gas, and prognosis for production in coming years [10]	3
Figure 2	Distribution of oil resources and oil reserves in fields [10]	4
Figure 3	Flow regime map illustration for multiphase flow	6
Figure 4	Picture of compressor block	9
Figure 5	Overview of major rig components	10
Figure 6	Instrumental specification for compressor block .	11
Figure 7	Pressure and velocity through a centrifugal compressor [4]	15
Figure 8	Boundary layer formation on a flat plate	17
Figure 9	Separation of the boundary layer and vortex formation at a circular cylinder [34]	18
Figure 10	The geometry and accelerations of inviscid flow in a centrifugal impeller	21
Figure 11	Velocity triangles at impeller inlet and outlet . . .	23
Figure 12	Acceleration and deceleration of the fluid close to the shroud	23
Figure 13	Velocity measurements by Eckardt in a centrifugal unshrouded impeller with no backsweep [9] .	25
Figure 14	The formation of slip, and effect on outlet velocity triangle	26
Figure 15	The geometry and force components of inviscid flow in a centrifugal backswept impeller	27
Figure 16	Effect of segregated flow on gas phase velocity . .	28
Figure 17	Velocity triangle at the impeller outlet	30
Figure 18	The geometry of a volute surrounding a centrifugal compressor with a vaneless diffuser [9]	33
Figure 19	Indication of backflow regions between compressor components	35
Figure 20	Illustration of stall onset	40
Figure 21	Illustration of rotating impeller-stall propagation .	40
Figure 22	Illustration of rotating diffuser-stall propagation .	41
Figure 23	Centrifugal compressor characteristic, with illustrated deep surge cycle	43
Figure 24	Three hole probe perpendicular to flow direction .	48
Figure 25	Model of 3-hole probe	56
Figure 26	Absolute velocity components	58
Figure 27	Threads fitted at impeller inlet	59

Figure 28	Thread placement in diffuser top left section . . .	60
Figure 29	FFT of high response pressure signal acquired at 9000 rpm $\phi = 0.06$ at impeller outlet	61
Figure 30	Impeller after application of coating	63
Figure 31	Drilled hole in relation to labyrinth seal	64
Figure 32	Location of drilled hole	64
Figure 33	Fluorescent liquid container	65
Figure 34	illustration of impeller-diffuser gap width	66
Figure 35	Compressor characteristic at 9000 rpm [35]	69
Figure 36	High and low range power spectral analysis for $0.06 \geq \phi \geq 0.05$ at 9000 rpm, 100% GMF (im- peller outlet)	71
Figure 37	High and low range power spectral analysis for $0.04 \geq \phi \geq 0.03$ at 9000 rpm, 100% GMF (im- peller outlet)	72
Figure 38	Compressor pressure ratio and ϕ versus time for the operating range $0.04 \geq \phi \geq 0.03$ at 9000 rpm, 100% GMF	73
Figure 39	Low range power spectral analysis for $0.03 \geq \phi \geq$ 0.02 at 9000 rpm, 100% GMF (impeller outlet) . . .	73
Figure 40	Compressor pressure ratio and ϕ versus time for the operating range $0.03 \geq \phi \geq 0.02$ at 9000 rpm, 100% GMF	74
Figure 41	Low range power spectral analysis for $0.05 \geq \phi \geq$ 0.04 at 9000 rpm, 100% GMF (diffuser outlet) . . .	74
Figure 42	Low range power spectral analysis for $0.04 \geq \phi \geq$ 0.02 at 9000 rpm, 100% GMF (diffuser outlet) . . .	75
Figure 43	Spreading stationary stall region at inducer, 9000 rpm, 100% GMF	76
Figure 44	Completely spread stall region at inducer, 9000 rpm, 100% GMF	77
Figure 45	Detected diffuser instability at 9000 rpm, 100% GMF	78
Figure 46	Graphical representation of test points on the com- pressor characteristic at 9000 rpm, 100% GMF . . .	79
Figure 47	Three hole probe measurements of dynamic pres- sure and flow angle at impeller outlet, 9000 rpm, 100% GMF	80
Figure 48	Three hole probe measurements of dynamic pres- sure and flow angle at diffuser outlet, 9000 rpm, 100% GMF	81
Figure 49	High range power spectral analysis for $0.06 \geq$ $\phi \geq 0.05$ at 9000 rpm, 90% GMF (impeller out- let)	82

Figure 50	Low range power spectral analysis for $0.06 \geq \phi \geq 0.04$ at 9000 rpm, 90% GMF (impeller outlet) . . .	83
Figure 51	Low range power spectral analysis for $0.04 \geq \phi \geq 0.02$ at 9000 rpm, 90% GMF (impeller outlet) . . .	84
Figure 52	Compressor pressure ratio and ϕ versus time for the operating range $0.03 \geq \phi \geq 0.02$ at 9000 rpm, 90% GMF	85
Figure 53	Low range power spectral analysis for $0.05 \geq \phi \geq 0.04$ at 9000 rpm, 90% GMF (diffuser outlet)	85
Figure 54	Low range power spectral analysis for $0.04 \geq \phi \geq 0.02$ at 9000 rpm, 90% GMF (diffuser outlet)	86
Figure 55	Detected flow phenomenon and labyrinth leakage influence at impeller inlet in the operating range $0.05 \geq \phi \geq 0.03$ at 9000 rpm, 90%GMF . . .	88
Figure 56	Detected flow phenomenon and labyrinth leakage influence at impeller inlet in the operating range $0.028 \geq \phi \geq 0.022$ at 9000 rpm, 90%GMF . .	89
Figure 57	Inducer before and after 5 minute run at 6000 rpm, 90% GMF	91
Figure 58	Impeller inlet section after 5 minute run at 6000 rpm, 90% GMF	91
Figure 59	Impeller channel after 5 minute run at 6000 rpm, 90% GMF	92
Figure 60	Impeller outlet section before and after 5 minute run at 6000 rpm, 90% GMF	92
Figure 61	Stroboscope induced impeller outlet flow regime at 9000 rpm, 90% GMF	93
Figure 62	Diffuser flow regime at 9000 rpm, 90% GMF	94
Figure 63	Illustration of measurement errors	107
Figure 64	Illustration of measurement error range	109

LIST OF TABLES

Table 1	Instrumentation list	12
Table 2	Installed pressure probes and sensors	49
Table 3	Locations for flow angle and velocity measurements	56
Table 4	3-hole probe test matrix	57
Table 5	Differential pressure accuracy test results	57
Table 6	Calculation of flow angle measurement error	58
Table 7	Test matrix	62
Table 8	Injection test matrix	66
Table 9	Analysed frequency range	70
Table 10	Deviation in diffuser outlet dynamic pressure measurements	81
Table 11	Points on calibration curve (0-100 mbar)	108
Table 12	Points on calibration curve (100-500 mbar)	108
Table 13	Error estimation pressure values	109
Table 14	Differential pressure accuracy test results	110
Table 15	Sensor accuracy	110

NOMENCLATURE

ROMAN LETTERS

LETTER	DESCRIPTION	UNIT
A	Area	[m ²]
C	Absolute velocity	[m/s]
C _D	Volume flow coefficient	[-]
D	Diameter	[m]
F	Force	[N]
N	Number of measurements in a sample	[-]
P	Pressure	[Pa]
Q̇	Volumetric flow	[m ³ /s]
R	Radius of curvature	[m]
R	Specific gas constant	[J/KgK]
T	Temperature	[°C]
S	Separation point	[m]
U	Rotational velocity	[m/s]
V	Velocity	[m/s]
Y	Expansion factor	[-]
W	Relative velocity	[m/s]
X	Measured value	[m/s]
Z	Compressibility	[-]
a	Acceleration	[m/s ²]
b	Diffuser width	[m]
f	Impeller revolution frequency	[Hz]
m	Mass	[Kg]
ṁ	Mass flow	[Kg/s]
r	Radial distance from axis of rotation	[m]
s	Distance	[m]
t	Time	[s]
x	Distance in the x direction	[m]

y	Distance in the y direction	[m]
DR	Density ratio	[-]
Ma	Mach number	[-]
Re	Reynolds number	[-]
SF	Slip factor	[-]
VS	Superficial velocity	[m/s]

GREEK LETTERS

LETTER	DESCRIPTION	UNIT
α	Logarithmic spiral angle	[°]
β	Absolute velocity component angle	[°]
γ	Inclination of blade to blade surface to the axis of rotation	[°]
δ	Boundary layer thickness	[m]
ε	Error	[mbar]
ζ	Orifice to pipe diameter ratio	[-]
θ	Angular position	[-]
κ	Specific heat ratio	[-]
μ	Measurement mean	[mbar]
ν	Kinematic viscosity	[m ² /s]
σ	Standard deviation	[mbar]
ρ	Density	[kg/m ³]
ϕ	Non dimensional flow coefficient	[-]
ω	Angular velocity	[1/s]

SUBSCRIPTS

SUBSCRIPT	DESCRIPTION
A	Component indicator
B	Component indicator
R	Random

S	Systematic
g	Gas
j	Jet
l	Liquid
m	Mean
r	Radial direction
v	Volume corrected
w	Wake
air	Air
crit	Critical
gap	Gap
inj	Injection
ori	Orifice plate
pipe	Pipe
rel	Relative
stag	Stagnation
stat	Static
tot	Total
1	Impeller inlet
2	Impeller outlet
3	Diffuser outlet
4	Compressor outlet
θ	Radial direction
∞	Infinite distance away

ACRONYMS

ACRONYM	DESCRIPTION
ASME	American Society of Mechanical Engineers
BPF	Blade Passing Frequency
CFD	Computational Fluid Dynamics

FFT	Fast Fourier Transform
GDP	Gross Domestic Product
GMF	Gas Mass Fraction
GVF	Gas Volume Fraction
LDV	Laser Doppler Velocimetry
L2F	Laser-2-Focus Velocimetry
NOK	Norwegian kroner
NTNU	Norwegian University of Science and Technology
PIV	Particle Imaging Velocimetry
PXI	PCI Extensions for Instrumentation
PSP	Pressure Sensitive Paint
P&ID	Piping and Instrumentation Diagram
PMMA	Polymethyl methacrylate
RMS	Root Mean Square
UV	Ultraviolet
VSD	Variable Speed Drive
rpm	Revolutions Per Minute
rps	Revolutions Per Second

Part I

INTRODUCTION AND TEST RIG
SPECIFICATIONS

INTRODUCTION

1.1 BACKGROUND AND MOTIVATION

*Master Thesis -
Impeller Stage
Instabilities*

The discovery of Ekofisk in 1969 marks the beginning of the Norwegian oil era. Production from the field started in June 1971, and several large discoveries were made in the following years. Since production started, the industry has contributed approximately NOK 11000 billion to the Norwegian GDP and is Norway's largest industry measured in value creation, state revenues and export value [10]. Although production of oil has decreased since its peak in 2001, the demand and production of natural gas has increased. Today Norway is the third largest gas exporter in the world, producing more natural gas than oil, and the growth in production is expected to continue, see Figure 1.

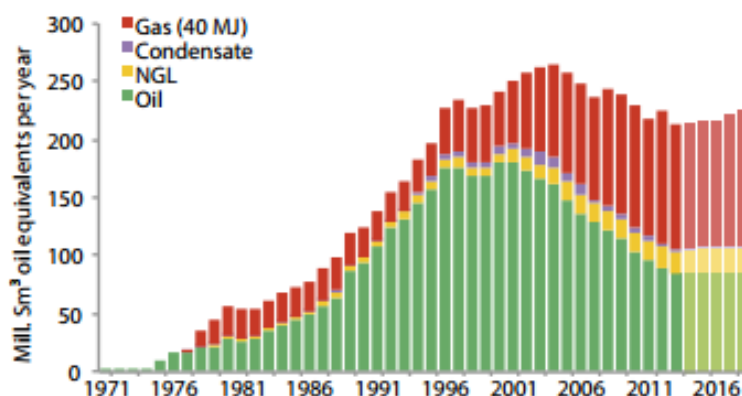


Figure 1: Historical production of oil and gas, and prognosis for production in coming years [10]

Now, more than 50 years after the discovery of Ekofisk, large parts of the North sea has been explored. New large discoveries are less likely, and the focus has shifted to improving recovery rate in producing fields as well as exploring for resources close to developed infrastructure.

Figure 2 gives an overview of the remaining resources in producing fields at planned cessation. It is clear that increasing the recovery rate has substantial value creation potential.

With the introduction of American shale oil the market has seen a significant increase in oil supply. The need to lower breakeven prices is imminent, and crucial to ensure continued growth and sustainability

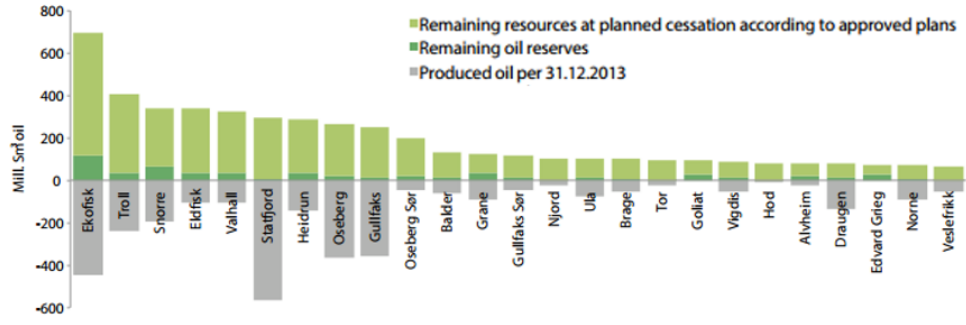


Figure 2: Distribution of oil resources and oil reserves in fields [10]

of the Norwegian oil and gas industry. New discoveries and efficient extraction solutions are essential, however, there are challenges to overcome. Many of the discoveries currently being considered for development are small. These fields do not support the construction of offshore platforms, and are dependant on existing infrastructure in order to become profitable. Discoveries are also being made in more remote areas, characterized by deep water and non existent infrastructure. These challenges has led to continued technology development, resulting in subsea processing. This allows for cost effective production and enables tie-ins to existing pipelines. Subsea solutions also enable direct transfer to onshore plants, removing the need for offshore processing entirely.

Common for both subsea transport and increased recovery rates is the need for subsea compression. Wellstream boosting allows for enlarged output rates, prolonged operation and increased transport distances. The reservoir streams are characterized by a low liquid content of 0-5% on a volume basis. This makes the use of traditional dry gas compressors inapt. For this reason, ongoing research aims to develop a compressor capable of operating in wet conditions while maintaining satisfactory performance levels.

1.2 MULTIPHASE FLOW

Wet gas is defined as gas containing up to 5% liquid on a volume basis. The gas volume fraction and gas mass fraction are given as:

$$\text{GVF} = \frac{\dot{Q}_g}{\dot{Q}_g + \dot{Q}_l} \quad (1)$$

$$\text{GMF} = \frac{\dot{m}_g}{\dot{m}_g + \dot{m}_l} \quad (2)$$

Another important parameter in multiphase flow is the slip factor SF. This denotes the velocity ratio between the phases and provides, along

with the density ratio DR, information on phase drag and expected flow regime.

$$SF = \frac{V_g}{V_l} \quad (3)$$

$$DR = \frac{\rho_g}{\rho_l} \quad (4)$$

The different multiphase flow regimes can be divided into four categories:

1. *Stratified flow*, characterized by a distinct horizontal phase separation. Common for low velocity systems where $DR \ll 1$, allowing gravitational forces to separate the phases.
2. *Annular flow*, characterized by a thin liquid film on the pipe wall and the lighter phase, with some liquid droplet entrainment, flowing in the pipe center. Common for systems with high GVF and dominating gas phase velocity, $SF \gg 1$, allowing gas turbulence to disperse the liquid into droplets.
3. *Slug flow*, characterized by a mixed flow regime where the gas phase exists as bubbles between sequential liquid "slugs".
4. *Bubble flow*, characterized by a dominant liquid phase, low GVF, and entrained gas bubbles. Common for horizontal multiphase flow.

Owing to low liquid concentration and high gas velocity, the expected flow regime in wet compression pipelines is *annular flow*. An overview of the different regimes, with corresponding superficial phase velocities, VS_g and VS_l , is illustrated in [Figure 3](#). VS_g and VS_l are given by:

$$VS_g = \frac{\dot{Q}_g}{A_{tot}}$$

$$VS_l = \frac{\dot{Q}_l}{A_{tot}}$$

where A_{tot} is the total pipe cross sectional area.

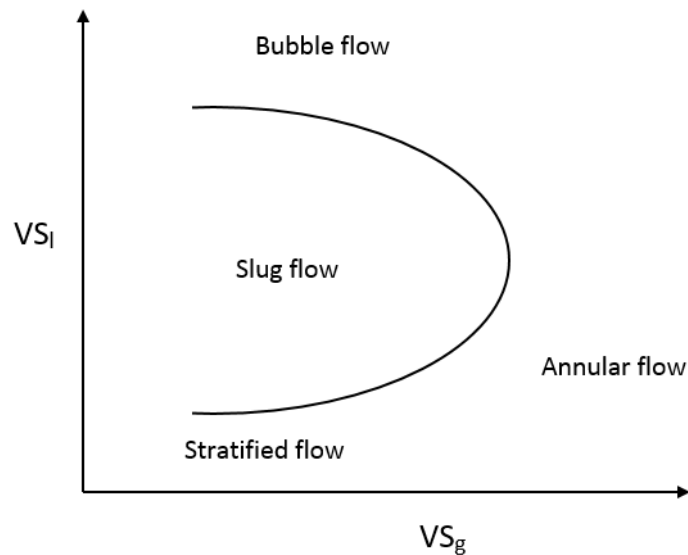


Figure 3: Flow regime map illustration for multiphase flow ¹

1.2.1 Advantages

The advantages of wet gas compression are many. The use of upstream separators and scrubbers are needed for dry gas compression. Installation of wet gas compressors would remove this need, reducing both the cost and size of compression packages. Size and complexity reduction is especially important for subsea installations, as these must operate for long periods of time without supervision. Brenne et al. [7] presented prospects for sub sea wet gas compression, mentioning advantages such as production flexibility, increased recovery rate and cost-effective exploitation of marginal gas/condensate fields.

1.2.2 Challenges

There are several challenges related to wet gas compression. The addition of a second phase modifies mixture density and friction effects. The density changes lead to compressibility variations which in turn affect compressor performance. In addition, phase interaction and heat transfer renders traditional calculation standards inadequate for performance determination.

Operational range and instability onset change with fluid composition. Current instability preventing installations are based on dry gas experiments, and knowledge of how liquid affect the compressor be-

¹ Based on illustrations and lecture notes from the subject TEP12 Multiphase flow.

haviour is crucial for designing new and effective damage preventing systems.

In order to design an efficient wet gas impeller with an acceptable operational range, detailed knowledge of wet gas impact on flow separation and flow regime variations through existing dry gas impellers is needed. This will further assist the ongoing research, and help to determine the validity of existing dry gas solutions.

1.2.3 Previous work

Prominent work has already been done in order to document wet gas influence on centrifugal compressor performance and instability. In 2005 Brenne et al. [6] evaluated the performance of a centrifugal compressor operating under wet gas conditions. Results showed an increase in pressure ratio but reduced polytropic efficiency at decreasing GVF's. Since then, several papers has been published on the subject. Hundseid et al. [21] witnessed significant polytropic head and efficiency reduction at decreasing GVF's. Fabbri et al. [12] displayed an initial pressure ratio increase, but a further decrease as GVF was reduced. The effect of droplet sizes on compressor performance was also investigated, showing that smaller droplets yielded less performance deterioration.

Grüner et al. [18] investigated airfoil performance in wet gas flow. Premature boundary layer separation was observed, resulting in degraded airfoil performance. This indicated premature instability onset under wet conditions. However, Grüner and Bakken [17] later observed an increased surge margin when liquid was present. Another significant discovery was the formation of an extending annulus ring of liquid forming at the impeller inlet prior to full surge. This phenomenon has been further documented by Ferrara et al. [13].

The authors previous work [35] documents wet gas effect on compressor performance and instability onset. Results displayed a decrease in polytropic efficiency at reduced GMF's, as well as a delayed instability onset under wet conditions. The occurring annulus ring of liquid forming prior to full surge was also thoroughly documented. Further investigation on flow regime and flow separation at low velocities are needed in order to fully understand wet gas effect on impeller stage instabilities.

1.3 PROJECT SCOPE

Based on literature review and experimental work at the NTNU wet gas compressor rig the goal of this thesis is to document impeller stage instabilities in both dry and wet conditions. Focus is given to impeller

flow regime, fluid accumulation and back flow phenomena at the impeller inlet tip area. The work is based on the following tasks:

1. *Based on tests establish and document the flow regime at the impeller inlet tip area.*
2. *From literature and experiments establish secondary flow phenomena within the impeller channels. Any flow separation and/or boundary layer impact at low flow conditions are of specific interest.*
3. *Document interactions between the inlet pipe, impeller and diffuser at low flow conditions.*

1.4 REPORT STRUCTURE

This thesis is constructed as a scientific report, divided in chapters, sections and subsections. A thorough literature review will be presented before moving on to test design and experimental results. The main contents of each chapter is summarized below.

- *Chapter 2* provides a detailed introduction to the NTNU wet gas test facility. All relevant rig specifications and installed instrumentation will be included.
- *Chapter 3* will discuss centrifugal compressor flow dynamics. Focus is given to prediction and explanation of occurring flow phenomena in the different components of a centrifugal compressor, as well as expected wet gas influence.
- *Chapter 4* includes a detailed review of known compressor instability phenomena, and their characteristics.
- *Chapter 5* presents different possibilities regarding flow visualization. Focus is given to techniques enabled by test rig specifications.
- *Chapter 6* gives an accurate description of all performed experiments and associated test procedures.
- *Chapter 7* presents this thesis' findings, and relates results to previously reviewed theory.
- *Chapter 8* concludes presented findings, and includes recommendations for further work.

TEST RIG

Results presented in this thesis are based on tests performed at the Norwegian University of Science and Technology's wet gas compressor rig. The rig was constructed in 2006 when NTNU and Statoil initiated a research program in order to document the influence of wet gas on centrifugal compressor operation.

2.1 SPECIFICATIONS

The NTNU wet gas compressor rig is a low pressure ratio one-stage air-water multiphase centrifugal compressor modified for wet gas operation. The test facility is an open loop configuration, where ambient air is compressed by a shrouded 17-blade backswept impeller. Prior to the impeller inlet, a water injection system is installed. The injection system consists of 16 nozzles mounted circumferentially around the inlet pipe, and is driven by a water pump. The installed diffuser is a vaneless straight walled diffuser, and a symmetrical circular volute with an increasing cross sectional area transports the fluid to the outlet pipe. A picture of the compressor block is given in [Figure 4](#).

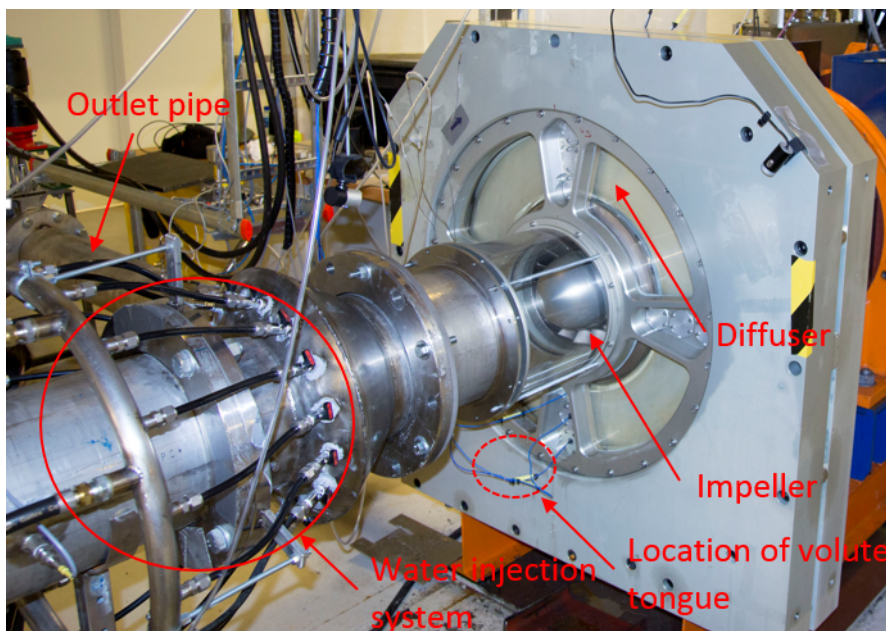


Figure 4: Picture of compressor block

The volute is designed for wet gas operation, and the cross sectional area is therefore reduced compared to similar dry gas installations. The volute discharge is at the bottom left of the compressor block, and the volute tongue's circumferential location is indicated in [Figure 4](#).

Power is supplied by an electric motor, capable of delivering up to 450 kW. The maximum speed is 11000 rpm and can be regulated by a variable speed drive system (VSD). A discharge throttle valve enables control of the compressor operating point. The flow enters the compressor axially, however, a variable inlet guide vane system can be added to induce prewhirl. [Figure 5](#) displays the main components of the rig, and how they are connected.

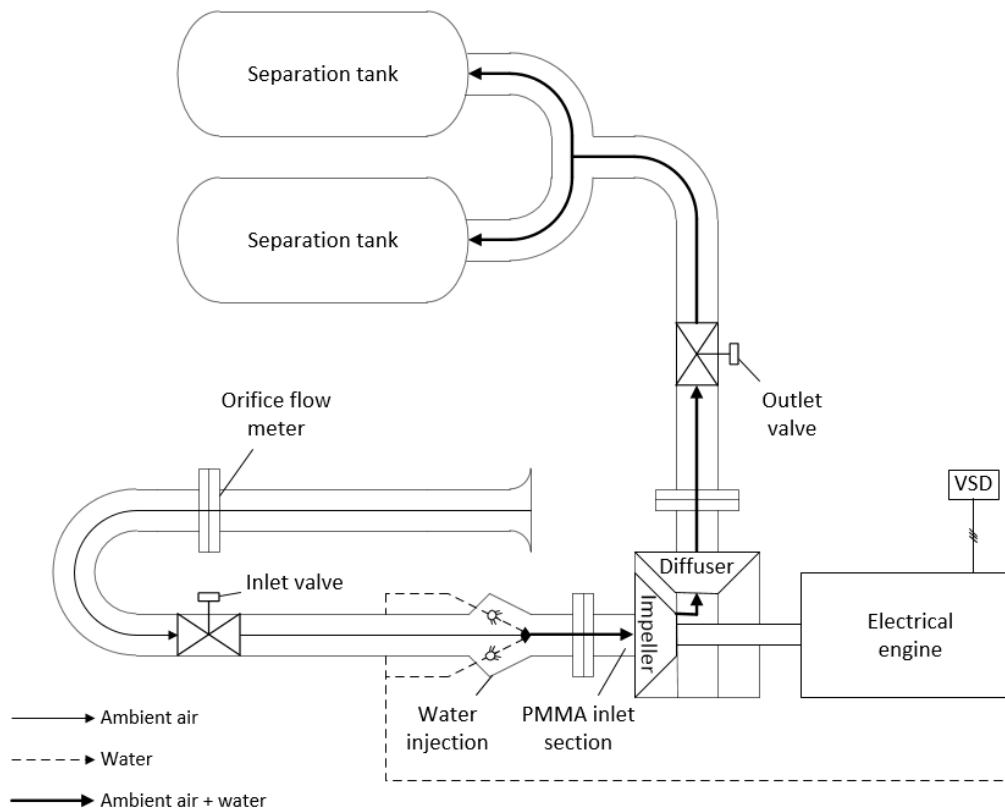


Figure 5: Overview of major rig components

To enable visualization of the inlet flow, a transparent thermoplastic (PMMA) inlet pipe-section is fitted at the impeller inlet. Sections of the same thermoplastic is also fitted in four different locations on the diffuser shroud wall, enabling visualization of the diffuser flow. The impeller PMMA inlet pipe-section is marked in [Figure 5](#) and all thermoplastic installations are visible in [Figure 4](#).

There are several risks involved with rig operation, and a thorough risk assessment has been performed alongside test rig development. An excerpt of the already developed risk assessment report is included in [Appendix F](#)

2.2 INSTRUMENTATION

The instrumentation setup is in accordance with *ASME PTC-10* standard [31]. The compressor characteristic is determined from static pressure and volume flow calculations. The volume flow is presented by the non dimensional flow coefficient ϕ . Static pressure is measured at compressor inlet and outlet, and the volume flow is calculated with an orifice plate located upstream of the compressor inlet. Four temperature sensors are mounted upstream and downstream of the compressor, allowing for accurate performance calculations. Calculation procedure for the volume flow and ϕ can be found in [Appendix B](#). Three high-response pressure sensors are flush mounted on the diffuser wall in order to document instability onset. One is located close to the impeller outlet, one in the middle of the diffuser and one at the diffuser outlet. The sensors are "High resolution ICP pressure sensors" with a natural frequency of 250 kHz and a low frequency response of 0.5 Hz. The diffuser wall is also fitted with flush mounted static pressure probes as well as 3-hole probes for flow angle measurement. These can be connected to four installed differential pressure sensors, enabling velocity determination in the diffuser. [Figure 6](#) displays the instrumental setup on the compressor block.

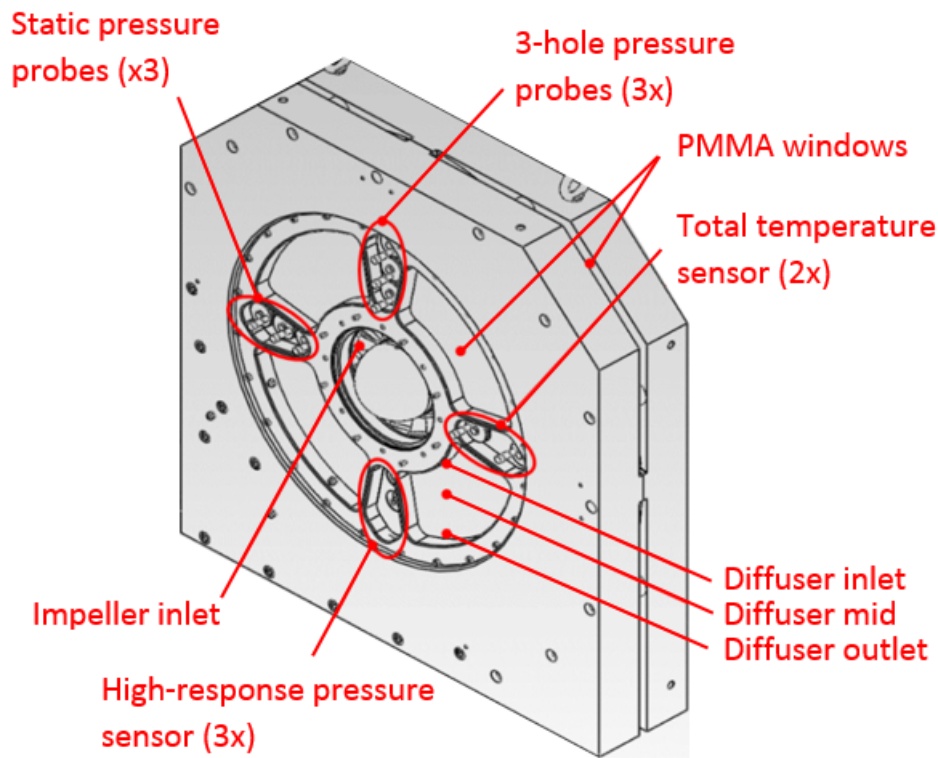


Figure 6: Instrumental specification for compressor block

In [Table 1](#) a comprehensive list of all sensors used in this study is given. The tag numbers refer to the labels of each sensor in the P&ID included in [Appendix A](#) which also indicates the positions of the sensors on the rig.

Table 1: Instrumentation list

TAG NAME	DESCRIPTION	INSTRUMENT	NOMINAL RANGE
ST – 1.1	Shaft speed	Relative rotary encoder	0 – 1200rpm
FT – 1.5	Water flow meter	KHRONE OPTILUX 5000	0 – 4.17L/s
PT – 3.1	Orifice differential pressure	SMAR-LD301	0 – 250mbar
PT – 3.3	Static orifice inlet pressure	Apilsen PCE 28	0 – 3bar
PT – 3.4	Static inlet pressure	Apilsen PCE 28	0 – 3bar
PT – 3.5	Static outlet pressure	Apilsen PCE 28	0 – 3bar
PDT – 1.1	Differential pressure sensor	GE UNIK 5000	0 – 500mbar
PDT – 1.2	Differential pressure sensor	GE UNIK 5000	0 – 500mbar
PDT – 1.3	Differential pressure sensor	GE UNIK 5000	–500 – 500mbar
PDT – 1.4	Differential pressure sensor	GE UNIK 5000	–500 – 500mbar
PE – 1.1	Pressure fluctuations	High res. ICP pressure sensor	690kPa
PE – 1.2	Pressure fluctuations	High res. ICP pressure sensor	690kPa
PE – 1.3	Pressure fluctuations	High res. ICP pressure sensor	690kPa
TT – 5.1	Orifice inlet temperature	Class A PT-100 (RTD)	0 – 130°C
TT – 500.16	Inlet temperature	ASL F500 (RTD)	–200 – 962°C
TT – 500.17	Inlet temperature	ASL F500 (RTD)	–200 – 962°C
TT – 500.18	Inlet temperature	ASL F500 (RTD)	–200 – 962°C
TT – 500.19	Inlet temperature	ASL F500 (RTD)	–200 – 962°C
TT – 500.20	Outlet temperature	ASL F500 (RTD)	–200 – 962°C
TT – 500.21	Outlet temperature	ASL F500 (RTD)	–200 – 962°C
TT – 500.22	Outlet temperature	ASL F500 (RTD)	–200 – 962°C
TT – 500.23	Outlet temperature	ASL F500 (RTD)	–200 – 962°C
TT – 500.24	Water temperature	Class A PT-100 (RTD)	0 – 130°C
XT – 3.1P	Ambient pressure	Barometric pressure sensor	500 – 1100hPa
XT – 3.1T	Ambient Temperature	Platinum RTD sensor	–40 – 60°
XT – 3.1R	Ambient relative humidity	RH sensor	0 – 100%

Part II

THEORY AND LITERATURE REVIEW

CENTRIFUGAL COMPRESSOR FLOW DYNAMICS

The centrifugal compressor was explained in detail in the authors preliminary project thesis [35]. As the scope of this thesis is limited to impeller stage instabilities and documentation of flow regime and component interaction, the details of compressor performance and compressor operation will not be included here. Further restrictions will be set according to test rig specifications in Chapter 2, and for this reason, reviewed theory will primarily be limited to shrouded impellers and vaneless diffusers. A short introduction of the centrifugal compressor is included below.

The centrifugal compressor consists, essentially, of three components:

- The Impeller
- The Diffuser
- The Volute

First, the rotating impeller, imparts a high velocity to the flow. The flow is then decelerated through the diffuser, resulting in a consequent rise in static pressure. Leaving the diffuser, the flow enters the volute, which purpose is to collect and deliver the flow to the outlet pipe. An overview of the components, as well as the velocity and pressure changes through the compressor are shown in Figure 7.

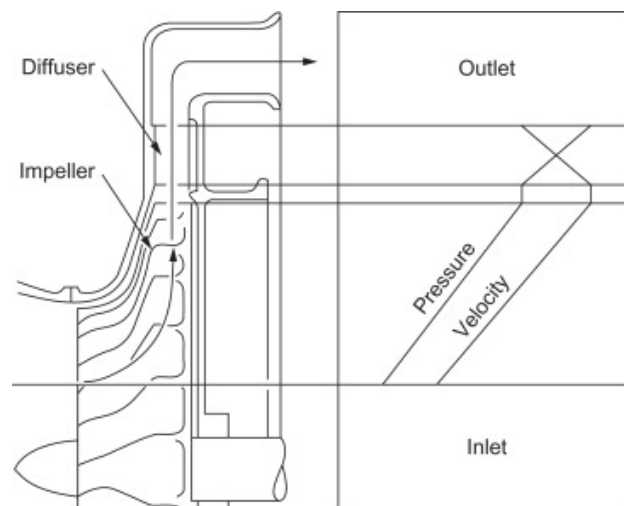


Figure 7: Pressure and velocity through a centrifugal compressor [4]

In order to understand how a fluid moves through each component, a detailed knowledge of all forces acting on the fluid is essential. Direct

solutions of the Navier Stokes equations are needed in order to acquire accurate results for flow behaviour and secondary movement within the components. However, CFD is not included in the scope of this thesis, and focus will be given to prediction of flow regimes and flow phenomena. Given the complexity of certain components, some simplifications will be made. In short, this chapter will give an overview of the different effects compressor components have on the fluid, as well as characteristic flow phenomena through each component. An explanation of occurring effects, and an overview of expected wet gas influence on compressor flow phenomena will also be included.

3.1 BOUNDARY LAYER THEORY

Given the geometry of the centrifugal compressor, with long narrow flow paths through the impeller and deceleration between two flat plates in the downstream diffuser, viscous effects are essential to consider when looking at the different component flow regimes.

Flow through a closed channel can be divided into two distinct regions. What separates them is the changing effect of viscosity, and thus shear forces, on the different fluid layers. In the flow center, viscosity can be neglected, and the flow is viewed as inviscid. This region takes up the majority of the flow channel, and is called the inviscid outer flow. Near the channel walls, the flow can no longer be viewed as inviscid. If the fluid velocity is to reach zero at the wall, fulfilling the no-slip condition, there has to exist a region in which viscosity is no longer neglected. At large Reynolds numbers the transition from the finite velocity in the inviscid outer flow to zero velocity at the wall takes place in a thin layer close to the wall, named by L. Prandtl in 1904 as *the boundary layer* [34].

The formation of a boundary layer is most readily shown on a flat plate as given in [Figure 8](#). At the leading edge there is a constant velocity distribution perpendicular to the plate. The flow is inviscid, and no shear forces are acting on the fluid layers. When the flow hits the plate the effect of viscosity becomes apparent as a retarded flow area is forming between the inviscid outer flow and the zero velocity flow at the plate surface. As the distance from the leading edge is getting larger, the amount of fluid particles caught up by the retardation is increasing. For this reason the thickness of the boundary layer $\delta(x)$, is an increasing function of the distance from the leading edge (x).

The phenomenon discussed so far is known as a laminar boundary layer, and is defined as a region which is affected by viscosity. However, a boundary layer does not always remain laminar. From fluid dynamics it is known that a flow can be either laminar or turbulent. Laminar flow occur where viscous forces are dominant, while a transition into turbulent flow takes place when inertial forces are starting to dominate.

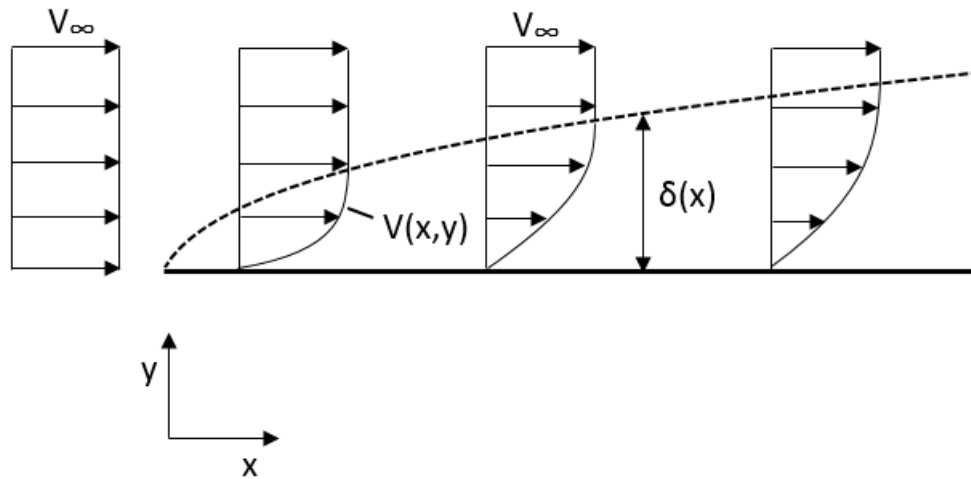


Figure 8: Boundary layer formation on a flat plate

This transition is marked with a critical Reynolds number expressed as the ratio of inertial to viscous forces.

$$Re = \frac{Vx}{\nu} \quad (5)$$

As for flow, after a certain distance from the leading edge, the boundary layer will become turbulent. The turbulent boundary layer is divided into two separate sublayers. Close to the wall, there still exists a thin layer in which viscosity is dominating. This layer is named the *viscous sublayer*, and is the innermost layer in the double layered structure. The majority of the turbulent boundary layer consist of a turbulent layer, characterized by random fluctuating motion, which is unaffected by viscosity. Given the "apparent friction" caused by the fluctuating motion this sublayer is known as the *frictional layer* [34]. The transition is detectable by a sudden increase of the boundary layer thickness, and the transition point is often referred to as x_{crit} , measured from the body leading edge. x_{crit} here denotes the distance from the leading edge to a point at which the critical Reynolds number, Equation 5, occurs. In compressors a transition from laminar to turbulent boundary layers will always take place, and as will be made clear in the following sections, the transition point may contribute to formation of different flow phenomena.

The fact that viscosity influence fluid velocity has now been made apparent. The formation of a boundary layer as depicted in Figure 8 is directly transferable to flow in impeller channels and flow along the walls in a diffuser. The boundary layer will decelerate the flow near the walls, and alter the velocity distribution through the respective components. However, the most important aspect of the boundary layer, regarding flow interaction, is the boundary layer separation.

3.1.1 Boundary layer separation

The phenomenon of boundary layer separation can easily be explained by looking at the flow around a circular cylinder. [Figure 9](#) depicts the streamlines and pressure distribution of the flow around a circular cylinder.

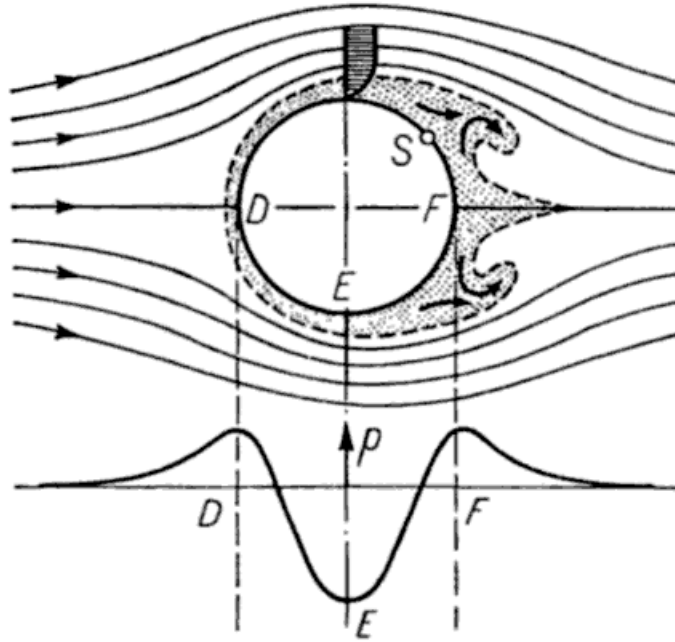


Figure 9: Separation of the boundary layer and vortex formation at a circular cylinder [34]

A particle moving from point D to E in the outer flow will experience an increase in velocity, where energy is transferred from pressure to kinetic energy and, from E to F, a similar decrease in velocity, where kinetic energy is transferred back into pressure. A particle flowing close to the cylinder wall, in the boundary layer, will experience the same velocity and pressure changes. However, where the particle in the inviscid outer layer freely can accelerate and decelerate, the particle in the boundary layer will be slowed by the present viscous forces. This causes the particle to lose much of its kinetic energy, and it is no longer capable of making the transition from point E to F. Because of the increasing pressure, the particle comes to a stand still, and is eventually pushed backwards by the pressure distribution of the outer flow. The point at which this occurs is called the separation point, and is denoted by S in [Figure 9](#).

The previous section pointed out that boundary layers may be either laminar or turbulent. The reason for mentioning this is that the state

of the boundary layer has proved to affect the separation point S [34]. In the turbulent boundary layer, the random fluctuating motion in the frictional layer, and the absence of viscosity, allows the boundary layer to absorb more energy from the inviscid outer flow, delaying separation. Boundary layer stability is therefore an important aspect when analysing flow separation and flow behaviour in compressor components, as component geometry can influence the boundary layer transition, and thus lead to regions of separated flow.

The boundary layer separation phenomenon is transferable to both airfoils and expanding channels, where similar velocity and pressure changes are present, thus making it highly relevant regarding flow behaviour in the impeller and diffuser of a centrifugal compressor. Boundary layer separation is also the main cause of compressor instability, and will be discussed further in [Chapter 4](#).

3.2 IMPELLER CHANNEL FLOW

Being the leading component in a compressor, the impeller's impact on flow behaviour will be apparent through downstream installations. Detailed knowledge of flow behaviour in impeller channels are thus important when further analysing compressor flow regime. Knowledge of separation zones and how multiphase flow will impact the overall flow behaviour are of additional importance, especially when documenting impeller stage instabilities.

The impeller is the working component of a compressor. Its rotating motion imparts energy to the fluid, increasing both the velocity and pressure, see [Figure 7](#). The impeller can be divided into two separate sections, namely the *inducer* and the *centrifugal section*. In a centrifugal compressor the flow enters the inducer in an axial direction and leaves the centrifugal section in a radial direction. Due to the complex geometry of the centrifugal impeller, the task of accurately predicting flow behaviour is ambitious. However, by doing certain simplifications, an approximate prediction can be made.

3.2.1 Force balance

Given the impeller's rotating motion, it is natural to look at the impeller channel in a frame of reference rotating with the impeller itself. By neglecting frictional forces, and looking at a flow element in the inviscid center flow of a blade to blade channel near the impeller outlet, Newton's second law of motion can be written as:

$$m\vec{a}_{\text{rel}} = \vec{F} - m(2\vec{\omega} \times \vec{W} + \vec{\omega} \times (\vec{\omega} \times \vec{r}) + \dot{\vec{\omega}} \times \vec{r}) \quad (6)$$

where \vec{a}_{rel} is the acceleration vector in the relative direction of motion. The remaining components in Equation 6 are, in order, the force from the pressure gradient, Coriolis force, centrifugal force and the rotational rate of change. By adopting a cylindrical coordinate system, and calculating the respective cross products, an estimation of the size and direction of the different force components can be made, see Figure 10b for reference.

$$\vec{\omega} = [0 \ 0 \ -\omega], \vec{W} = [W \ 0 \ 0], \vec{r} = [r \ 0 \ 0]$$

$$\vec{\omega} \times \vec{W} = [0 \ -\omega W \ 0] \quad (7)$$

$$\vec{\omega} \times \vec{r} = [0 \ -\omega r \ 0] \quad (8)$$

$$\vec{\omega} \times (\vec{\omega} \times \vec{r}) = [-\omega^2 r \ 0 \ 0] \quad (9)$$

Inserting this in Equation 6, together with the force from the pressure gradient,

$$\vec{F} = -\frac{1}{\rho} \vec{\nabla} P m = -\frac{1}{\rho} \left(\frac{\partial \vec{P}}{\partial r} + \frac{1}{r} \frac{\partial \vec{P}}{\partial \theta} m \right)$$

expressions for the force balance in the radial direction r and the tangential direction θ can be derived.

$$m \vec{a}_r = -\frac{1}{\rho} \left(\frac{\partial \vec{P}}{\partial r} \right) m + \omega^2 r m \quad (10)$$

$$m \vec{a}_\theta = -\frac{1}{\rho} \left(\frac{1}{r} \frac{\partial \vec{P}}{\partial \theta} \right) m + 2\omega W \sin(\gamma) m \quad (11)$$

The \sin term in Equation 11 is arising because the relative velocity vector \vec{W} is inclined at an angle γ to the axis of rotation. Here the angular velocity is assumed constant such that the rotational rate of change ($\vec{\omega} \times \vec{r}$) is zero. The velocities and different accelerations are displayed in Figure 10b. It should be noted that this equation is derived for a radial blade impeller. If the impeller blades are backswept, which is usually the case due to an increase in operational range, the curved path gives rise to a new acceleration component, $\frac{W^2}{R}$, working perpendicular

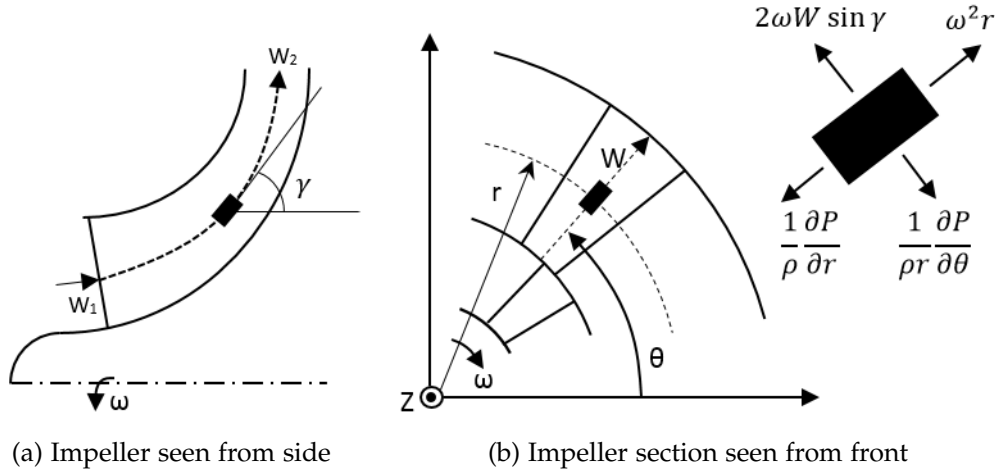


Figure 10: The geometry and accelerations of inviscid flow in a centrifugal impeller

to the relative velocity vector, where R is the blade channel radius of curvature.

By further inspecting Equation 10 and Equation 11, a good estimation of the pressure distribution in the radial and tangential directions of the impeller channel can be made. Rearranging Equation 11, and setting the tangential acceleration to be zero, it is easily shown that the pressure gradient is positive in the θ direction.

$$\frac{\partial \vec{P}}{\partial \theta} = 2\omega W \sin(\gamma)\rho \tag{12}$$

The same can be done for the radial component by imagining a closed outlet valve.

$$\frac{\partial \vec{P}}{\partial r} = \omega^2 r \rho \tag{13}$$

It is thus evident that there is a distinct high pressure and low pressure side in the impeller channel, as well as an increasing pressure in the radial direction.

The last element that needs to be considered in order to get a complete three dimensional understanding of the impeller channel forces is the curvature from impeller inlet to impeller outlet, Figure 10a. From curved channel flow theory [9], it is known that the centrifugal force acting on the fluid element is equal to $\frac{mW^2}{R}$, where R is the impeller radius of curvature. This force will be greater near the hub, and decrease towards the shroud. The only force to balance this centrifugal force is the pressure force, and it is thus clear that the impeller channel also has a positive pressure gradient in the shroud to hub direction.

The previously mentioned pressure inconsistencies gives rise to secondary flow movement in the impeller channel driven by the pressure gradients. This phenomenon is further increased by the reduced energy level of the flow in the impeller channel boundary layers, discussed in [Section 3.1](#), and is known as secondary flow. When discussing the effect of multiphase flow further on in this chapter, these pressure gradients will also be seen to have a significant impact on the impeller channel flow regime.

3.2.2 Secondary flow

In *Compressor Aerodynamics* by N. A. Cumpsty [9], secondary flow is described as the flow at right angles to the primary flow. It is said to be generated when a primary flow with non-uniform stagnation pressure is subjected to accelerations perpendicular to the primary streamline direction. From what was discussed in the previous section, it is already clear that accelerations perpendicular to the primary streamline direction are present in a centrifugal backswept impeller, namely the Coriolis acceleration and the centrifugal acceleration arising from the curved blade to blade channel. It has further been proved that the impeller channel operate with a highly irregular pressure distribution.

The stagnation pressure of a moving fluid is derived as,

$$P_{\text{stag}} = P_{\text{stat}} + \frac{\rho C^2}{2} \quad (14)$$

By looking at [Figure 11a](#), it can be seen that the absolute velocity C can be expressed as a vector sum of the relative velocity W and the rotational velocity U . This gives an expression for the relative stagnation pressure,

$$P_{\text{stag}} = P_{\text{stat}} + \frac{\rho W^2}{2} - \frac{\rho \omega^2 r^2}{2} \quad (15)$$

where $\omega^2 r^2 = U^2$.

From [Equation 15](#) it is clear that the stagnation pressure in the impeller channel depends on the static pressure and the local relative velocity W . The irregular pressure distribution in the channel is thus establishing two regions of low relative stagnation pressure, the region close to the shroud and the region along the suction side of the impeller blade. The flow will also be subject to a change in velocity along the shroud. At the inlet the flow will accelerate, however, in order to maintain a constant mass flow it will be subject to a heavy deceleration towards the impeller outlet. The regions are marked in [Figure 12](#). The deceleration causes a reduction of W at the shroud near the impeller

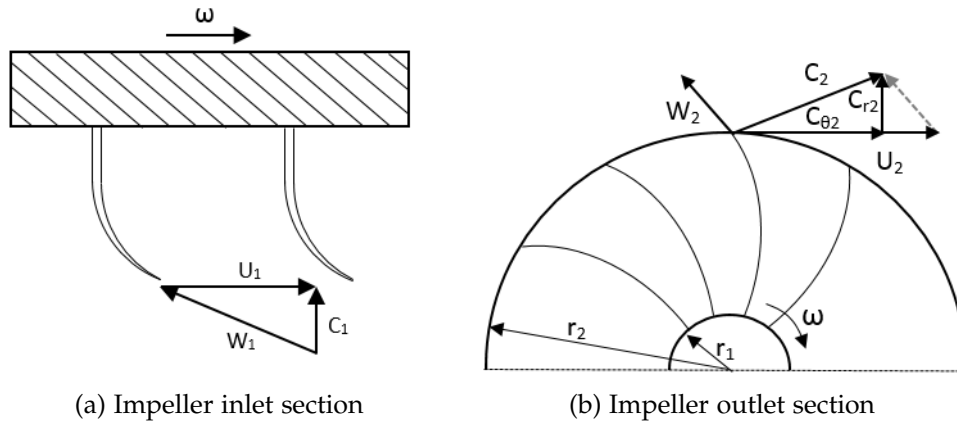


Figure 11: Velocity triangles at impeller inlet and outlet

outlet, which further decreases the relative stagnation pressure in the region. Remembering from Section 3.1.1, that boundary layer separa-

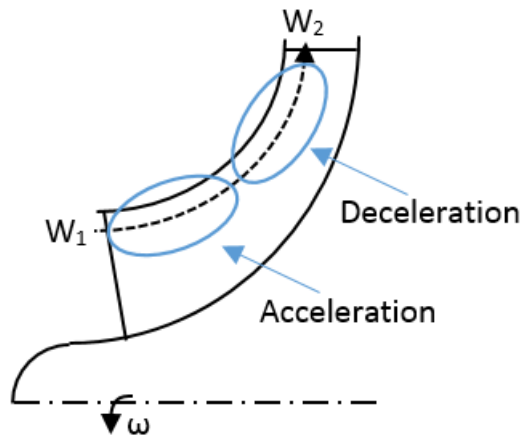


Figure 12: Acceleration and deceleration of the fluid close to the shroud

tion arises from stagnation of the boundary layer flow not longer able overcome the increasing pressure gradient, a reduced stagnation pressure combined with increasing pressure in the radial direction, will increase the risk of boundary layer separation. Another important aspect mentioned in Section 3.1.1 was the delayed separation resulting from turbulent boundary layers. It is known that a boundary layer experiences a destabilizing effect on concave surfaces. Similarly the boundary layer is stabilized on a convex surface, and transition into turbulence is delayed [9]. This means that flow along the hub will experience a faster transition to turbulent boundary layers, while the flow along the shroud will experience a delayed transition. It is thus evident that the shroud region appears as a high risk zone for boundary layer separation, as a laminar boundary layer is less resistant to separation.

When regions of relative stagnant or near stagnant flow has formed, it is expected to see secondary flow movement towards regions of low static pressure [9]. This means that one can expect secondary flows moving from the shroud section towards the region of low relative stagnation pressure at the suction surface of the impeller blade. This effect is further increased by the transverse pressure gradient, arising from the Coriolis acceleration, which will interact with the hub and shroud boundary layers to produce secondary flows in the same direction. The result of these secondary flows is the formation of a low energy region in the shroud/suction area often described as a wake.

The phenomenon of a separated flow region in the impeller channel was first discussed by Dean in 1971 [9]. It was also Dean who named the phenomenon, the jet-wake model, and since its discovery it has been the subject of multiple publications.

In 1973 J. Moore investigated the effects of rotation and secondary flows on flow in a rotating radial-flow passage [27] [28]. Results indicated the formation of a large wake region on the suction side of the passage, at high flow rates. There was also observed a net transport of momentum towards the suction side of the channel in the top and bottom wall boundary layers. This lead to a thickening of the suction side boundary layer as the transported fluid concentrated in the observed wake region. Not long after, D. Eckardt (1976) performed detailed measurements of velocities, directions and fluctuation intensities of the internal flow field of a radial unshrouded discharge impeller, using a laser velocimeter [11]. A summary of the results is given in [9] and shown in Figure 13. Although not directly relevant given the tested impeller was unshrouded, the results provide an excellent illustration of the wake region formation, and is for that reason included. The figure display an even velocity profile at the impeller inlet. As the flow is curved, an irregularity is forming, resulting in a significant flow deceleration on the suction-surface/shroud-corner of the impeller channel. The result is an uneven velocity profile at the impeller outlet, as predicted in the jet-wake model.

3.2.3 Slip

The previous section described the effect pressure distribution had on secondary flows within the impeller channel. The distinct pressure difference at the impeller blade outlet also causes a second effect, namely *the slip velocity*. In an ideal case, the flow would leave the impeller in the same direction as the impeller blades are pointing. However, this is not the case. The distinct pressure and suction side of an impeller blade leads to a shift in the relative velocity leaving the impeller. As soon as the fluid leaves the impeller channel, momentum will be trans-

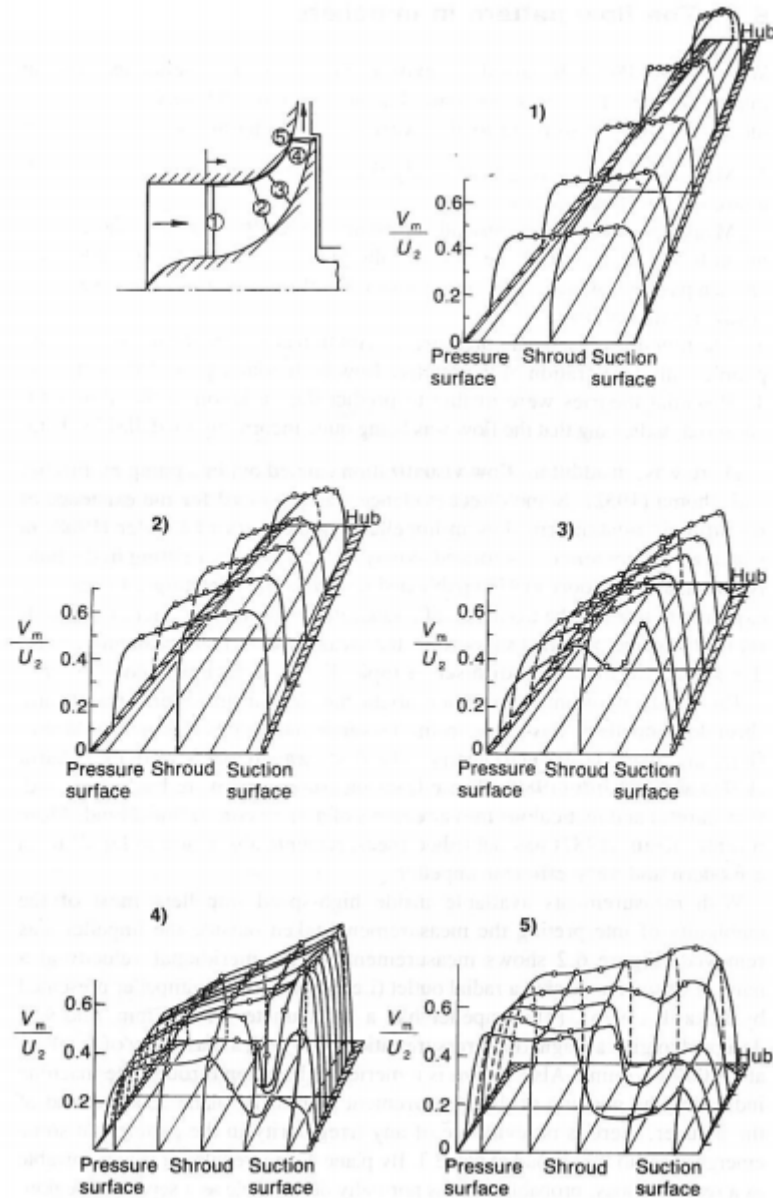


Figure 13: Velocity measurements by Eckardt in a centrifugal unshrouded impeller with no backsweep [9]

ferred from the high pressure side to the low pressure side, equalizing the pressure. The result is formation of a velocity component adverse the direction of rotation and is called the slip velocity. Slip results in a reduction of the tangential velocity entering the diffuser and is thus lowering the potential pressure recovery. The slip velocity and its effect on the impeller outlet velocity diagram is illustrated in [Figure 14](#).

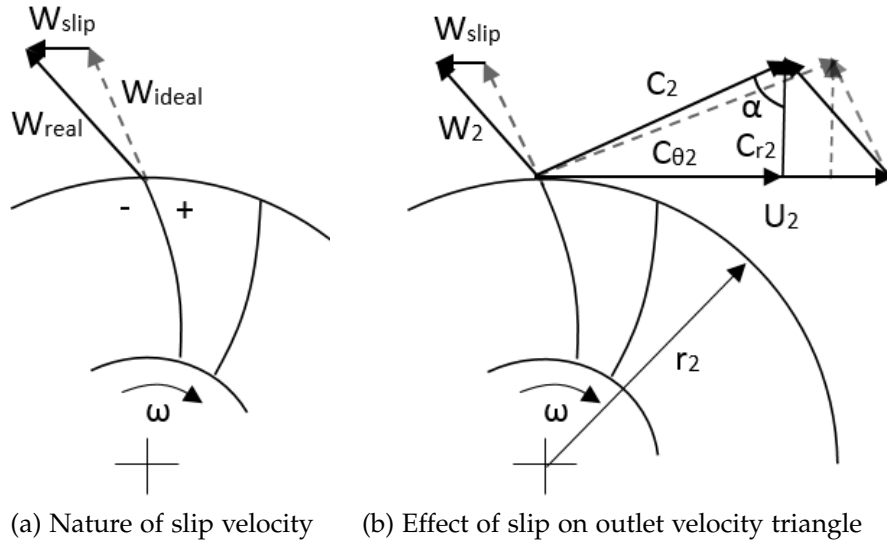


Figure 14: The formation of slip, and effect on outlet velocity triangle

3.2.4 Multiphase effects

Little to no research has been published on the effect multiphase flow has on the impeller channel flow regime. CFD is emerging as a new approach to determine multiphase effects [36], but physical predictions and observations are important in order to verify future results. By looking at the equations derived in [Section 3.2.1](#), certain predictions can be made regarding multiphase effects on flow regime.

Below is a summary of the forces acting on a flow element in the inviscid center flow of a blade to blade channel.

1. Coriolis force: $2\omega W \sin(\gamma)m$
2. Centrifugal force from impeller rotation: $\omega^2 r m$
3. Centrifugal force from blade to blade curvature: $\frac{mW^2}{R}$
4. Centrifugal force from impeller inlet to impeller outlet curvature: $\frac{mW^2}{R}$

All these forces are balanced by the pressure force, and by looking at a finite volume, and expressing mass as a product of volume and density,

it is clear that the above mentioned forces will increase with increasing ρ . Imagining a two phase mixture entering this finite volume, the two phases would be experiencing a different pressure load. If the mixture has a $DR \ll 1$, separation of the phases is a plausible result. In Figure 15 an overview of different forces and their directions are shown.

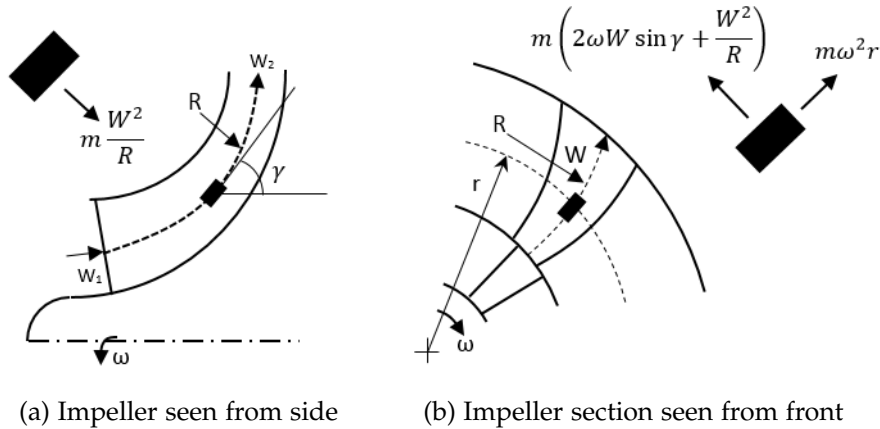


Figure 15: The geometry and force components of inviscid flow in a centrifugal backswept impeller

From this, an expected internal multiphase flow field can be derived. The heavier phase will be forced towards the hub/pressure-side of the impeller channel, while the lighter phase will flow along the shroud/suction-surface, forming a segregated flow regime. Indications of segregated flow was witnessed in the authors previous work [35], and a segregated flow in the impeller channel can lead to significant changes in flow behaviour. The previously discussed wake formation is based on boundary layer effects and secondary flow movement in the impeller channel. A liquid layer along the hub surface will change boundary layer effects, and introduce a new interaction region between the liquid and gas phase. The liquid will also take up a portion of the channel area, reducing available flow area for the gas. Both these effects will increase gas phase velocity, which in turn will delay wake region formation. The concept is sketched in Figure 16.

Slip will also change with the addition of of a second phase. Given a segregated flow, liquid will be concentrated at the pressure side of the impeller blades. The liquid's increased inertia makes it more resistant to the blade tip pressure gradient, and a reduction in slip is expected. However, where slip for gas is assumed constant, the liquid slip is expected to increase in magnitude with increasing pressure, as the higher density makes it more sensitive to pressure changes. Phase drag is another component which arises with multiphase flow, and will depend on respective phase velocities and dispersed liquid droplets. It is evident that knowledge of the internal flow regime is essential in order

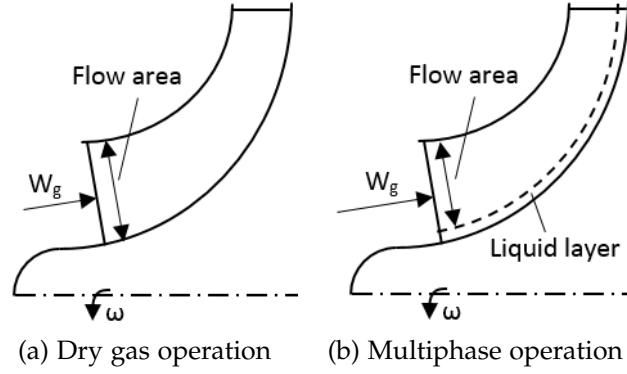


Figure 16: Effect of segregated flow on gas phase velocity

to accurately predict occurring phase interaction, and firmly establish a multiphase flow regime for the impeller.

As pointed out in the chapter introduction, the forces mentioned in this section are not a complete overview of all forces acting on the fluid in an impeller channel. Friction force is a dominant force which has been left out. However, the discussed forces and their directions have provided a sufficient overview in order to describe the different flow phenomena.

3.3 VANELESS DIFFUSER

The stationary vaneless diffuser has a much simpler geometry than the complex rotating impeller. In short, it can be described as an annular channel surrounding the impeller, with parallel or slightly inclined walls. Although simple, the vaneless diffuser is a critical component in a centrifugal compressor, and its purpose is to, as efficiently as possible, convert the high absolute velocity leaving the impeller outlet into pressure. The conversion is made possible by an increasing outlet area in the radial direction. To understand the flow dynamics in a vaneless diffuser, it is helpful to develop a basic analysis for the flow.

3.3.1 Flow analysis

By assuming a constant velocity over the diffuser width and looking at an incompressible inviscid flow, the continuity and Navier-Stokes equations in cylindrical coordinates are as follows:

$$\frac{1}{r} \frac{\partial(\rho r C_r)}{\partial r} + \frac{1}{r} \frac{\partial(\rho C_\theta)}{\partial \theta} = 0 \quad (16)$$

$$\rho \left(\frac{\partial C_r}{\partial t} + C_r \frac{\partial C_r}{\partial r} + \frac{C_\theta}{r} \frac{\partial C_r}{\partial \theta} - \frac{C_\theta^2}{r} \right) = -\frac{\partial P}{\partial r} \quad (17)$$

$$\rho \left(\frac{\partial C_\theta}{\partial t} + C_r \frac{\partial C_\theta}{\partial r} + \frac{C_\theta}{r} \frac{\partial C_\theta}{\partial \theta} + \frac{C_r C_\theta}{r} \right) = -\frac{1}{r} \frac{\partial P}{\partial \theta} \quad (18)$$

Given that the velocity of the inviscid fluid is only dependant on the radial displacement r , the continuity equation and the radial and tangential momentum equations in a radial parallel wall diffuser at steady state are derived as,

$$\frac{1}{r} \frac{\partial(\rho r C_r)}{\partial r} = 0 \quad (19)$$

$$C_r \frac{\partial C_r}{\partial r} - \frac{C_\theta^2}{r} = -\frac{1}{\rho} \frac{\partial P}{\partial r} \quad (20)$$

and

$$C_r \frac{\partial C_\theta}{\partial r} + \frac{C_r C_\theta}{r} = 0 \quad (21)$$

where the tangential pressure gradient is assumed to be zero. Integrating [Equation 19](#) and [Equation 21](#) from diffuser inlet to a point (r, θ) yields,

$$C_r r = C_{r2} r_2 \quad (22)$$

$$C_\theta r = C_{\theta 2} r_2 \quad (23)$$

Combining these two equations and [Equation 20](#), an expression for the pressure increase over the diffuser can be derived [8].

$$\frac{P - P_2}{\frac{1}{2} \rho C_2^2} = \left(1 - \left(\frac{r_2}{r} \right)^2 \right) \quad (24)$$

In [Equation 24](#) the subscript 2 denotes the impeller outlet/diffuser inlet, and it can be seen that the pressure increases with the radius squared.

It is also useful to look at a streamline through the diffuser. The equation for a streamline for an incompressible flow is given by

$$\frac{1}{r} \frac{\partial r}{\partial \theta} = \frac{C_r}{C_\theta} \quad (25)$$

Knowing from Equation 22 and Equation 23 that $\frac{C_r}{C_\theta} = \frac{C_{r2}}{C_{\theta2}}$, Equation 25 can be integrated giving an expression for the flow path through a diffuser

$$\ln \frac{r}{r_2} = \frac{(\theta - \theta_2)}{\tan \alpha} \quad (26)$$

where $\alpha = \tan^{-1}\left(\frac{C_{\theta2}}{C_{r2}}\right)$ is the logarithmic spiral angle measured from the radial direction. Thus, the inviscid flow in a parallel wall radial diffuser follows logarithmic spiral streamlines. The different velocity components and flow angles can be found in Figure 17.

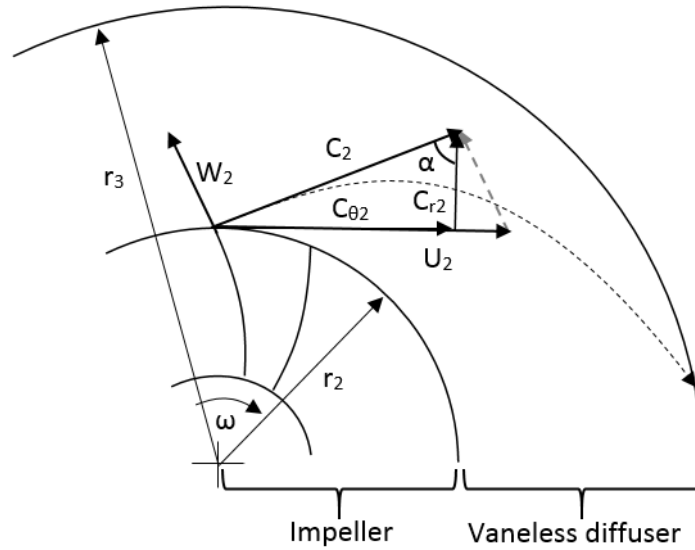


Figure 17: Velocity triangle at the impeller outlet

To view the flow as inviscid and incompressible is of course a major simplification. There are some important effects that has to be considered when investigating the diffuser flow. Viscous stresses in the boundary layers are going to have a big influence, resulting in a deceleration near the diffuser walls and a non uniform velocity profile across the diffuser width. As seen from Section 3.1, these stresses will determine the stability of the flow, where a longer flow path increases the risk of boundary layer separation. Compressibility effects also plays a significant part on the diffuser flow behaviour. The density of a compressible fluid will rise in line with the pressure. The radial velocity must then decrease with radius in order to satisfy the conservation of mass flow. The tangential velocity will not be directly affected by a density increase resulting in an increased inclination angle to the radial direction for the mean flow, or in other words, a longer flow path through the diffuser.

From Figure 17 the dependency of the logarithmic spiral angle on volume flow is clearly visible. An increase in volume flow will result in an

increased radial and a reduced tangential velocity component, reducing the size of α . On the other hand, a reduced volume flow means a reduction of the relative velocity, which in turn leads to an increased α . In this, the stabilizing effect of the backswept impeller blades can also be seen. A radial outlet impeller would get the same increase in logarithmic spiral angle, resulting in a longer flow path. However, where a radial outlet would result in a reduction of the absolute velocity entering the diffuser, a backswept impeller will lead to an increase of the absolute velocity, counteracting the destabilizing effect of the longer flow path.

Figure 17 can also be used to visualize the effect a discontinuous impeller outlet velocity has on the diffuser absolute velocity. The previous section discussed the formation of a wake in the shroud/suction corner of an impeller channel. By imagining the relative velocity leaving the impeller as the mean of the wake velocity W_{w2} and the jet velocity W_{j2} , and knowing that $W_{j2} > W_{w2}$, it can be seen that the wake will be characterized by a larger flow angle α than the jet, thus creating a highly discontinuous velocity field at the diffuser inlet.

3.3.2 Multiphase effects

There are several considerations to be made when determining multiphase effects on the diffuser flow behaviour. The slip factor between the phases SF and the density ratio DR will determine phase drag and influence flow regime. From Section 3.2.1 equations supporting a segregated flow leaving the impeller was established, which in turn will affect the flow behaviour of the diffuser.

From the diffuser flow analysis it is clear that a multiphase flow will affect the flow path through the diffuser. The higher inertia of the liquid phase will counteract deceleration in the diffuser resulting in a shorter flow path for the liquid. By assuming an incompressible liquid, deceleration from compressibility is also removed, further shortening the liquid flow path. Given a segregated flow, the liquid phase may then act as a guide vane for the gas phase, forcing it to take a reduced flow path through the diffuser, lowering pressure recovery. Different flow angles for the phases will also result in substantial mixing losses, as gas particles will collide in passing liquid particles. This effect is expected to be greatest at lower flows, where the logarithmic spiral angle of the gas phase velocity is greatly increased in succession with an increased absolute velocity. Additionally, segregation of the phases leads to a reduced flow area for the gas phase in the impeller, further increasing its velocity. Another consideration is the drag and phase slip between the phases. Some liquid droplets will be dispersed in the gas phase. If the slip factor SF reaches a value below unity, the entrained droplets will exert drag on the gas, hindering deceleration. The two phase mixture

will also lower the compressibility of the gas phase, reducing deceleration due to density changes. It should be noted that this effect varies with GVF, and is negligible as the GVF approaches 100%. Knowing that density is a function of pressure and temperature, a further increase of gas density will follow owing to the higher heating capacity of the liquid phase and the resulting gas phase cooling.

Lars Brenne [5] investigated the effect of two-phase air-water flow on the diffuser pressure recovery. The diffuser performance was found to decrease when liquid droplets were entrained in a continuous gas due to insufficient deceleration of the high inertia liquid-phase. Liquid was also found to accumulate in low energy regions, initiating separation. It is thus expected to see accumulation of water in the low energy regions of the diffuser wall boundary layers.

3.4 VOLUTE

The purpose of the volute is to collect the fluid leaving the diffuser and, as efficiently as possible, deliver it to the outlet pipe. Volute are not always included in compressor design, but they are very common in industrial compressors and generally added in applications where size is not a limiting factor [16] [9]. Compared to impeller and diffuser flow, the volute is by far the most neglected component in centrifugal compressor research [37]. The majority of published results focus on the influence of volute design on compressor performance, and not the velocity distribution inside the volute.

To ease the volute design process, the geometry is set such that velocity in the circumferential direction is kept constant. This is equivalent with a circumferentially constant pressure, and allows the volute to be treated as if it had no upstream effect on the compressor. From the previous section it is already established that the velocity leaving the diffuser is non-uniform over the diffuser width. However, for the purpose of analysis, the mean radial and tangential velocities out of the diffuser will be considered. Given the low velocity in the volute compared to the impeller and diffuser, frictional effects will be neglected. With uniform static pressure and no wall friction it follows from conservation of the moment of momentum that

$$r_3 C_{\theta 3} = r C_{\theta} \quad (27)$$

Thus, regardless of the volute cross sectional area, the circumferential velocity is fixed by the local streamline radius about the axis of the machine [9]. Once the mean radius of the volute is decided, it can easily

be seen that for a given tangential velocity leaving the diffuser, the mean velocity through the volute is fixed.

$$r_3 C_{\theta 3} = r_m C_{\theta m} \quad (28)$$

The radius and velocity components in Equation 28 can be related to Figure 18, where the geometry and velocity components of a volute are shown.

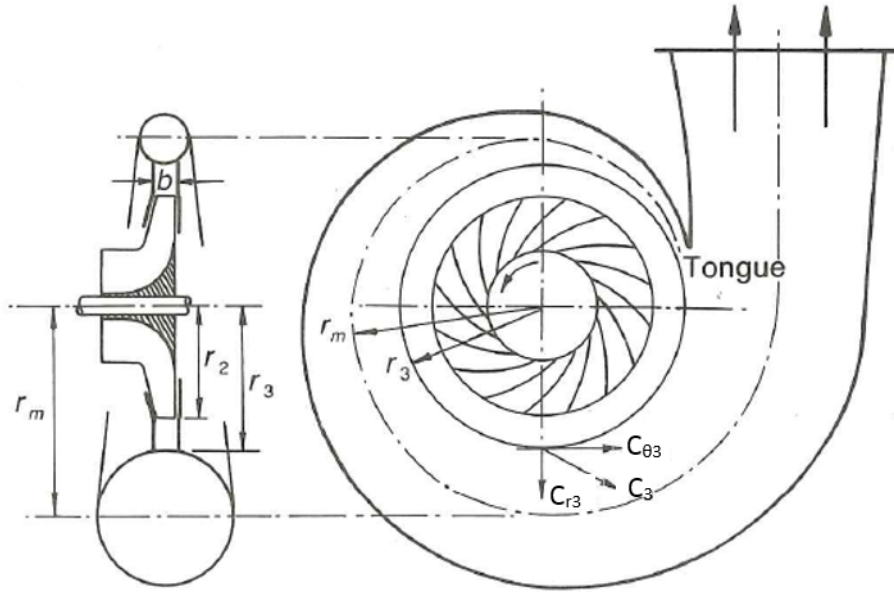


Figure 18: The geometry of a volute surrounding a centrifugal compressor with a vaneless diffuser [9]

From Figure 18 it is also clear that the mass flow leaving the diffuser is dependant on the radial velocity C_{r3} while the mass flow leaving the volute is decided by the tangential velocity $C_{\theta m}$. An expression for the conservation of mass flow can be written as

$$\frac{d}{ds}(\rho_m C_{\theta m} A) ds = \rho_3 C_{r3} b r_3 d\theta \quad (29)$$

where b is the axial width of the diffuser at r_3 , A is the cross-sectional area of the volute and s denotes distance around the volute. By replacing ds with $r_m d\theta$ and introducing Equation 28 to Equation 29, an expression for the cross-sectional area change through the volute can be derived,

$$\frac{d}{ds} \left(\frac{A}{r_m} \right) = \frac{\rho_3 C_{r3} b}{\rho_m C_{\theta 3} r_m} \quad (30)$$

showing that $\frac{A}{r_m}$ is increasing with s for a constant $C_{\theta m}$.

The specified volute characteristics means that the volute is designed for a specific operating point, with a specific tangential velocity and density. Any operation outside this point, will lead to irregularity, and affect volute flow characteristics and compressor operation. If the compressor is operating at increased load, the fluid will enter the volute with an increased radial and a reduced tangential velocity component, as discussed in [Section 3.3.1](#). The increased radial component results in the formation of a large cross-sectional swirl, while the reduced tangential component means that the fluid must accelerate through the volute in order to maintain mass flow conservation. This acceleration leads to a pressure decrease along the volute circumference, affecting the pressure distribution in the entire compressor. Similar effects can be seen at low loads, where reduced radial and increased tangential velocity components is the result. This will necessarily lead to a deceleration through the volute, causing a pressure increase along the flow path. From [Figure 18](#) the volute tongue can be identified as a critical point for instability occurrence, as it will experience a highly discontinuous pressure rise. The design of the tongue is also important regarding the inclination angle this will make to the local velocity profile, where at increased flow, the risk of boundary layer separation will increase due to the increased radial velocity. The occurrence of swirling flow and the discussed pressure and velocity changes in centrifugal compressor volutes are well documented by R. A. Van den Braembussche et al. [37] and E. Ayder et al. [2].

3.4.1 *Multiphase effects*

Knowing that the volute is designed for a specific operating point and a given fluid composition, there is little doubt that the addition of a second phase will cause significant changes in the volute flow behaviour. The previous sections have discussed how multiphase flow affects both the impeller and the diffuser. The volute will experience the combined effect, and will be forced to operate outside of its design point. The most significant effects will be the reduced flow path through the diffuser and the cooling effect of the liquid phase changing the gas phase density. Both these effects lead to an increased radial velocity at the diffuser outlet causing swirl and acceleration through the volute. A counteracting effect of the mixture density change is that a volute designed for dry gas operation will have a cross sectional area too big for the multiphase mixture, leading to deceleration through the volute. Which effect is dominating depends on operating point, upstream effects and volute design.

3.5 COMPONENT INTERACTION

It has now been firmly established that flow at the impeller outlet is highly non-uniform. From the previously displayed [Figure 17](#) it can be seen that a variation in relative velocity will affect the absolute velocity entering the diffuser and its direction. At first sight, it might seem difficult for a downstream diffuser to provide an efficient pressure recovery from the distorted flow entering it. However, research has shown that this unsteadiness has little influence on the pressure recovery as the "jet and wake" quickly merge into a mean velocity through the vaneless diffuser [9]. What the unsteady structure does affect is the angle of the mean radial flow. M. Inoue et al. reported that the change of the wake core position with flow rate significantly affected the mean velocity profile in the axial direction at the inlet to the diffuser [22].

Another important phenomenon arising from component interaction is leakage. Given the impeller specification mentioned in [Chapter 2](#), tip leakage between impeller blades and shroud is not relevant for this thesis. However, leakage due to gaps between the rotating impeller and the stationary diffuser can influence the impeller inlet flow regime. In [Figure 19](#) a sketch of the impeller and diffuser indicates where regions of leakage and hence backflow may occur.

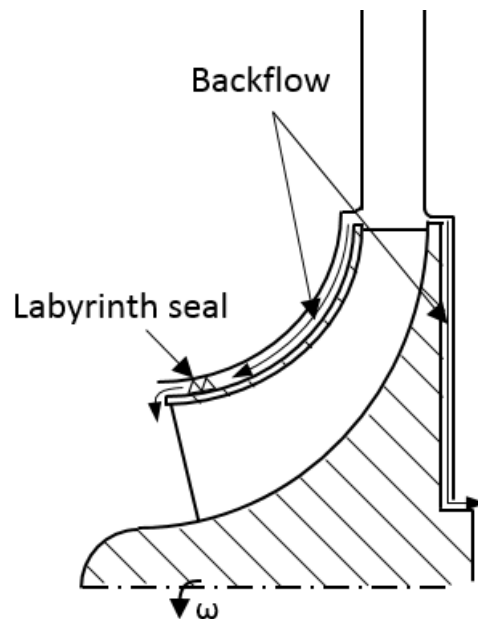


Figure 19: Indication of backflow regions between compressor components

This backflow arises due to the pressure increase from impeller inlet to impeller outlet. In order to reduce the leakage, a labyrinth seal is installed. However, at low flow and high pressure ratio the leakage may be significant. The backflow between the impeller shroud and the dif-

fuser wall is particularly important regarding impeller inlet flow regime at reduced flow.

Volute interaction will become apparent at low and high loads. The previous section discussed how the pressure distribution through the volute will change when a compressor operates outside of design point. At high loads, a local stall section can form at the volute tongue, causing an unstable area at the diffuser outlet affecting diffuser stability. The pressure will also decrease around the volute circumference, causing velocity changes through the diffuser. The volute can also affect the onset of backflow between the compressor components. At low loads, the volute will affect the pressure profile of the entire compressor. The pressure is increasing through the volute, and as a result, there will be a pressure maximum at the volute outlet. This pressure increase will change the pressure distribution in the diffuser down to the impeller outlet. An increase in impeller outlet pressure will affect the onset of backflow, and the region closest to the volute tongue is of specific interest. The disturbance from the tongue can be large right through the impeller, also affecting upstream conditions. Measurements upstream of turbochargers have shown reverse flow out of the inducer at a fixed circumferential position related to the tongue at unstalled operating conditions [9].

3.6 SUMMARY AND TEST RIG CONSIDERATIONS

The impeller installed at the NTNU test rig facility is a shrouded back-swept impeller. A wake is expected to form in the shroud/suction-section of the impeller channel, characterized by a lower relative velocity and a resulting increased logarithmic spiral angle entering the diffuser. As a result of the backsweep, absolute velocity entering the diffuser is expected to increase at lower flows, while at the same time being subject to a longer flow path. Additional components include a vaneless straight walled diffuser and a modified circular volute. The traverse velocity profile in the diffuser is expected to be influenced by boundary layer viscosity, resulting in a deceleration at the diffuser shroud and hub wall. Flow reduction is expected to increase the logarithmic flow path through the diffuser, and boundary layer separation should first appear in the outer regions. Leakage from impeller outlet to impeller inlet is a possibility given a small gap between impeller and diffuser shroud. The volute is expected to produce a circumferential pressure gradient at any operation outside of design point. The volute tongue's location, indicated in [Figure 4, Chapter 2](#), may lead to increased leakage in the lower parts of the impeller inlet at low flows.

Multiphase flow is expected to produce a segregated flow regime in the impeller channels. A reduced slip, and a reduced flow path through

the diffuser are expected results. A mixing region between gas and liquid is expected to form downstream the impeller outlet as the phases will move differently through the diffuser, the gas phase tending to take a longer path. Given that the installed volute is modified for wet operation, a slower buildup of the circumferential pressure gradient is expected at low flows compared to dry gas operation.

In order to document impeller stage instabilities, flow regime at the impeller inlet tip area, as well as interaction between the different compressor components at low flow conditions, a detailed understanding of the different compressor instability phenomena is needed. This chapter will introduce the most common compressor instabilities, and how they can be detected. A section on wet gas impact is also included, which will provide an overview of published results and expected behavioural changes. The chapter will end with a summary of the different phenomena and which can be expected under testing given the test rig specifications provided in [Chapter 2](#). The topic of centrifugal compressor instabilities were also discussed in the authors previous work [\[35\]](#), and due to the importance of this topic, it is also included in this thesis.

4.1 STALL

Stall is one of two aerodynamic instabilities occurring in a centrifugal compressor. In the field of aerodynamics, stall is a well known phenomenon. The angle of attack increases above a certain limit, resulting in flow separation and vortex formation on the low-pressure side of the airfoil. The principle was explained in [Section 3.1.1](#), where boundary layer separation in the flow around a cylinder was described. The same phenomenon will occur at the inlet of a centrifugal compressor if the volumetric flow is sufficiently decreased or the rotational speed sufficiently increased. From the inducer reference point, the relative velocity W_1 is the fluid inlet velocity. The fluid hits the impeller blades at a certain angle of attack, which at design-point, gives the best efficiency through the compressor. Given a reduction of the inlet velocity, the angle of attack on the impeller blade is increased. This leads to a thickening of the boundary layer on the suction side of the impeller blade. If the inlet velocity is further reduced and the critical angle of attack is reached, flow separation will occur. An illustration is given in [Figure 20](#).

As described in [\[33\]](#) and [\[16\]](#) the stall phenomenon occurring in compressors is often referred to as *rotating-stall*. The reason being the formation of one or more stall-cells propagating around the compressor annulus. This can be explained by [Figure 21](#) where stall in channel B averts the incoming flow, resulting in an increased angle of attack for

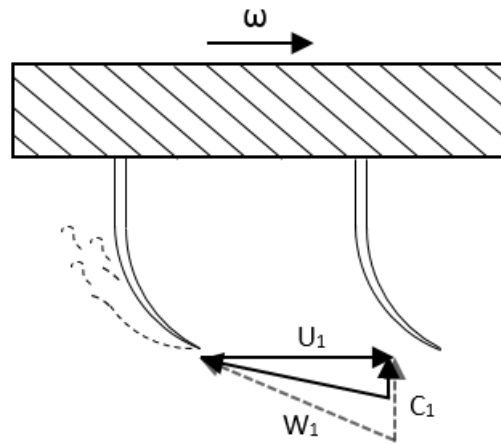


Figure 20: Illustration of stall onset

channel A and a reduced angle of attack for channel C. This leads channel A to stall, allowing channel B to recover, and a rotating stall effect is the result. Correspondingly, the stall-cell evolution will be adverse to the rotation of the impeller leading to a stall-cell propagating at a fraction of the impeller speed. The stall-cell can be detected by the pressure and velocity fluctuation it is creating and is documented in literature.

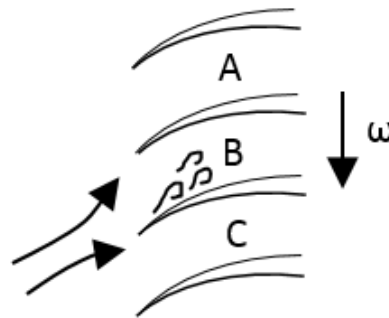


Figure 21: Illustration of rotating impeller-stall propagation

Rotating stall does not only occur in the impeller. As explained in [Section 3.3.1](#), a reduced volume flow will also result in an increased flow path through the diffuser, it is thus natural that stall may also appear here. The geometry of the vaneless diffuser and the adverse pressure gradient in the radial direction makes it inherently unstable. By increasing the flow path, the distance of viscous interaction will increase and eventually the flow will be forced to a halt. This point marks the onset of diffuser stall, and a region of stalled flow will form in the outer parts of the diffuser channel. This "blockage" will influence the diffuser flow path, and the effect can be seen in [Figure 22](#). Flow

upstream of the blockage will be inclined towards the radial direction, stimulating stall recovery, while the flow downstream of the blockage will be inclined tangentially leading to additional stall buildup. The result is again a rotating stall region, propagating in the direction of rotation. The phenomenon was recently documented by S. Ohuchida et al. [30].

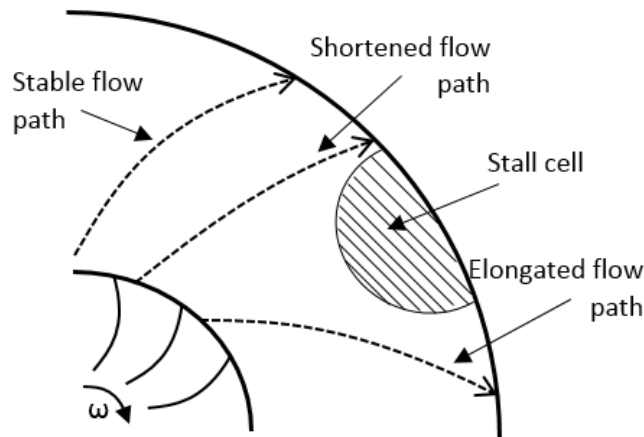


Figure 22: Illustration of rotating diffuser-stall propagation

Frigne et al. [15] was able to document a distinction between different types of impeller and diffuser rotating stall in a centrifugal compressor with a vaneless diffuser. They concluded that almost all rotating instabilities could be subdivided into three distinct groups:

1. Diffuser rotating stall due to a strong interaction between boundary layer and inviscid core flow in the vaneless diffuser. This is characterized by a low relative propagation speed ($\leq 20\%$ of impeller rotating speed).
2. Abrupt impeller rotating stall due to a strong interaction between impeller and diffuser. Characterized by a relative propagation speed between 20 and 40%.
3. Progressive impeller rotating stall due to flow separation in the impeller. Characterized by a very high relative propagation speed (50-80%).

A further differentiation between abrupt and progressive impeller stall was made by N. A. Cumpsty in [9]. Impeller stall is here defined as either part-span or full-span stall. Part-span stall is described as one or multiple rotating stall cells partly extending over the annulus, while in full-span stall, the stall cells fully cover the impeller annulus. Part-span cells are observed to rotate at close to 50% of the impeller speed, and

leads to a progressive stall phenomenon, as described by Frigne et al. [15]. Full-span cells usually rotate more slowly in the range of 20-40% [9] and the resulting stall phenomenon is the previously mentioned abrupt impeller stall. Part-span stall is often detected as a precursor to full-span stall.

Stall may also appear as a stationary cell in the inducer. In Section 3.4 the effect of reduced volume flow on volute behaviour was discussed. Any operation outside of design point will result in a circumferential static pressure gradient in the volute. At low volume flow, the volute cross sectional area is too big, and the flow will be subject to a deceleration. This leads to a static pressure buildup through the volute, with a maximum appearing at the volute tongue. This pressure buildup will create a region of increased static pressure at the circumferential location nearest the volute tongue stretching all the way to the inducer. An increase in static pressure is equivalent to a decrease in velocity, and a stationary low velocity region can thus form at the inducer entrance. Given a low volumetric flow, this can result in a stationary stall region at the inducer inlet. The phenomenon was documented by D. A. Fink et al. [14] whom investigated turbocharger surge in a radial impeller-vaneless diffuser free-spool system. Stationary stall cells are known to propagate, and may act as an initiator to rotating stall.

Rotating or stationary stall are mechanisms which allows the compressor to operate at very low volumetric flows. The reduced flow is distributed between non-stalling cells, making continued operation possible. Although the local mass flow varies around the impeller annulus, the overall mass flow is assumed constant. This is not the case for surge.

4.2 SURGE

Surge is the second aerodynamic instability phenomenon occurring in centrifugal compressors and is characterized by low frequency, high amplitude pressure and flow fluctuations. It is a highly unwanted phenomenon, as surge oscillations may cause structural damage and induce vibration in other parts of the compression system. Knowledge of the centrifugal compressor characteristic is important in order to understand the surge cycle. Figure 23 illustrates the effect downstream choking inflicts on a centrifugal compressor operating at constant speed.

Imagining a closed choke valve (D), no mass flow would go through the compressor, and the pressure rise is equal to the centrifugal pressure head produced by the impeller [33]. Opening the valve will initiate flow movement and the diffuser will contribute to the pressure increase. At point C the compressor is near its maximum efficiency and the pressure ratio reaches its peak value. Further opening of the valve will lead to a reduced flow path in the diffuser, see Section 3.3.1, and the pressure

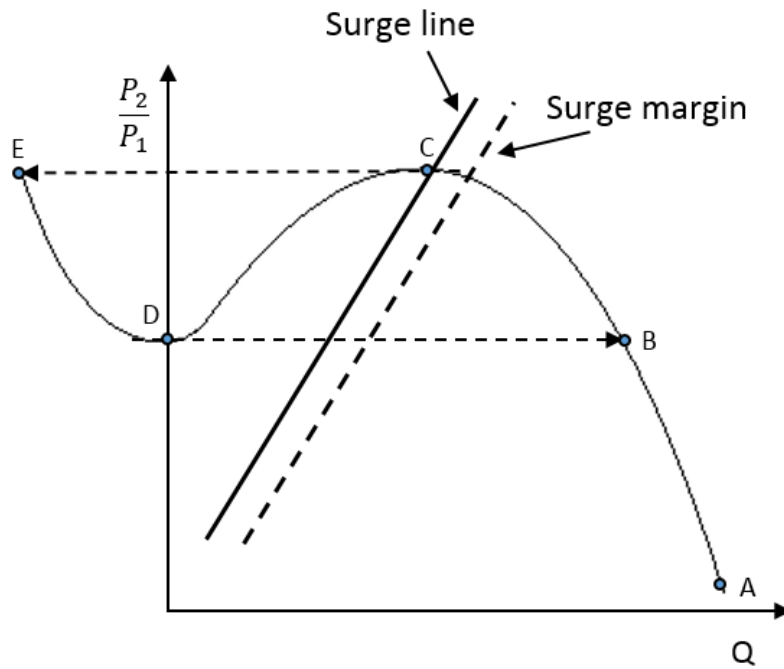


Figure 23: Centrifugal compressor characteristic, with illustrated deep surge cycle

ratio will drop as a result of the reduced diffusion effect. In practice, operation between point D and C is not possible. At low inlet velocities aerodynamic instabilities arise in both impeller and diffuser, discussed in [Section 4.1](#), and further reduction may lead to surge. The surge cycle, indicated in [Figure 23](#), can be described as follows:

1. The cycle starts in C where the flow is becoming unstable. Additional decrease of volume flow will result in delivery pressure reduction.
2. The downstream pressure is now higher than the compressor delivery pressure, resulting in a negative pressure gradient and backflow. The operating point has jumped to E.
3. Backflow occurs till the pressure is equalized, and the compressor follows the characteristic to point D.
4. Stable operation is now possible, and the compressor jumps to point B, completing the cycle.

It is common to distinguish between different levels of surge. *Mild/classic surge* refers to the condition where the overall mass flow oscillates, but remains in the forward position. *Deep surge*, the cycle explained in [Figure 23](#), is when the mass flow fluctuation increase to the

extent of backflow being observed. There is also a phenomenon known as *modified surge*, which is a combination of surge and rotating stall [16].

Whether or not stall is a precursor to surge is debated in literature. There is no doubt that rotating stall can lead to surge, but whether it is necessary or not is unclear. D. A. Fink et al. [14] investigated surge dynamics in a radial impeller vaneless diffuser free-spool system. Measurements indicated impeller stall at the inducer tips to be a key phenomenon in initiating surge. The effect of downstream volume size on surge fluctuations was also investigated. Downstream volume size refers to the plenum size downstream the compressor outlet but upstream the outlet choking valve. Results displayed a strong relation between downstream plenum size, fluctuation amplitude and fluctuation frequency. A large downstream volume result in big amplitudes and low frequent fluctuations. The frequency is set by the plenum emptying and filling times. Small volumes make the detection of surge difficult, as the mass flow will constantly adjust itself, and it was observed that operating points previously initiating surge only displayed rotating stall when downstream volume was reduced.

To avoid surge onset, surge control systems are standard in the industry. A surge margin, as indicated in Figure 23, is decided, and all operation left of this point is avoided by flow regulating systems.

4.3 SHOCK FORMATION

The compressor operating range is limited by two factors. At low flow, onset of the two discussed aerodynamic instabilities will mark the lower operating limit. There is also a limit at high mass flows, namely *the choking point*. The choking point characterizes the point when flow reaches supersonic velocity somewhere along the compressor stage. In a centrifugal compressor the maximum relative velocity will occur in the impeller inlet section at the inducer blade-tip. Given the Mach number relation

$$\text{Ma} = \frac{V}{\sqrt{\kappa_v ZRT}}$$

and knowing that $T_2 > T_1$ it is evident that the critical area for Mach number control is at the inducer inlet blade-tip. If the flow reaches $\text{Ma} = 1$ shock formation can occur resulting in flow separation and severe losses [33].

Although choking is a limiting factor on compressor operation the phenomenon is mostly encountered in axial compressors. Centrifugal compressors rarely operate close to the choke line, and the only reason for mentioning it here is the effect multiphase flow has on the fluid's Mach number.

4.4 MULTIPHASE EFFECTS

Grüner and Bakken [17] concluded that introduction of a liquid phase to the flow contributed to a delayed instability onset. The same result was found in the author's pre-project [35], and a proposed explanation was phase segregation taking place in the impeller leading to a reduced flow area for the gas phase at the impeller inlet. The phenomenon was discussed and illustrated in Section 3.2.4. A reduction in flow area leads to increased velocity and a later onset of instability. Dispersed liquid droplets will induce drag on stagnating flow on the suction side of inducer blades. This will delay separation, and may be another explanation for the delayed instability onset. In Section 3.3.2 the effect of multiphase flow on diffuser flow behaviour was discussed. The flow was believed to take a shorter path through the diffuser when a liquid phase was added. This will lead to a later onset of diffuser instability. In Section 3.4.1 the multiphase effect on volute behaviour was discussed. The reduced flow path through the diffuser forces a shift to the right of the volute design point, leading to flow acceleration, however, the increased density leads to a reduced volume flow, which causes a flow deceleration. The combined effect decides the pressure buildup at the volute tongue which is known to affect instability onset.

Grüner and Bakken [17] discovered an extending annulus ring of liquid forming at the impeller inlet prior to full surge when operating in wet conditions. The same phenomenon was documented and investigated in the authors previous work [35] and by Ferrara et al. [13]. The phenomenon can be caused by backflow from the impeller, but can also be a result of leakage through the labyrinth seal.

The speed of sound is known to decline as liquid content rises [20]. This results in an increased Mach number, and choked flow may be an increased problem for centrifugal compressors when operating under wet conditions. No indication of shock formation was found in the authors pre-project, however, it is an important consideration to keep in mind.

4.5 SUMMARY AND TEST RIG CONSIDERATIONS

In a centrifugal compressor the impeller stage instabilities are expected to appear as either stall or surge. Stall at the inducer can develop as rotating cells propagating at a fraction of the impeller rotational speed or as a stationary cell caused by the pressure buildup at the volute tongue. Stall can also develop in the diffuser, given the elongated flow paths at low volumetric flows. Impeller stall is expected to be a precursor to surge which is detectable by significant mass flow and pressure fluctuations. The downstream volume in between impeller outlet and the

outlet choking valve is expected to have a major impact on the surge fluctuation frequency and amplitude. The downstream volume on the NTNU test rig facility is small. A difficulty in detecting surge is therefore expected.

The volute installed at the NTNU test rig facility is intentionally designed with a reduced cross sectional area in order to account for the increased density of the multiphase flow. For this reason, the pressure buildup at the volute tongue is expected to appear at lower volumetric flow for wet operation than for dry, which can contribute to a later onset of instability.

FLOW VISUALIZATION TECHNIQUES

This chapter will describe different approaches to visualize flow behaviour and instability phenomena. [Chapter 3](#) gave an overview of the flow behaviour through each compressor component and [Chapter 4](#) described the different instabilities and their characteristics. The visualization techniques used should be suitable to detect changes caused by different flow phenomena and instability for both dry and wet conditions. Focus will be given to techniques made possible by equipment already installed at the test rig facility. A short description of other relevant flow visualization techniques will also be included aiding further development of the NTNU wet gas test facility.

5.1 PRESSURE SENSORS

Pressure sensors are a necessity when visualizing compressor flow. The compressor operating point is determined by pressure readings, and the onset of aerodynamic instabilities are characterized by pressure and flow fluctuations. There is a variety of different pressure sensors and probes enabling visualization of specific flow phenomena.

5.1.1 *Static pressure sensors*

Static pressure sensors measure the static pressure of the flow. A great advantage with static pressure readings is that sensors or probes can be flush mounted in the respective components allowing for accurate static pressure measurements without interfering with flow behaviour.

5.1.2 *Differential pressure sensors*

Differential pressure sensors measure the pressure difference between two respective pressure levels. Information on component pressure rise and flow velocity can easily be determined with differential pressure readings.

5.1.3 Multi-hole probes

Multi-hole probes are widely used in combination with differential pressure sensors to determine flow angle and stagnation pressure. Stagnation pressure is the sum of static and dynamic pressure, given as

$$P_{\text{stag}} = P_{\text{stat}} + \frac{1}{2}\rho V^2$$

where V is the fluid velocity. The concept of multi-hole probes can easily be understood from [Figure 24](#), where a 3-hole probe mounted perpendicular to the flow direction is shown.

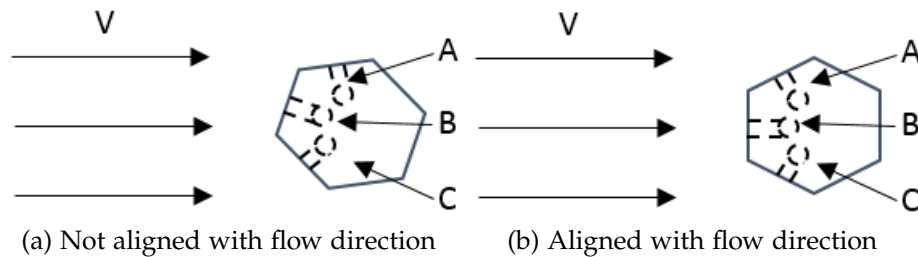


Figure 24: Three hole probe perpendicular to flow direction

Hole A and C are connected with tubing to a differential pressure sensor, showing the difference in stagnation pressure between the two. As seen from [Figure 24a](#), the stagnation pressure in hole C will be greater than that in hole A because of the difference in perpendicular velocity components. When the differential pressure between the two holes are zero, the probe will be aligned perfectly with the flow direction, and a true value for the stagnation pressure can be measured from hole B.

There are some difficulties arising when utilizing pressure probes in wet conditions. Given that the sensor is not in direct contact with the flow, but connected to a probe through tubing, liquid is known to leak through the probes forming liquid bubbles in the connecting tubes. This causes inaccurate pressure readings, and pressure probes are thus not suited for wet gas operation.

5.1.4 High-response pressure sensors

In [Chapter 4](#) the pressure fluctuating characteristic of rotating stall and surge was described. These pressure fluctuations are expected to occur at a frequency in the range of 1 – 100% of the rotational frequency. In order to detect these fluctuations, high-response pressure sensors are needed. High-response pressure sensors have been, and are still used with great effect in experimental stall and surge investigation. A

common technique is to use a Fast Fourier Transform (FFT) on high-frequency pressure fluctuating readings. This is a mathematical evaluation function which transforms time-related oscillation data into the frequency range. Transformation from the time domain into the frequency domain is a common tool in analysing instability characteristics, and well documented in literature [17] [19] [3].

5.1.5 Test rig installations

In order to get a good overview of the pressure characteristics and flow dynamics in a compressor, a combination of the above mentioned sensors and probes are needed. Table 2 lists the different pressure sensors and probes installed at the NTNU test rig facility. For detailed location, the reader is referred to Figure 6 from Chapter 2 and the P&ID in Appendix A.

Table 2: Installed pressure probes and sensors

DEVICE TYPE	TAG NAME	LOCATION
Static pressure sensor	PT – 3.4	Compressor inlet
Static pressure sensor	PT – 3.5	Compressor outlet
Static pressure probe	-	Impeller outlet
Static pressure probe	-	Diffuser mid
Static pressure probe	-	Diffuser outlet
3-hole probe	-	Impeller outlet
3-hole probe	-	Diffuser mid
3-hole probe	-	Diffuser outlet
High-responsive pressure sensor	PE – 1.1	Impeller outlet
High-responsive pressure sensor	PE – 1.2	Diffuser mid
High-responsive pressure sensor	PE – 1.3	Diffuser outlet
Differential pressure sensor	PDT – 1.1	-
Differential pressure sensor	PDT – 1.2	-
Differential pressure sensor	PDT – 1.3	-
Differential pressure sensor	PDT – 1.4	-

5.2 DIRECT VISUALIZATION

Direct visualization is important in order to gather useful information about flow behaviour. Qualitative information on flow regime, phase

interaction and distribution is obtainable by observing the flow through transparent installations.

5.2.1 *Foreign material injection*

An interesting possibility in direct visualization is the injection of foreign materials to the flow. At discrete points in the flow, dye, smoke or any traceable material is released into the fluid in order to visualize its behaviour. The foreign material is then swept along with the mean flow, and any trends, disturbances or other interesting phenomena can be documented. The technique is well suited for both dry and wet conditions, as the injected material's properties are chosen for specific operating conditions. Different injection methods are also used in order to determine flow velocity and direction. The author can recommend [26] for a detailed overview of different techniques and their area of application.

5.2.2 *Thread attachment*

The flow regime at the impeller inlet and in the diffuser are characterised by rapid fluctuations and irregularity when operating in the unstable region. For this reason, injected substances are subject to turbulence and may disperse quickly. A method to visualize the flow characteristic near instability onset, especially in dry conditions, is the use of threads. Threads can be attached to areas of interest to see how the flow behaves. Fluctuations in the flow velocity will be clearly visible, as threads will flicker when subject to an irregular flow.

5.2.3 *Stroboscope*

A stroboscope is a useful tool when visualizing phenomena in rotating machines. In simple terms, the stroboscope is a lamp which produces brief repetitive flashes of light. If the stroboscope frequency is adjusted to the rotational frequency, or a submultiple of it, the rotating object will appear stationary. This allows for visualization of flow phenomena which would otherwise be invisible due to the rapid rotation.

5.2.4 *Test rig installations*

The NTNU test rig facility was presented in [Chapter 2](#), and it was made clear that transparent thermoplastic installations can be found at the impeller inlet section and in the diffuser shroud wall. Direct visualization techniques are therefore of high relevance when documenting flow be-

haviour in the compressor. The discovery of an extending annulus ring of liquid forming at the impeller inlet prior to full surge by Grüner and Bakken [17] is a great example of the importance of direct visualization.

5.3 COATING

A large variety of coatings are available in the turbomachine industry. There are coatings to reduce surface roughness, protect against corrosion and to reduce erosion. Coatings are also being developed to help visualizing flow behaviour and changes over surfaces. A good example is the relatively new approach to surface pressure measurements, the use of pressure-sensitive paint (PSP). Conventional methods are based on pressure probes and sensors, limiting information to only discrete points on a surface. By using PSP the pressure can be measured over the entire surface of a body, without the risk of equipment interfering with the flow [25]. Coatings can also be used to effectively give information on phase segregation in a two phase mixture, as the resistance to different substances may vary.

5.4 OTHER TECHNIQUES

There are several other techniques used for flow visualization well documented in literature. The techniques discussed so far are all applicable to the NTNU test rig facility, as the necessary equipment is already in place. The techniques discussed in this section will not be subject for implementation, but are relevant for further development of the test facility.

5.4.1 *Optical techniques*

There are several optical techniques used for dry gas visualization. Particle Imaging Velocimetry (PIV) and Laser Doppler Velocimetry (LDV) are two of the most used techniques for velocity measurements in turbomachines [24].

5.4.1.1 *Particle Imaging Velocimetry*

PIV is a measurement technique based on seeding a transparent fluid with tracer particles. Sufficiently small particles will not influence the natural tendency of the flow, and follow the streamlines accurately. At the desired position, a high energy light source illuminates the particles, and two pictures are taken in quick succession. Knowledge of the time interval between the photographs makes it possible to calculate the velocity of the flow. An alternative way is to use high frequent light

pulsations and only take one picture. Again, time between the pulses must be known. For high-speed flows, such as the flow out of an impeller, this requires the use of a high-speed camera in combination with a laser. The technique is well documented in literature and Wernet et al. [38] proved this to be a powerful technique for capturing instantaneous flow field phenomena. The results given by D. Eckardt [11] cited in Chapter 3 was performed using a similar technique called "*Laser-2-Focus Velocimetry*" (L2F).

5.4.1.2 *Laser Doppler Velocimetry*

LDV is based on the principle of Doppler shift. The fluid is exposed to a high energy light source with a known frequency. Particles in the fluid will reflect this light, and the reflected light-frequency is measured. The shift seen in frequency is caused by the fluid motion, and known as the Doppler effect. The fluid velocity is determined from this registered shift in frequency.

5.4.1.3 *Challenges*

The use of optical visualization techniques encounter some problems regarding wet flow applications. The flow regime described in Chapter 1 can make visualization of seed particles difficult. Marie Jellum [24] discussed the application of optical visualization techniques and pointed out another problem being the water droplets dispersing effect on the laser light. There is also a limiting factor in the impeller design of the test rig facility rendering optical techniques impractical. The impeller is shrouded, thus removing the necessary access to the flow.

5.4.2 *Vibroacoustic measurements*

Another detection method explored, is the use of vibroacoustic measurements. Aretakis et al. [1] investigated the possibility of detecting unstable operating conditions of a turbocharger using vibroacoustic measurements. It was emphasized that the disadvantage of the usual instability detection systems were the rather increased sensitivity to non laboratory environments. Since ordinary detection systems need to be placed in contact with the flow path, they might not be suited for use in field operating machines. Sound and casing vibration measurements are much less intrusive than the traditional systems. It was found that the RMS value of the acoustic signals, filtered in the sub-synchronous part of the spectrum gave the possibility to distinguish between stall-free, stalled and operation with surge present.

Part III

TEST DESIGN AND EXPERIMENTAL
RESULTS

EXPERIMENTAL SETUP AND PROCEDURE

Based on reviewed visualization techniques in [Chapter 5](#) and the limitations of the compressor rig, [Chapter 2](#), a set of six different tests were designed in order to document impeller stage instabilities, flow regime, secondary flow phenomena and compressor component interactions.

1. *3-hole probe measurements*: in order to determine flow angle and velocity at the impeller outlet and in the diffuser at different locations on the compressor characteristic.
2. *Thread attachment*: in order to visualize impeller inlet and diffuser flow characteristics in dry conditions at low flow.
3. *High-response pressure readings*: in order to detect pressure fluctuation frequencies and analyse the transition from stable to unstable operation.
4. *Impeller coating*: in order to investigate phase separation in the impeller channel.
5. *Labyrinth injection*: in order to document the effect of labyrinth backflow on impeller inlet flow regime.
6. *Stroboscope and visual observation*: in order to detect impeller inlet and diffuser flow characteristics in wet conditions.

6.1 3-HOLE PROBE MEASUREMENTS

3-hole probes were chosen to analyse the impeller outlet and diffuser outlet flow regime in dry conditions. The impeller flow characteristic was thoroughly reviewed in [Section 3.2](#), and formation of a wake region in the shroud/suction side corner of the impeller channel was pointed out as an expected phenomenon. Flow angle and velocity readings were expected to provide a good indication on wake region formation as the wake will be characterized by an increased tangential flow. For explanation see [Section 3.3.1](#).

The 3-hole probes were used in combination with static pressure probes and differential pressure sensors to provide accurate information on velocity and flow direction. Measurements were done at the diffuser inlet and diffuser outlet, see [Figure 6](#) in [Chapter 2](#). In [Figure 25](#) a model of the installed 3-hole probes is shown. Hole A and C were

connected to a differential pressure sensor with a range of ± 500 mbar, allowing for accurate probe alignment to the flow direction. The measured angle was the logarithmic spiral angle α , in other words, the angle between hole B and the radial direction in the diffuser. The velocity was determined by connecting hole B and the corresponding static pressure probe to a second differential pressure sensor. The concept was discussed in [Chapter 5](#), and the stagnation pressure from hole B subtracted the static pressure at the location provided measurements for the dynamic pressure $\frac{1}{2}\rho C^2$.

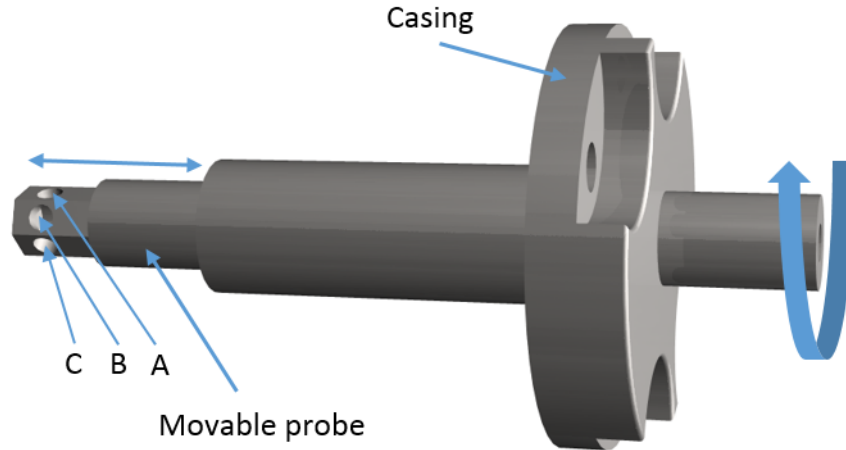


Figure 25: Model of 3-hole probe

Measurements were done at five points over the diffuser width. The traverse measurement locations are given in [Table 3](#), where 0% of diffuser width represents the diffuser shroud, and 100% the diffuser hub.

Table 3: Locations for flow angle and velocity measurements

LOCATION	% of diffuser width				
	Point 1	Point 2	Point 3	Point 4	Point 5
Diffuser inlet	0	25	50	75	97
Diffuser outlet	0	25	50	75	97

The reason for 97% being the maximum diffuser width was a distance of 0.5 mm between the probe tip and its holes, preventing measurements being done at the hub wall surface. Measurements were taken at different locations on the compressor characteristic, and the test matrix can be found in [Table 4](#).

Table 4: 3-hole probe test matrix

RPM	Flow coefficient (ϕ)						
6000	0.065	0.05	0.04	0.03	0.028	0.026	0.024
9000	0.065	0.05	0.04	0.03	0.028	0.026	0.024

6.1.1 Accuracy

The differential pressure sensors' accuracy was thoroughly investigated before test initiation. Calibration was performed and an error margin was estimated. The error measurement calculation procedure as well as calibration procedure can be found in [Appendix C](#), and a copy of the results are given in [Table 5](#).

Table 5: Differential pressure accuracy test results

SENSOR	ε_S	3σ	MAX ε_{tot}	MIN ε_{tot}
PDT.1-1	-0.02 [mbar]	0.02 [mbar]	-0.04 [mbar]	0.00 [mbar]
PDT.1-2	-0.10 [mbar]	0.02 [mbar]	-0.12 [mbar]	-0.08 [mbar]
PDT.1-3	-0.22 [mbar]	0.05 [mbar]	-0.27 [mbar]	-0.17 [mbar]
PDT.1-4	-0.39 [mbar]	0.07 [mbar]	-0.46 [mbar]	-0.32 [mbar]

The accuracy of flow angle measurements was also subject for investigation. A range for acceptable differential pressure deviation had to be decided, as a differential pressure of zero was next to impossible to accomplish given manual adjustment of the 3-hole probes. In [Figure 26](#) a sketch of the absolute velocity in the diffuser entering a 3-hole probe is given. C_A and C_C represents the velocity components of the absolute velocity entering hole A and B. The 3-hole probes used in this experiment had a hexagon shaped head, and the angle between each hole was 60 degrees.

The static pressure over the sensor head was assumed constant, allowing an expression for the dynamic pressure difference between hole A and C to be made.

$$\frac{1}{2}\rho C_A^2 - \frac{1}{2}\rho C_C^2 = \frac{1}{2}\rho(C \cos(\beta))^2 - \frac{1}{2}\rho(C \cos(\beta - 120))^2 \quad (31)$$

By rearranging [Equation 31](#), an expression for the flow angle β based on the dynamic pressure measurements from hole A, B and C was derived.

$$\frac{1}{2}\rho C_A^2 - \frac{1}{2}\rho C_C^2 = \frac{1}{2}\rho C^2 \sin(120) \sin(120 - 2\beta) \quad (32)$$

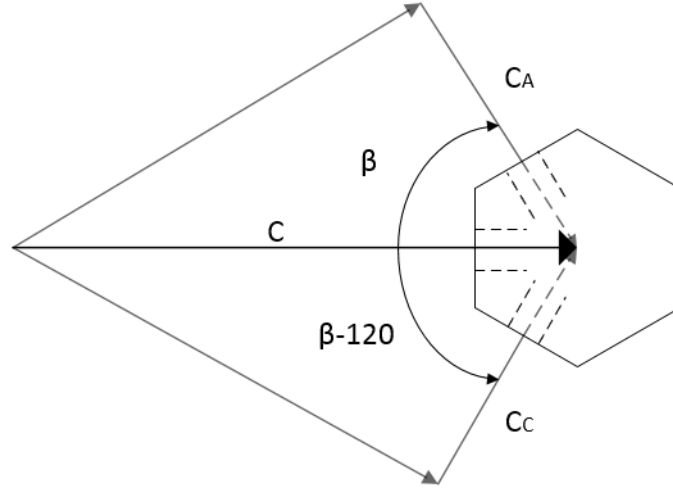


Figure 26: Absolute velocity components

$$\frac{\frac{1}{2}\rho C_A^2 - \frac{1}{2}\rho C_C^2}{\frac{1}{2}\rho C^2} \frac{1}{\sin(120)} = \sin(120 - 2\beta) \quad (33)$$

$$\beta = \frac{120 - \sin^{-1}\left(\frac{\frac{1}{2}\rho C_A^2 - \frac{1}{2}\rho C_C^2}{\frac{1}{2}\rho C^2} \frac{1}{\sin(120)}\right)}{2} \quad (34)$$

Given values for the flow dynamic pressure and the differential pressure between the two guide holes, the error in flow angle measurement could now be estimated as $\beta - 60$.

From preliminary tests, a range of ± 1.5 mbar was chosen as acceptable for the angle adjustment. More accurate adjustment proved difficult and was very time consuming. Adjusted for the maximum sensor error in Table 5, a value of ± 2 mbar was chosen for calculation of the maximum flow angle measurement error. In Table 6 the results from the error estimation are shown. The estimates were based on dynamic pressure readings in the flow center at 9000 rpm and the given operating points.

Table 6: Calculation of flow angle measurement error

POSITION	$\phi = 0.065$	$\phi = 0.05$	$\phi = 0.04$	$\phi = 0.03$
Impeller outlet	$\pm 0.78^\circ$	$\pm 0.69^\circ$	$\pm 0.62^\circ$	$\pm 0.54^\circ$
Diffuser outlet	$\pm 1.79^\circ$	$\pm 1.95^\circ$	$\pm 2.02^\circ$	$\pm 2.50^\circ$

A sample size of 60 was decided as sufficient for mean velocity determination. With a logging frequency of 2 Hz this is equivalent to 30 seconds of logging at each operating point and depth. A stabilisation period of 10 minutes was allowed between each operating point. As pressure and velocity stabilizes quickly, a longer stabilization period was deemed unnecessary.

6.2 THREAD ATTACHMENT

Previous research had proved the formation of an extending annulus ring of liquid forming at the impeller inlet prior to full surge. In order to further investigate this phenomenon, a detailed documentation of impeller inlet instability onset has been carried out for dry conditions. Threads were fitted circumferentially around the impeller inlet allowing for detection and determination of instability phenomena. Previous research had proved difficulty in detecting surge onset, given the small downstream volume on the NTNU test rig. Neither was any attempt made to distinguish rotating and stationary inducer stall. The threads were installed as a solution to both these problems, ensuring a clear way of instability differentiation. The fitted threads were 3 cm long and were glued to the inlet pipe 3.5 cm upstream the inducer, thus leaving an area of 5 mm between threads and inducer inlet. The threads were braided nylon, which prevented deformation in wet conditions. A picture of the fitted threads is given in [Figure 27](#).

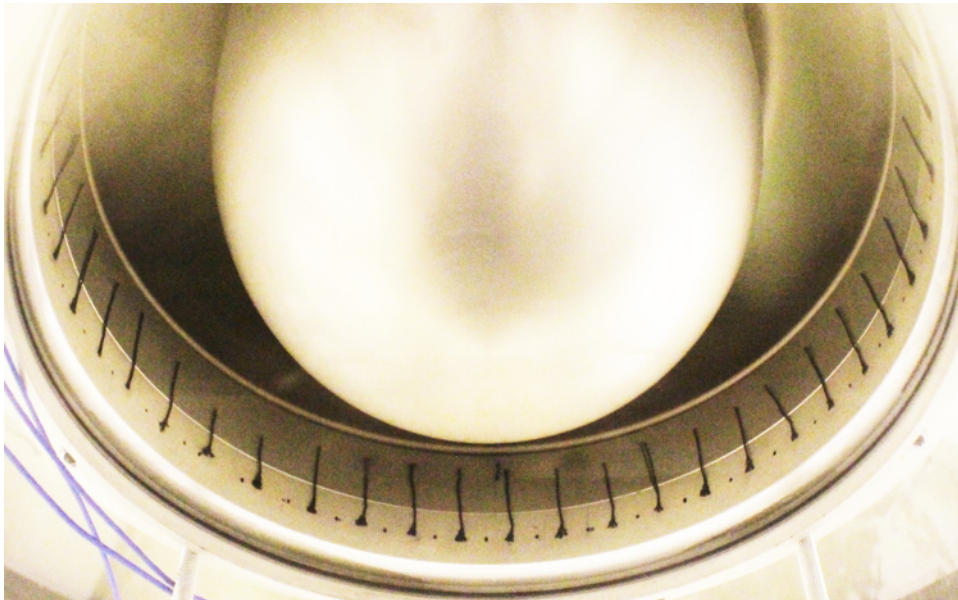


Figure 27: Threads fitted at impeller inlet

Threads were also fitted in the diffuser, in the interest of indicating regions of unstable flow. They were glued to the diffuser hub at diffuser

inlet, mid and outlet in four locations around the diffuser. In [Figure 28](#) a picture of the thread placement is given. Threads were also fitted in the top right, bottom right and bottom left sections.



Figure 28: Thread placement in diffuser top left section

Flow visualization was performed at 6000 and 9000 rpm. Reference pictures were taken at stable operation, then the compressor was slowly operated into instability, while pictures were taken for documentation.

6.3 HIGH-RESPONSE PRESSURE READINGS

High-response pressure sensors are installed at the NTNU test lab facility and served as the primary source of instability detection in this thesis. The sensors are installed at diffuser inlet, mid and outlet, allowing for a complete impeller stage investigation.

In [Chapter 4](#) the nature of the different instabilities were discussed. Given the characteristic frequencies of different instability phenomena, an analysis of the pressure fluctuation frequencies was decided as the most effective instability detection procedure. Transformation of time related oscillating data into the frequency domain was performed in NI DIAdem with a Fast Fourier Transform. The resulting frequency range of a FFT is always half the sampling rate, and the sampling frequency has to be at least 2.5 times the highest frequency to be analysed [23]. As a result, the sampling frequency was set to 20000 Hz, allowing for accurate analysis of the frequency spectra between 0-4 kHz. In order to get a good visualization of occurring pressure fluctuations and the

magnitude of these, the power spectrum was chosen for amplitude representation. This means that plotted values will be the squared of the root mean square of the signal, indicating the power contained in each frequency. The chosen window function was the Hanning window, ensuring a correct representation of the constituent pressure fluctuation frequencies.

A characteristic frequency easily detected in centrifugal compressors is the blade passing frequency arising from pressure fluctuations caused by the passing blades. Another is the fluctuation caused by the impeller revolution and its harmonic frequencies. In performed experiments, instability onset was marked as the appearance of pressure fluctuations surpassing the BPF in amplitude. A performed FFT is displayed in [Figure 29](#). This was performed on data acquired at 9000 rpm, equivalent of 150 rps. With a 17 bladed impeller, the BPF is equal to 2550 Hz, and is clearly visible as the dominating amplitude. Harmonics of the impeller revolution are also clearly visible at $2f$ and $3f$, where f is the impeller revolution frequency, 150 Hz.

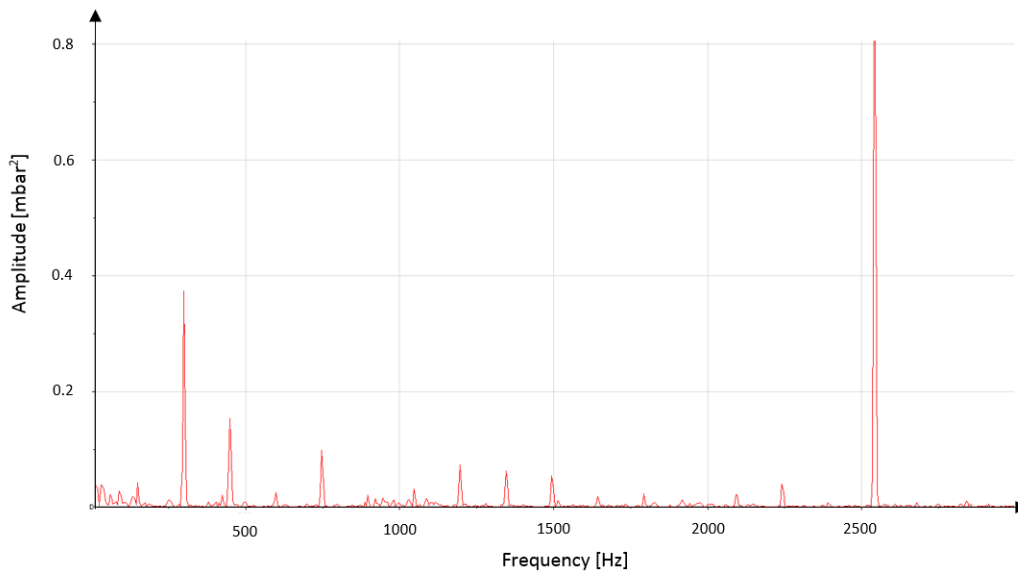


Figure 29: FFT of high response pressure signal acquired at 9000 rpm $\phi = 0.06$ at impeller outlet

Areas of focus were the impeller outlet and diffuser outlet as instability was expected to occur in the impeller or the outer parts of the diffuser. Tests involved running the compressor at stable operation, then incrementally shifting operation into the unstable range of the compressor characteristic. Operational adjustments were done by gradually closing the outlet valve. Given the large sampling frequency, and resulting sizable logging file, it was decided to separate logging into four ranges of ϕ . The test matrix is given in [Table 7](#).

Table 7: Test matrix

RPM	Flow coefficient range [ϕ]			
6000	0.06-0.05	0.05-0.04	0.04-0.03	0.03-0.02
9000	0.06-0.05	0.05-0.04	0.04-0.03	0.03-0.02

In the author's previous work, the effect of multiphase flow on instability initiation was investigated. An increase in surge margin was observed for reduced GMFs. In order to perform a thorough investigation of wet gas instability onset and the effects leading to delayed instability, tests in this thesis were concentrated on 90% GMF, as a further reduction was assumed to enhance already witnessed phenomena. The test matrix for wet operation was the same as given above, however an adjustment of the GMF was performed in between each logging range, ensuring minimal deviation as ϕ was reduced. Calibration of the high-response pressure sensors was performed by PCB Piezotronics, and the calibration certificates can be found in [Appendix D](#).

6.4 IMPELLER COATING

Previous results indicated a separated flow in the impeller channels of the centrifugal impeller when operating under wet conditions [35]. Assumptions were based on distinct water jets being observed at the impeller outlet. To further investigate the flow regime in the impeller channel it was decided to coat the impeller with a water soluble substance, expecting to see a distinct differentiation between regions of coated and uncoated area in the impeller channel. A segregated flow is believed to be one of the main contributors to delayed instability onset, and proof of the phenomenon will go a long way to confirm its relevance.

Preliminary tests were executed in order to validate the concept. A water soluble green paint was chosen as coating, and four impeller channels were coated. The impeller was run for 10 minutes at 6000 rpm with a GMF of 90% at $\phi = 0.065$. 6000 rpm was chosen because previous experiments indicating phase segregation performed by the author [35], was concluded at this speed. In addition, based on derived equations from [Section 3.2](#), an increase of the rotational speed was believed to enhance phase segregation.

For the main test, the whole impeller was coated, enabling multiple channels to be inspected and compared. The compressor was run at dry conditions and inspected in order to rule out any changes arising from dry gas operation. It was then run for 5 minutes at 6000 rpm with a GMF of 90% and $\phi = 0.065$. The diffuser was removed to allow for

thorough investigation of the impeller channels and pictures were taken before and after completion to document any changes in the coating. A picture of the coated impeller is given in [Figure 30](#).



Figure 30: Impeller after application of coating

Given the time consuming work of removing and replacing the diffuser, tests were only completed at $\phi = 0.065$, 90% GMF.

6.5 LABYRINTH INJECTION

In the author's previous work, the formation of an extending annulus ring of water was documented at the impeller inlet during wet instability [35]. The ring appears to form as a result of impeller stall, and backflow of air through the impeller vanes. Further investigation of the appearing annulus ring was initiated in order to get a better understanding of this unstable phenomenon. In [Section 3.5](#) the possible leakage arising from pressure rise over the impeller was mentioned. Leakage from the labyrinth seal into the compressor inlet section will influence impeller inlet flow regime, and the phenomenon is known to increase as the compressor is approaching surge. For this reason, leakage from

the labyrinth seal is believed to be a possible contributor to witnessed phenomenon. The effect of labyrinth leakage on the documented ring formation was not investigated in the authors previous work, and was therefore of interest in this thesis.

In order to document the effect of labyrinth leakage on the impeller inlet flow regime in wet conditions, a hole was drilled in the diffuser shroud upstream the labyrinth seal. The hole allowed for injection of traceable material, which made documentation of leakage possible. The hole's location in relation to the labyrinth seal is sketched in [Figure 31](#), and a picture of the compressor inlet section after modification is given in [Figure 32](#)

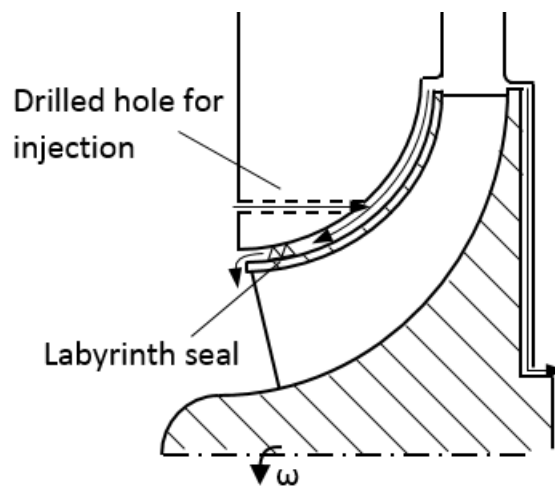


Figure 31: Drilled hole in relation to labyrinth seal

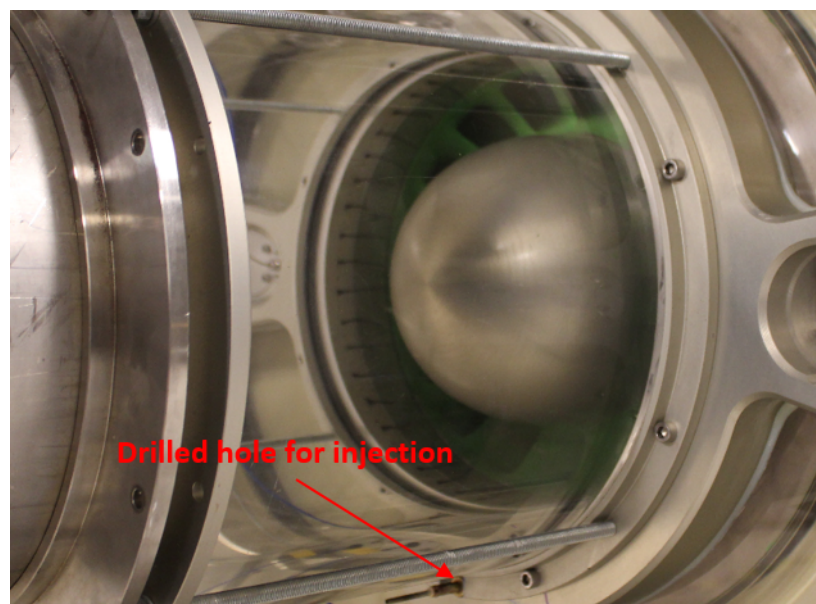


Figure 32: Location of drilled hole

Fluorescent liquid, which is easily detectable by the use of UV light, was used for injection. The fluorescent liquid was filled in a container mounted at the same height as the impeller. The tank was pressurised by a connected compressor outlet static pressure probe. The compressor outlet pressure was used in order to maintain a stable pressure during injection. The tank was connected to a valve, which was further connected to the installed injection probe visible in Figure 32. The diameter of the injection probe is 2 mm, and given the low pressure rise over the compressor, any increase in compressor outlet pressure resulting from flow reduction was assumed to have negligible effect on the fluorescent flow. A sketch of the installed tank is given in Figure 33.

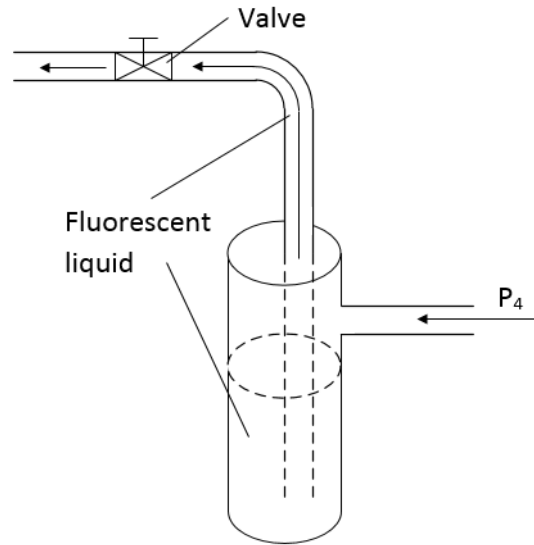


Figure 33: Fluorescent liquid container

Concern was given to the possibility of injected flow enforcing back-flow through the labyrinth seal or up into the impeller outlet. However, performed estimates indicated fluorescent injection to have little effect on the flow regime between impeller and diffuser shroud. In Figure 34 the width of the impeller-diffuser gap on the shroud side is indicated along with the diameter of the injection channel.

From Equation 35 and Equation 36 it is clear that $A_{\text{gap}} \gg A_{\text{inj}}$. The dominant force acting on the backflow region is thus arising from the impeller outlet pressure, and is equal to $P_2 A_{\text{gap}}$.

$$A_{\text{inj}} = \frac{\pi D^2}{4} \quad (35)$$

$$A_{\text{gap}} = 2\pi r_2 b \quad (36)$$

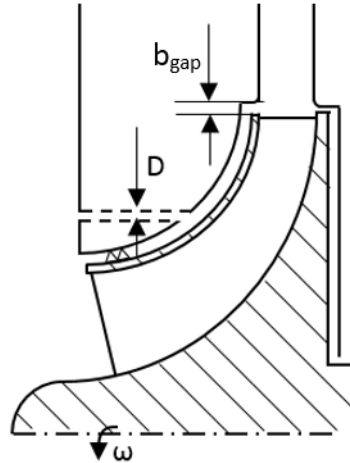


Figure 34: illustration of impeller-diffuser gap width

The effect of labyrinth leakage on impeller inlet flow regime was documented by taking pictures of the inlet flow regime at set operating points with and without fluorescent injection. A UV light was used in order to capture the injected fluorescent liquid. The test matrix is given in [Table 8](#).

Table 8: Injection test matrix

RPM	GMF	Flow coefficient [ϕ]							
6000	90%	0.05	0.04	0.035	0.03	0.028	0.026	0.024	0.022
9000	90%	0.05	0.04	0.035	0.03	0.028	0.026	0.024	0.022

A GMF of 90% was chosen in order to compare results to previously performed experiments. A limitation in visibility through the thermo-plastic inlet pipe section was also a factor, as any GMF below 90% caused a liquid film to form at the pipe wall, rendering direct visualization and documentation impossible.

6.6 STROBOSCOPE AND VISUAL OBSERVATION

In [Section 3.3.2](#), the effect of multiphase flow on diffuser flow regime was discussed. The higher inertia of the liquid phase counteract deceleration, resulting in a shorter flow path for the liquid. Possible phase segregation in the impeller combined with increased inertia can lead to liquid jets, forcing the gas phase to take a shorter flow path through the diffuser. At lower flows, gas phase flow angle is expected to increase, resulting in increased mixing between the phases. An expected liquid accumulation in the low energy parts of the diffuser shroud and hub was also mentioned, based on published research by Lars Brenne [\[5\]](#).

Installed thermoplastic sections in the diffuser made visual observation of impeller outlet and diffuser multiphase flow phenomena possible. A combination of stroboscope and different light settings were used in order to capture occurring effects. The use of a stroboscope allowed for stationary observation of flow leaving the impeller and documentation of multiphase interaction. The stroboscope frequency was set equal to the blade passing frequency, enabling observation of every passing blade channel. In order to accurately capture appearing flow regime in the diffuser, a short shutter time was used in combination with a strong light-source. A shutter time of $1/4000$ s was chosen, reducing blur to a minimum. Flow regime and occurring multiphase effects were documented from stable operation down to the onset of instability. Of specific interest was documentation of phase interaction at lower flows, and occurring regions of unstable flow.

EXPERIMENTAL RESULTS

This chapter will present results gathered from previously described tests. Results from dry operation will be presented first, then wet gas effects will be discussed in detail and compared to witnessed dry phenomena. The majority of presented results will be limited to 9000 rpm, and will be referenced to an operating point based on the flow coefficient ϕ . Wet gas operation was as previously mentioned limited to 90% GMF in order to perform a thorough analysis of occurring effects, another limitation being visibility through the compressor thermoplastic inlet section. In order to provide a graphical representation of discussed operating ranges, the author's previously calculated compressor characteristic is included in [Figure 35](#). The characteristic is taken from the author's previous work [35], where a detailed explanation for calculation procedure can be found. Presented results include operation to the left of this characteristic, and the compressor is then operating in the unstable range.

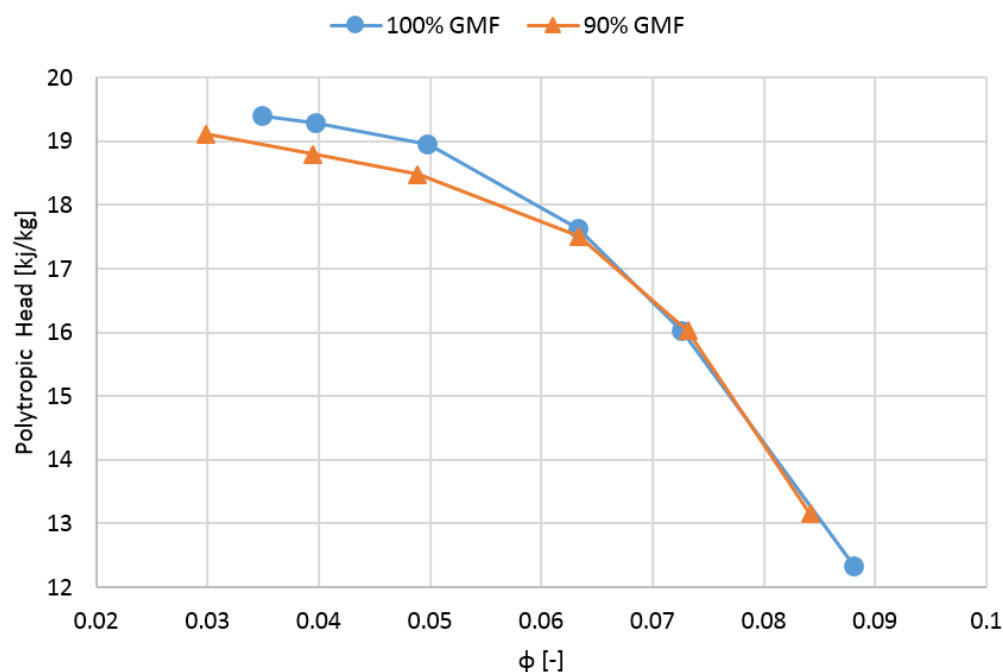


Figure 35: Compressor characteristic at 9000 rpm [35]

7.1 DRY OPERATION

In the following section all results regarding dry operation will be presented. Results include determination of impeller and diffuser flow regime based on 3-hole probe measurements and visualization of flow phenomena connected to compressor instability. Performed instability investigation based on power spectral analysis of high-response pressure readings at impeller and diffuser outlet will be presented first, establishing the operational range, and the different occurring instability phenomena.

7.1.1 Power spectral analysis

High-response pressure readings were taken at the impeller and diffuser outlet areas. Results are presented as a power spectral analysis, which procedure was explained in [Section 6.3](#). Given that instability phenomena are expected to occur at a fraction of the rotational frequency, the area of interest is limited to frequencies in the range 0-150% of the impeller revolutionary speed. Given the low frequency response of the sensors, 0.5 Hz, and the occurrence of some low frequency disturbance, the lower value has been set to 2 Hz in plotted results. In [Table 9](#) an overview of the analysed frequency spectra is given. The higher range is included in order to compare fluctuations with the occurring BPF. Presented results will be limited to 9000 rpm as similar results were witnessed at lower speeds. The low range frequency resolution is 1 Hz.

Table 9: Analysed frequency range

RPM	f	BPF	LOW RANGE	HIGH RANGE
6000	100 Hz	1700 Hz	2-200 Hz	2-2000 Hz
9000	150 Hz	2550 Hz	2-250 HZ	2-3000 Hz

Resulting pressure fluctuation frequencies are plotted as a function of time, which corresponds to the logging time of specified flow coefficient range. For regions of instability onset, the corresponding ϕ vs. time plot will be included. Presented ϕ ranges were all logged at the same time, meaning power spectral analysis of impeller and diffuser outlet correlates to the same time axis.

7.1.1.1 Impeller outlet

In Figure 36 the power spectral analysis of impeller outlet readings is shown for a flow coefficient ranging from 0.06 to 0.05. The high range analysis reveals the BPF as the dominating pressure fluctuation, and no instability is detected.

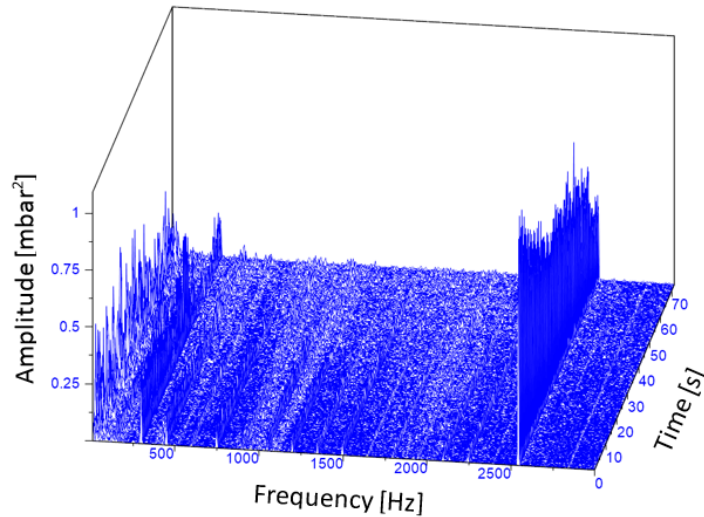
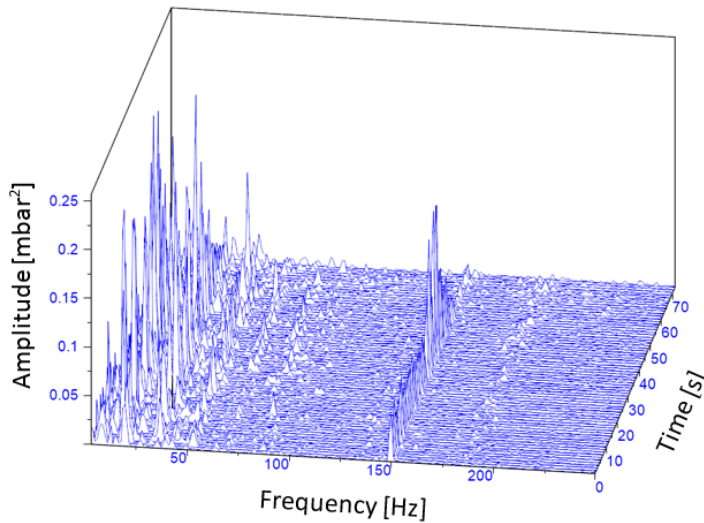
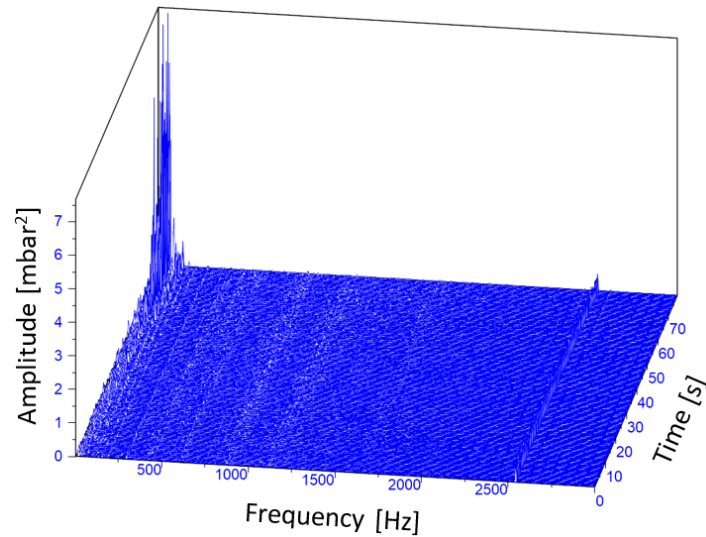
(a) $0.06 \geq \phi \geq 0.05$, 2-3000 Hz(b) $0.06 \geq \phi \geq 0.05$, 2-250 Hz

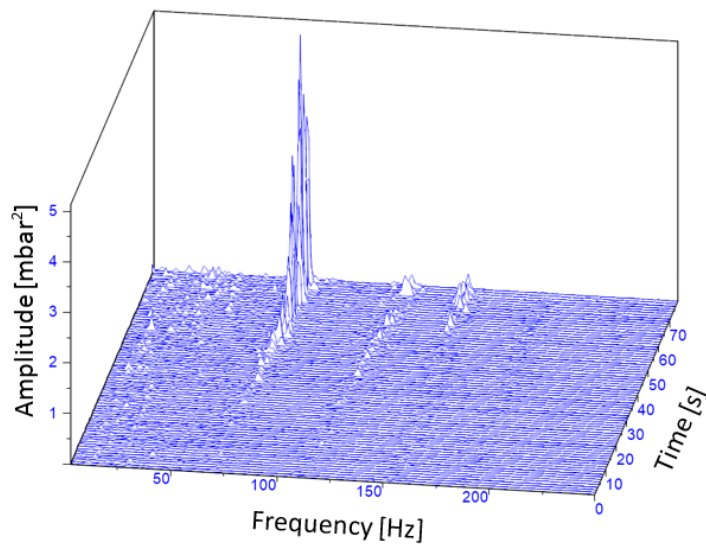
Figure 36: High and low range power spectral analysis for $0.06 \geq \phi \geq 0.05$ at 9000 rpm, 100% GMF (impeller outlet)

Further reduction of the flow coefficient displays little change in detected fluctuations until ϕ is closing on 0.03. Figure 37 displays the power spectrum for ϕ ranging from 0.04 to 0.03. After 60 seconds, which corresponds to a ϕ of 0.032, the occurrence of a powerful fluctuation is detectable at 75 Hz. This is equivalent to 50% of the rotational frequency

and as discussed in [Chapter 4](#) is an indication of part-span rotating stall due to flow separation in the impeller. As seen in [Figure 37a](#), the detected power fluctuation is greatly superior to the BPF in amplitude, and clearly marks the onset of instability.



(a) $0.04 \geq \phi \geq 0.03$, 2-3000 Hz



(b) $0.04 \geq \phi \geq 0.03$, 2-250 Hz

Figure 37: High and low range power spectral analysis for $0.04 \geq \phi \geq 0.03$ at 9000 rpm, 100% GMF (impeller outlet)

The onset of stall is further verified by a drop in compressor delivery pressure, and is displayed in [Figure 38](#) where the static to static compressor pressure ratio is plotted alongside ϕ . The drop is detectable after 60 seconds, which corresponds to a ϕ of 0.032.

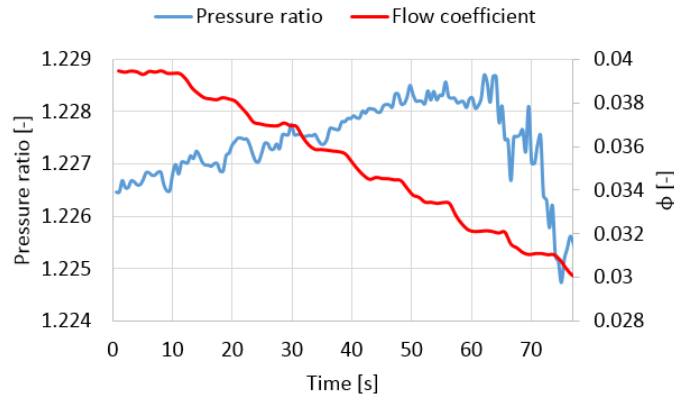


Figure 38: Compressor pressure ratio and ϕ versus time for the operating range $0.04 \geq \phi \geq 0.03$ at 9000 rpm, 100% GMF

Further reduction of the flow coefficient leads to additional instability development. In Figure 39 the spectral analysis as operation is approaching $\phi = 0.02$ is given.

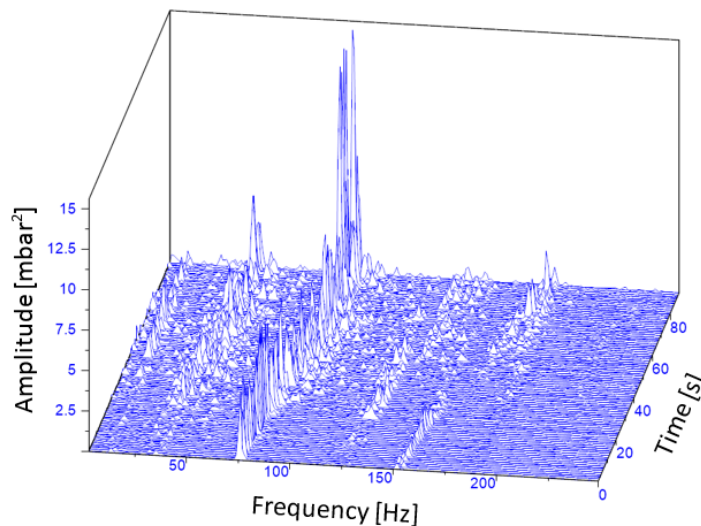


Figure 39: Low range power spectral analysis for $0.03 \geq \phi \geq 0.02$ at 9000 rpm, 100% GMF (impeller outlet)

The already detected pressure fluctuation at 75 Hz increases in magnitude, and fluctuations in the range of 30-60 Hz is appearing. The appearance of these fluctuations can be explained by an increase in stall cell span, and a transition into full-span stall, where stall is covering the majority of the impeller annulus. After 40 seconds, which corresponds to a ϕ of 0.026 a low frequency fluctuation appears at 10 Hz, indicating surge onset. As ϕ is closing on 0.02 an increase in all amplitudes are witnessed, indicating severe instability. The fact that inducer stall remains as the most powerful fluctuation even after surge onset implies that the occurring surge phenomenon is modified surge, which is a combination

of surge and stall, discussed in [Chapter 4](#). The absence of dominating surge frequencies is a result of the small downstream plenum, which effect was investigated by D. A. Fink et al. [14].

Indications of surge onset is further supported by the increased pressure ratio fluctuation observed in [Figure 40](#) after 40 seconds, which is seen to correspond with a flow coefficient of 0.026.

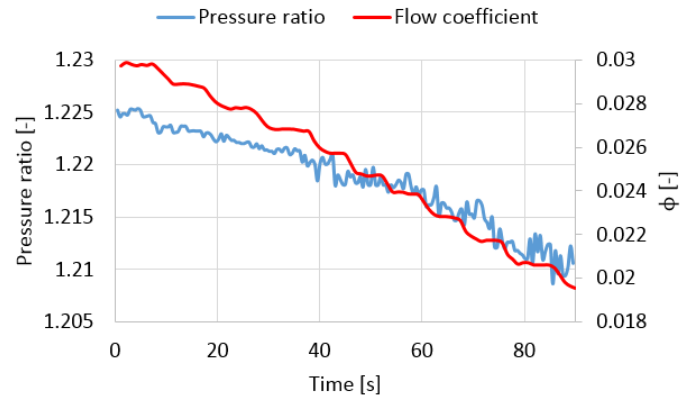


Figure 40: Compressor pressure ratio and ϕ versus time for the operating range $0.03 \geq \phi \geq 0.02$ at 9000 rpm, 100% GMF

7.1.1.2 Diffuser outlet

No distinct blade passing frequency is detected at the diffuser outlet. This is to be expected, as the pressure difference over the blades are quickly neutralized when the air is entering the diffuser. [Figure 41](#) provides the spectrum analysis of the operational range $0.05 \geq \phi \geq 0.04$.

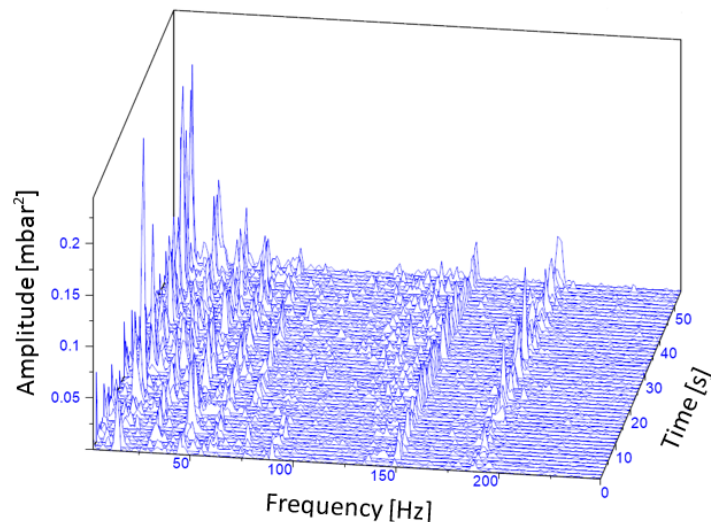
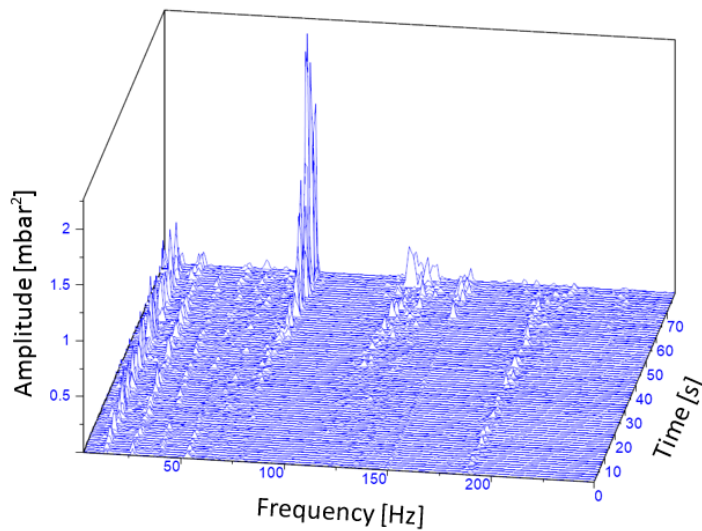


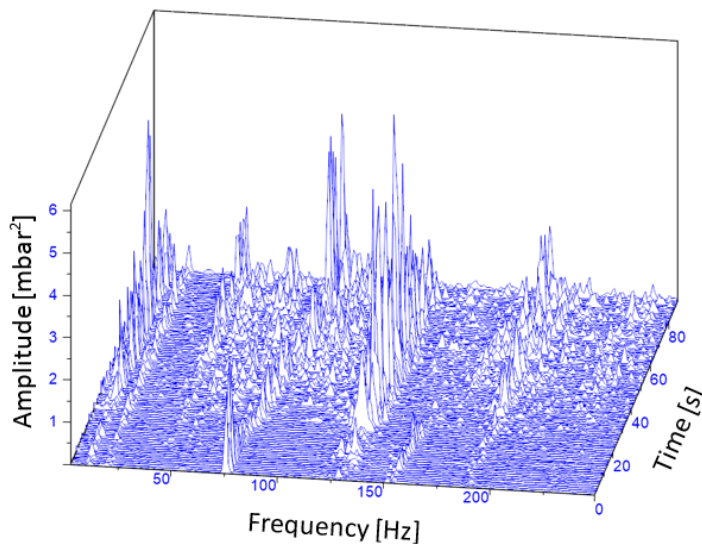
Figure 41: Low range power spectral analysis for $0.05 \geq \phi \geq 0.04$ at 9000 rpm, 100% GMF (diffuser outlet)

As seen, the only detected fluctuations are of low amplitude in the range up to 60 Hz. Fluctuations in this range were also detected at the impeller outlet, and are caused by instabilities in the diffuser, and possible rotating stall. However, because of the low amplitude, the fluctuations does not have a detectable effect on compressor operation, see [Figure 35](#), and are not considered as initiation of compressor instability.

As indicated by previously presented results, further reduction of the flow coefficient initiates impeller stall and compressor instability. Detected instability onset in the diffuser outlet appears at the same ϕ and frequency as for the impeller outlet, and the power spectrum is displayed in [Figure 42](#).



(a) $0.04 \geq \phi \geq 0.03$, 2-250 Hz



(b) $0.03 \geq \phi \geq 0.02$, 2-250 Hz

Figure 42: Low range power spectral analysis for $0.04 \geq \phi \geq 0.02$ at 9000 rpm, 100% GMF (diffuser outlet)

The detected stall initiating frequency is seen to have a lower amplitude than the equivalent stall frequency at impeller outlet. This supports the stated origin of the instability being separation in the impeller. The previously observed low frequent fluctuations are also clearly visible in [Figure 42a](#) leading up to instability, further indicating onset of diffuser rotating stall prior to impeller stall.

7.1.2 Instability classification

Power spectrum analysis indicated onset of impeller stall at $\phi = 0.032$ and possible diffuser rotating stall appearing prior to impeller instability. Threads were fitted circumferentially around the impeller inlet and in the diffuser to help classify detected instability phenomena. Pictures of instability onset in this section has been edited in Photoshop in order to highlight witnessed effects. Results will be presented for 9000 rpm, enabling reference to previously presented power spectral analysis.

7.1.2.1 Impeller inlet

In [Figure 43](#) captured instability onset at the inducer is given.

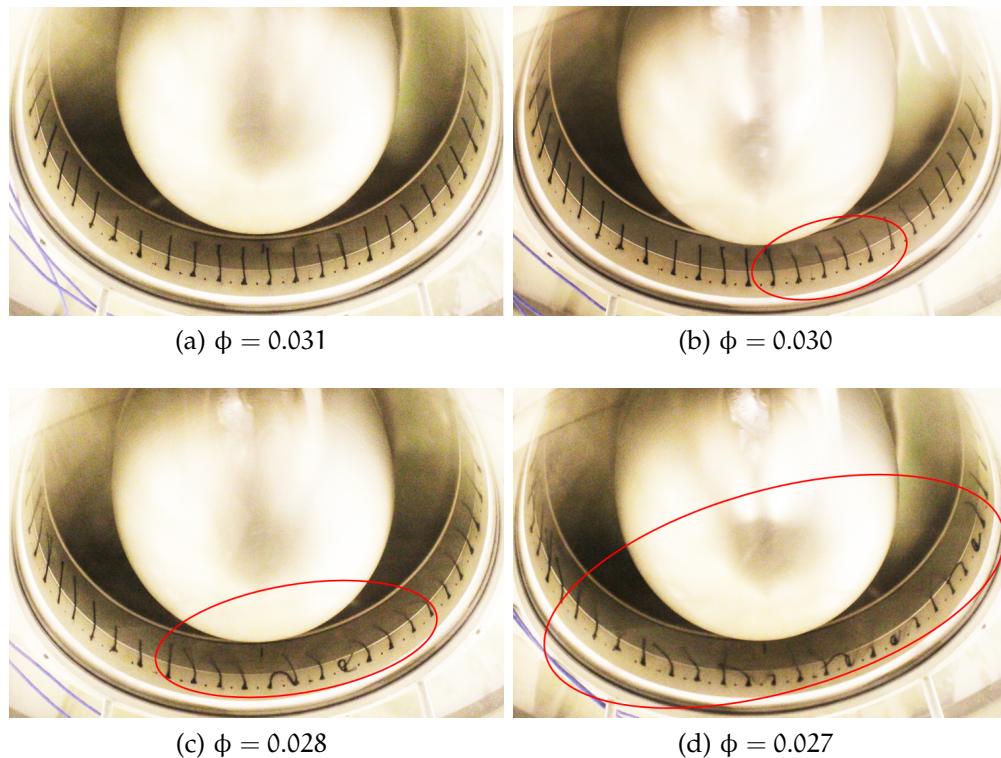


Figure 43: Spreading stationary stall region at inducer, 9000 rpm, 100% GMF

Detected inducer stall is visible at $\phi = 0.03$ encircled in [Figure 43b](#). This corresponds well with indicated impeller stall from power spectral

analysis at $\phi = 0.032$. A small deviation in detection point is expected given the small gap in between fitted threads and inducer. The stall region appears stationary, and as displayed in Figure 43, is expanding over the inducer annulus as ϕ is reduced. The fact that impeller stall appears as a stationary stall region is a strong indication of volute influence. The pressure buildup through the volute at low flow was discussed in detail in Section 3.4, and the possibility of a stationary stall region forming as a result was discussed in Section 4.1. The location of the stall cell corresponds well with the circumferential location of the volute tongue, which further indicates volute pressure buildup to be the initiating factor. The frequencies of detected pressure fluctuations indicate a rotating stall phenomena. The visible stationary stall region in Figure 43 is thus believed to act as an initiator for rotating stall, not detected by the fitted threads.

Reduction of ϕ below 0.27 quickly leads to a stall region completely covering the annulus, and the fully developed stall section is depicted in Figure 44.

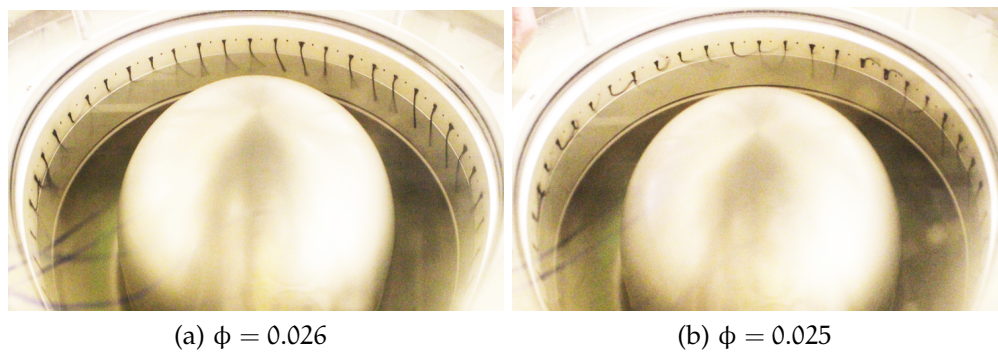


Figure 44: Completely spread stall region at inducer, 9000 rpm, 100% GMF

The stall region is observed to completely cover the inducer at $\phi = 0.026$ with corresponding annulus flow fluctuations observed at $\phi = 0.025$. Power spectral analysis indicated surge onset at $\phi = 0.026$ which corresponds well with a fully developed stall region. As a result, inducer stall is confirmed as a precursor to surge.

7.1.2.2 Diffuser

Threads were fitted in the diffuser to help clarify occurring diffuser instabilities. In Figure 45 detected instability onset in the diffuser is given.

Instability is first detected in the outer parts of the diffuser, already appearing at $\phi = 0.065$. Unstable flow in the volute entrance area is expected even at high ϕ as the entering radial velocity will lead to swirl. A small fluctuation is also detected at the impeller outlet. This is also

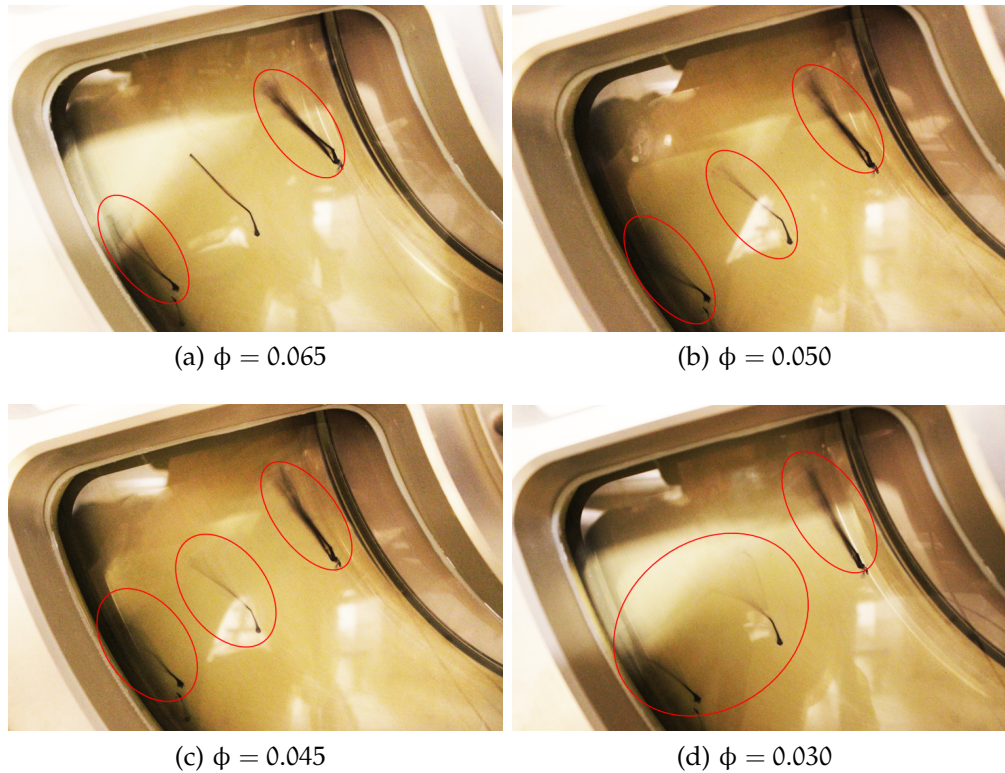


Figure 45: Detected diffuser instability at 9000 rpm, 100% GMF

expected, as there is a pressure variation over the impeller blade channel, as well as a possible jet/wake flow phenomenon out of the impeller. From power spectral analysis, low amplitude pressure fluctuations were detected at the diffuser outlet, starting from $\phi = 0.05$. In [Figure 45](#) velocity fluctuations are detected in the diffuser mid section at $\phi = 0.05$ and are seen to gradually increase as ϕ is lowered. Threads in the diffuser clearly indicate diffuser instabilities prior to inducer stall.

7.1.3 Flow regime

As discussed in [Chapter 6](#), 3-hole probe measurements were performed at 6000 and 9000 rpm at the impeller outlet and diffuser outlet in order to document dry gas flow regime. Presented results will be limited to 9000 rpm as similar effects were witnessed at lower speeds. The test matrix and locations for 3-hole probe measurements were given in [Section 6.1](#), respectively [Table 4](#) and [Table 3](#), and a graphical representation of test points on the compressor characteristic is plotted in [Figure 46](#).

Power spectral analysis indicated onset of impeller stall at $\phi = 0.032$, and diffuser instabilities appearing at $\phi = 0.05$. From [Figure 46](#) it is thus clear that 3-hole probe measurements were taken in both stable and unstable operation. The stable range consists of measurements between

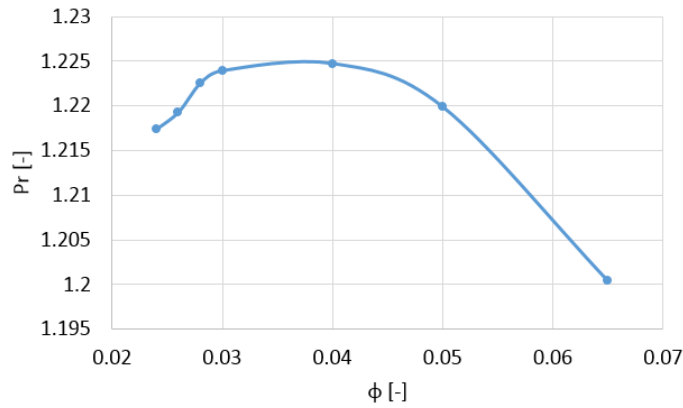


Figure 46: Graphical representation of test points on the compressor characteristic at 9000 rpm, 100% GMF

$\phi = 0.065$ and $\phi = 0.04$, while the unstable range is from $\phi = 0.03$ and down. Results will be presented separately for the impeller outlet and diffuser outlet, starting with the impeller.

7.1.3.1 Impeller outlet flow regime

In [Figure 47](#) values for detected dynamic pressure and flow angle at impeller outlet are given.

In the stable operating range, dynamic pressure and corresponding flow angle is seen to increase at reduced ϕ . This result was expected given the impeller's backsweep and the impeller outlet velocity's dependence on volumetric flow discussed in [Chapter 3](#). In [Figure 47b](#) the flow angle is seen to increase towards the diffuser shroud. This indicates the presence of a wake region in the impeller shroud area, as mentioned in [Section 6.1](#), which again was expected from reviewed literature. Directly after the onset of impeller stall, a jump in the dynamic pressure at the shroud is witnessed in [Figure 47c](#). The jump in velocity is accompanied with a jump in flow angle to 90° , see [Figure 47d](#), which clearly indicates a fully separated stagnant wake region at the impeller shroud area. A flow angle of 90° is equivalent to no flow in the radial direction, and stall is thus leading to a potential backflow region forming at the impeller shroud. The impeller shroud was pointed out as a high risk region for flow separation in previously reviewed literature, and formation of the stagnant wake region was expected.

As ϕ is further reduced, no increase in dynamic pressure is detected. In fact, [Figure 47c](#) is displaying a slight decrease. This is further confirming that the compressor is operating in the unstable range, as effects of instability will only increase in magnitude and flow fluctuation is the result. The flow angle is seen to increase in the hub region of the diffuser,

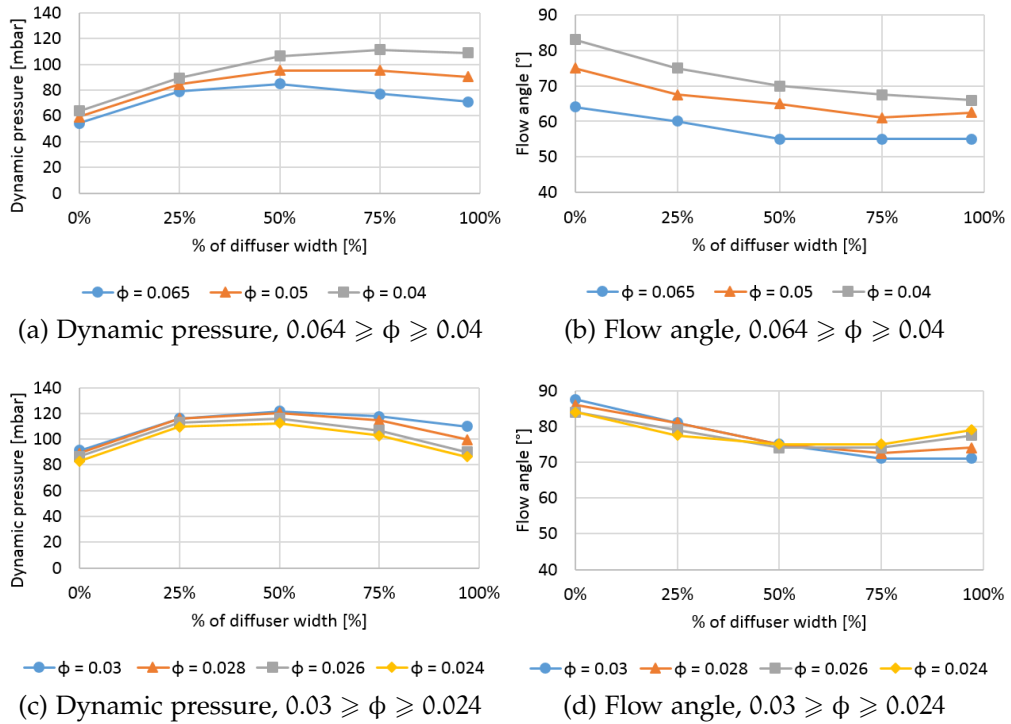


Figure 47: Three hole probe measurements of dynamic pressure and flow angle at impeller outlet, 9000 rpm, 100% GMF

explained by an enlarged wake region in the impeller, moving from impeller shroud to hub along the suction side of the impeller blade.

7.1.3.2 Diffuser outlet flow regime

In [Figure 48](#) values for detected dynamic pressure and flow angle at diffuser outlet are given.

In contrast to the impeller outlet, velocity at the diffuser outlet decreases as ϕ is reduced. This is expected as lowering ϕ is reducing the relative velocity leaving the impeller leading to a longer flow path in the diffuser and increased pressure recovery, in other words, the velocity decreases at the diffuser outlet. The phenomenon was discussed in [Chapter 3](#), and said flow angle increase is clearly visible in [Figure 48b](#). The effect of boundary layer deceleration is also clearly visible, as the dynamic pressure is reduced at both shroud and hub. The velocity profile remains fairly unchanged as the compressor is moved into unstable operation, however, a jump in the flow angle near the diffuser shroud wall is detected. Results have already pointed to a backflow region forming in the impeller shroud, and the flow angle measurements indicates an elongation of this region through the diffuser. Little change is detected in the flow angle as the compressor is moved further into instability,

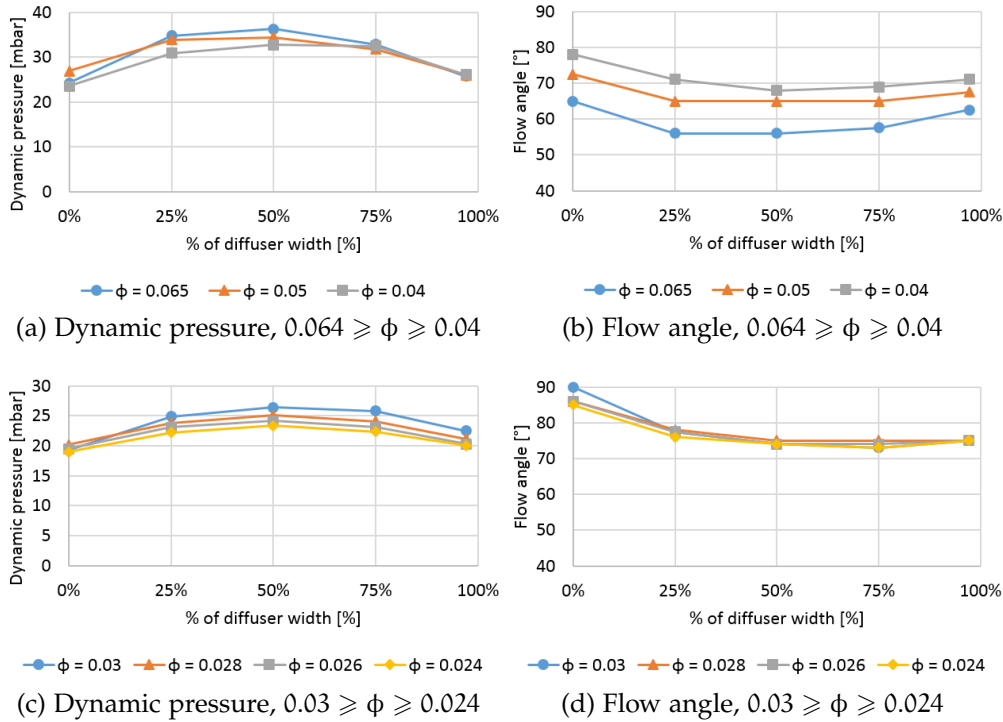


Figure 48: Three hole probe measurements of dynamic pressure and flow angle at diffuser outlet, 9000 rpm, 100% GMF

which establishes the diffuser shroud as the region where backflow occurs.

Results from spectral analysis pointed to instabilities in the diffuser prior to stall initiation in the impeller. In Table 10 calculated measurement deviations in detected dynamic pressures are given.

Table 10: Deviation in diffuser outlet dynamic pressure measurements

WIDTH:	0%	25%	50%	75%	100%
ϕ	Dynamic pressure deviation				
0.065	3.73%	1.71%	1.13%	1.43%	2.37%
0.05	10.68%	4.90%	2.24%	1.60%	3.32%
0.04	18.98%	16.17%	9.80%	3.05%	11.82%
0.03	7.31%	8.24%	5.28%	4.29%	3.79%

A distinct increase in deviation is noted at the diffuser shroud at $\phi = 0.05$ which has further increased at $\phi = 0.04$. This increase in measurement deviation supports previously presented results indicating diffuser rotating stall prior to impeller stall. An explanation of the decrease in measurement deviation after onset of impeller stall is that velocity in the developed wake region will fluctuate between positive

and negative radial velocity, and with a total velocity angle of 90° this will not lead to major fluctuations in detected velocity. However, rotating stall will enforce significant fluctuation of the absolute velocity, which is easier to detect.

7.2 WET OPERATION

In the following section all results regarding wet operation will be presented. Results include determination of impeller multiphase flow regime based on impeller coating, and direct visualization of occurring multiphase phenomena in the diffuser. The effect of labyrinth leakage on previously witnessed annulus ring formation is also thoroughly documented. As for dry operation, a detailed spectral analysis of instability onset will be presented first, determining instability phenomena, operational range and wet gas effect on instability onset.

7.2.1 Power spectral analysis

Results are presented in the same manner as for dry operation, and limited to 9000 rpm. Testing was concentrated at 90% GMF, focusing on explaining witnessed results, as previous testing already has indicated an enhancement of occurring effects at lower GMF.

7.2.1.1 Impeller outlet

In [Figure 49](#) the high range power spectral analysis at impeller outlet is shown for a flow coefficient ranging from 0.06 to 0.05.

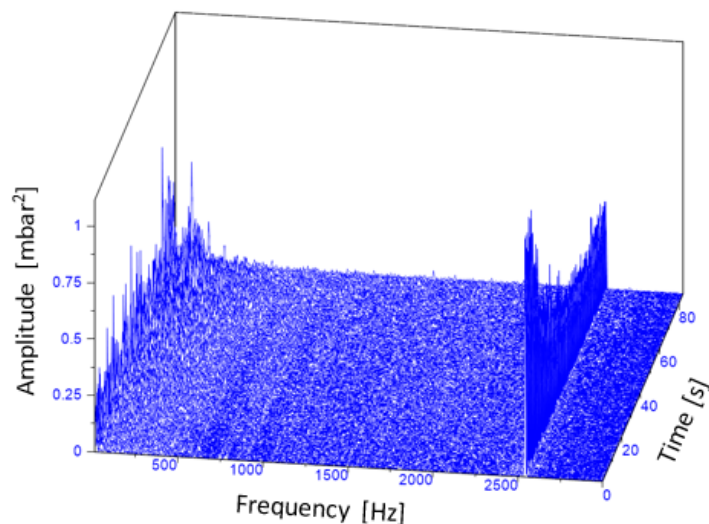
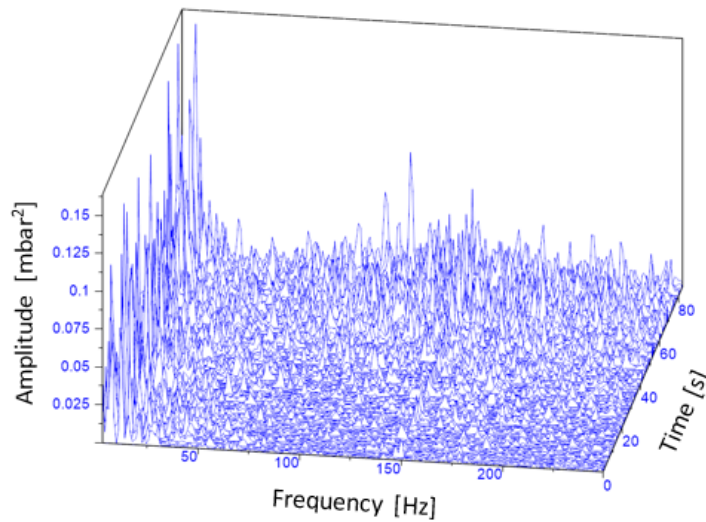
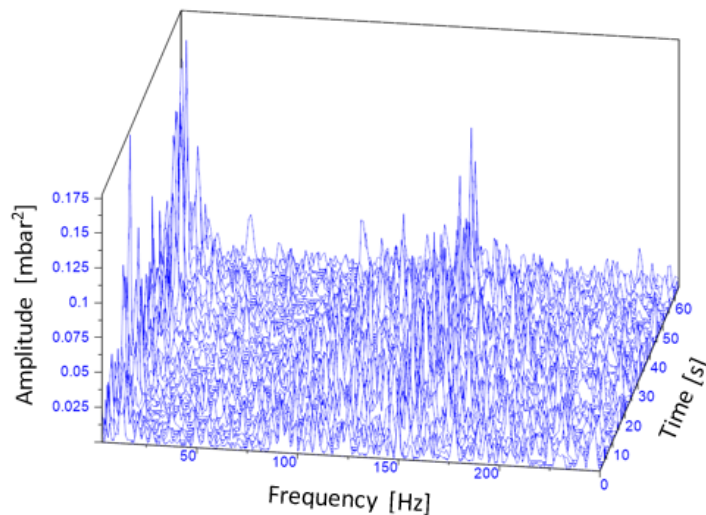


Figure 49: High range power spectral analysis for $0.06 \geq \phi \geq 0.05$ at 9000 rpm, 90% GMF (impeller outlet)

The high range analysis reveals the BPF as the dominating pressure fluctuation. In Figure 50 some low amplitude fluctuations are visible in the low range spectrum, but no distinct frequencies are present. It is however expected to see a pressure fluctuation at 150 Hz equal to the impeller revolution speed, as was the case for dry operation. The absence of this frequency, and the presence of what seems to be a more distributed area of fluctuations points to a distorted pressure equalization, which indicate a multiphase mixing area.



(a) $0.06 \geq \phi \geq 0.05$, 2-250 Hz



(b) $0.05 \geq \phi \geq 0.04$, 2-250 Hz

Figure 50: Low range power spectral analysis for $0.06 \geq \phi \geq 0.04$ at 9000 rpm, 90% GMF (impeller outlet)

Presented dry gas results displayed onset of impeller rotating stall at $\phi = 0.032$. In Figure 51 the low range spectral analysis as ϕ is reduced from 0.04 to 0.02 is displayed.

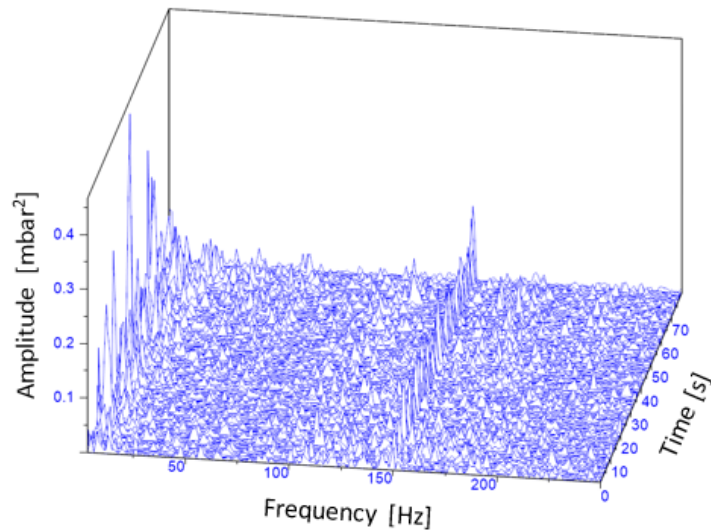
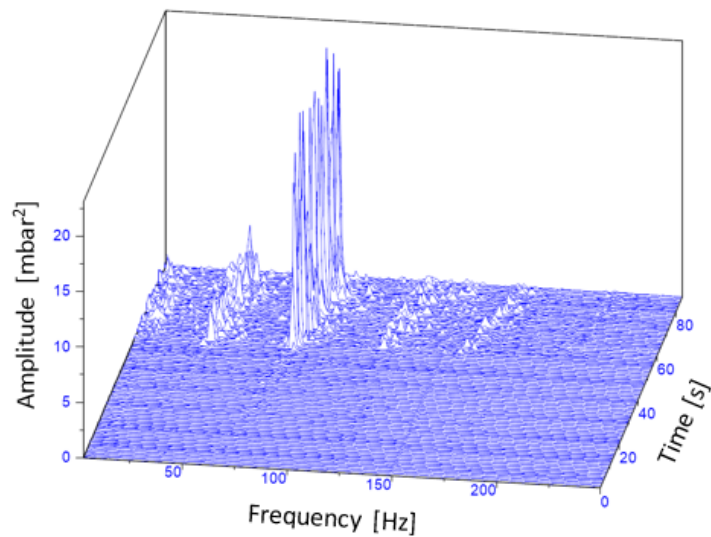
(a) $0.04 \geq \phi \geq 0.03$, 2-250 Hz(b) $0.03 \geq \phi \geq 0.02$, 2-250 Hz

Figure 51: Low range power spectral analysis for $0.04 \geq \phi \geq 0.02$ at 9000 rpm, 90% GMF (impeller outlet)

A delayed onset of instability in wet conditions is evident, as no onset of stall is detected in [Figure 51a](#). A simultaneous onset of all previously observed dry gas instability frequencies is however detected in [Figure 51b](#), indicating direct transition into modified surge. The onset of instability is detected after 55 seconds, corresponding to $\phi = 0.024$. A big increase in surge margin is detected for wet operation, as instability onset is moved from $\phi = 0.032$ to $\phi = 0.024$.

Further indications of direct transition into modified surge is observed in [Figure 52](#) where the compressor static to static pressure ratio with corresponding ϕ is given for the operational range $0.03 \geq \phi \geq 0.02$. An abrupt increase in pressure ratio fluctuation is observed after 55

seconds, corresponding to $\phi = 0.025$. No drop in pressure ratio is witnessed prior to the abrupt initiation of large amplitude fluctuations, indicating an absence of pre occurring stall.

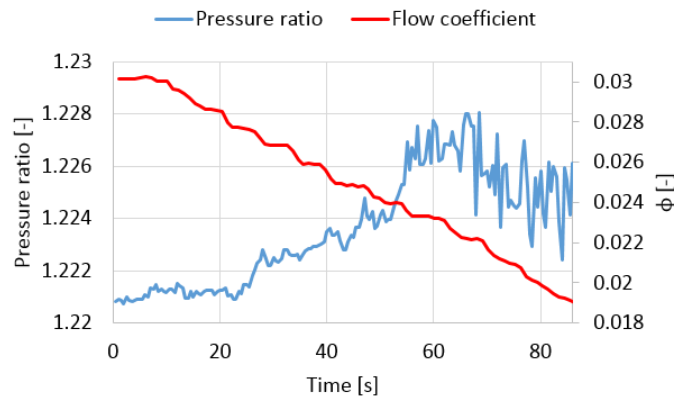


Figure 52: Compressor pressure ratio and ϕ versus time for the operating range $0.03 \geq \phi \geq 0.02$ at 9000 rpm, 90% GMF

7.2.1.2 Diffuser outlet

As for dry operation, no distinct blade passing frequency is detected at diffuser outlet during wet operation. Figure 53 provides the spectral analysis of the operational range $0.05 \geq \phi \geq 0.04$.

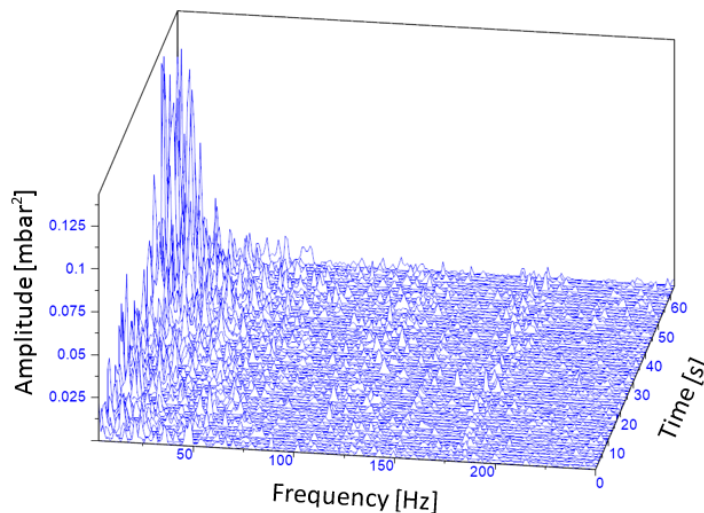
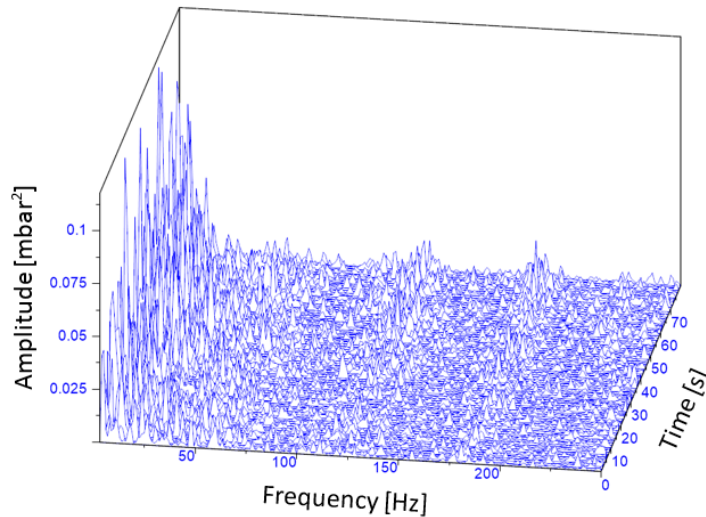


Figure 53: Low range power spectral analysis for $0.05 \geq \phi \geq 0.04$ at 9000 rpm, 90% GMF (diffuser outlet)

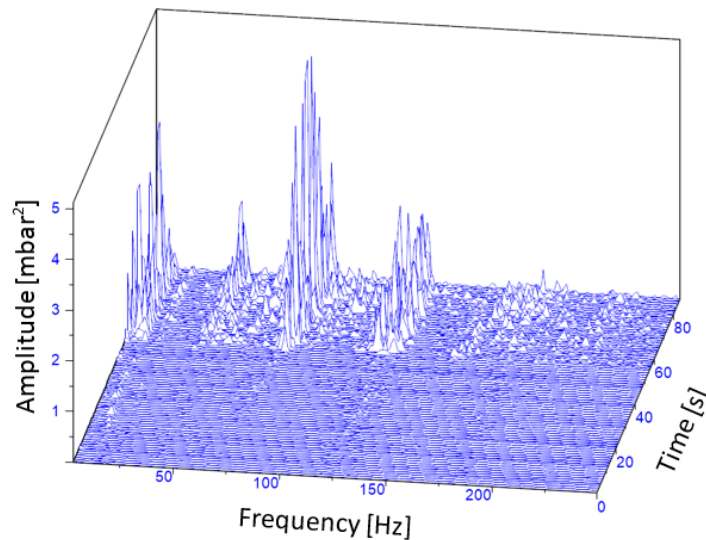
No distinct frequencies are detected, and the only witnessed fluctuations appear at low amplitude in the range up to 50 Hz. This is fairly equal to observed fluctuations in dry operation, however the fluctuations are more evenly dispersed, again pointing to multiphase inter-

action and a distorted flow regime. The fluctuations are not affecting overall compressor stability, as the amplitudes are too low.

As indicated by impeller outlet analysis, further reduction of the flow coefficient initiates a simultaneous onset of previously witnessed instability phenomena. Detected instability onset in the diffuser occurs at the same ϕ as in the impeller, but again with a lower amplitude, further indicating the impeller as the point of initiation. The onset of instability is displayed in Figure 54.



(a) $0.04 \geq \phi \geq 0.03$, 2-250 Hz



(b) $0.03 \geq \phi \geq 0.02$, 2-250 Hz

Figure 54: Low range power spectral analysis for $0.04 \geq \phi \geq 0.02$ at 9000 rpm, 90% GMF (diffuser outlet)

Again, the delayed onset is clearly visible, as no instability is detected in Figure 54a.

In [Section 3.4](#) the characteristic pressure buildup in the volute at low flow was explained. A delay in the pressure buildup at wet operation was expected to occur as a result of reduced pressure recovery and a shorter flow path through the diffuser. In dry operation, a stationary stall zone was observed at the volute tongue circumferential position, initiating inducer stall. The delayed onset of instability in wet operation, and the absence of a characteristic stall frequency appearing prior to modified surge, are both strong indications of delayed volute pressure buildup to be a contributing factor to witnessed results.

7.2.2 *Multiphase flow regime*

Multiphase flow regime has been investigated at three locations over the impeller stage. Presented results will start with impeller inlet flow regime and the impact of labyrinth leakage at reduced flow. Determination of multiphase flow regime in the impeller channel based on performed impeller coating will be presented, finishing with a detailed investigation of occurring multiphase flow phenomena in the diffuser.

7.2.2.1 *Impeller inlet flow regime*

In the author's previous work, the formation of an extending annulus ring of liquid was observed in relation to wet instability [35]. A thorough investigation of occurring instability phenomena in dry conditions has already been carried out, indicating a stationary stall region at the lower parts of the inducer to initiate rotating stall. Investigation of wet instability displayed a later instability onset, characterized by a direct transition into modified surge. Onset of surge will affect impeller inlet flow regime, but as pointed out in [Section 3.5](#), leakage from the labyrinth seal is a possible contributor.

To investigate the effect of labyrinth leakage fluorescent liquid was injected through a drilled hole in the diffuser shroud. The test procedure was explained in [Section 6.5](#) where the corresponding test matrix is included in [Table 8](#).

On the following two pages, a detailed picture series showing the transition in impeller inlet flow regime as the compressor is taken from stable operation into surge is given. Presented results are limited to 9000 rpm as similar effects were witnessed at lower speeds. [Figure 55](#) displays flow regime for the range $0.05 \geq \phi \geq 0.03$, while [Figure 56](#) covers the remaining range $0.028 \geq \phi \geq 0.022$. For each ϕ the flow regime is depicted with and without fluorescent injection, clearly indicating the effect of labyrinth seal leakage.

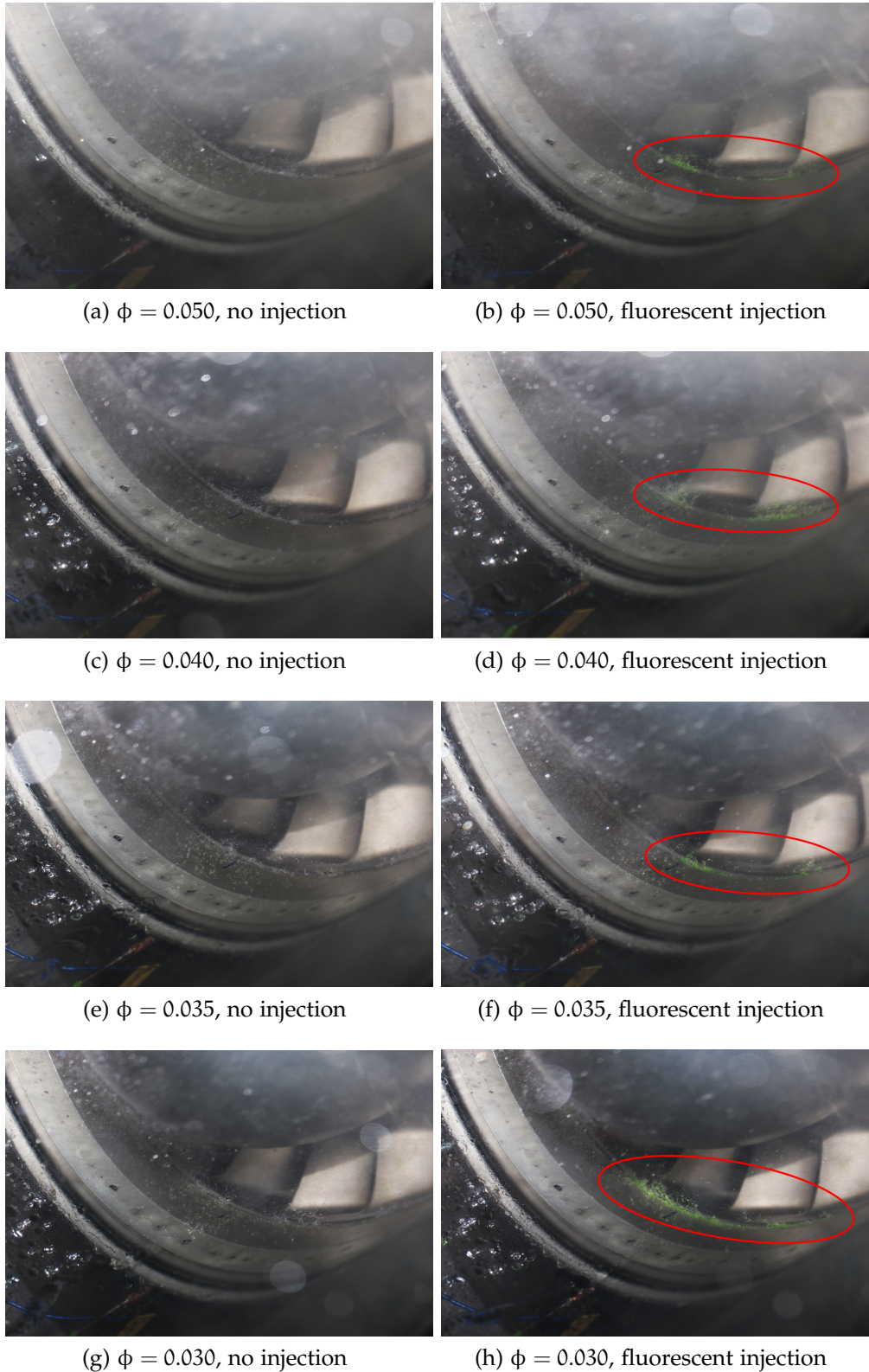


Figure 55: Detected flow phenomenon and labyrinth leakage influence at impeller inlet in the operating range $0.05 \geq \phi \geq 0.03$ at 9000 rpm, 90%GMF

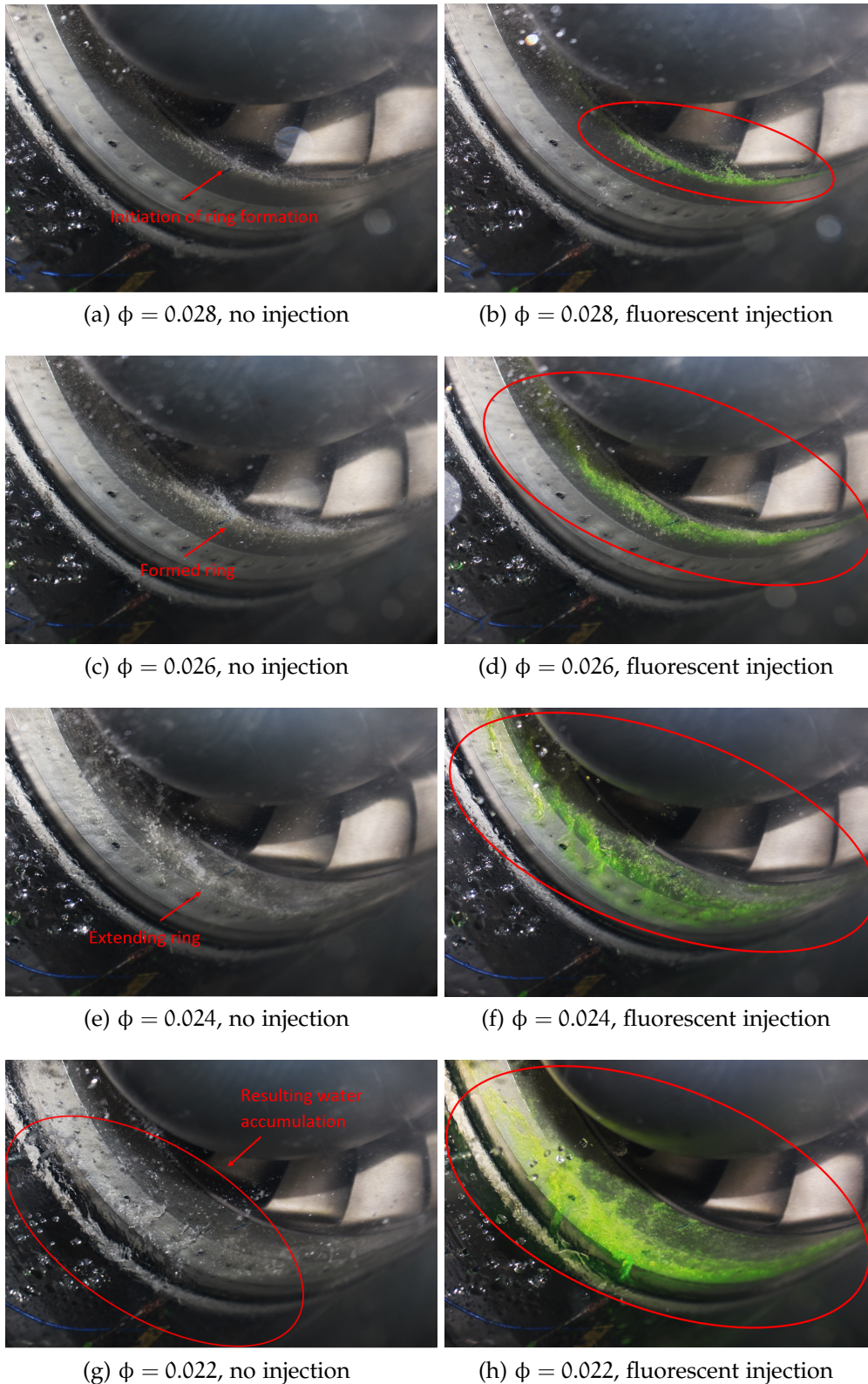


Figure 56: Detected flow phenomenon and labyrinth leakage influence at impeller inlet in the operating range $0.028 \geq \phi \geq 0.022$ at 9000 rpm, 90%GMF

No distinct change in inlet flow regime is witnessed between $\phi = 0.05$ and 0.03 . Labyrinth leakage is present, but has no significant impact on flow behaviour. Leakage appears constant as ϕ is reduced to 0.035 , but an increase in detected leakage is visible at $\phi = 0.03$ in [Figure 55h](#). Further reduction of the flow initiates formation of the previously discussed annulus ring of liquid. The initiation is highlighted in [Figure 56a](#), and with it, an increase in detected leakage is clearly visible. At $\phi = 0.026$ the ring has formed, and substantial leakage is detected. Spectral analysis indicated onset of modified surge at $\phi = 0.024$. As seen in [Figure 56e](#) the onset of surge leads to an expansion of the previously formed ring, pushing it further upstream the inducer. The onset of surge leads to a substantial increase in leakage, visible in [Figure 56f](#). Further flow reduction leads to water accumulation upstream the impeller inlet, and the severity of labyrinth leakage is clearly visible in [Figure 56h](#).

From presented results it is clear that labyrinth leakage has an impact on the witnessed annulus ring formation. Initiation of the ring formation is seen to appear at the inducer bottom region, suggesting increased leakage in this region. The possible influence of volute pressure buildup on labyrinth leakage was discussed in [Section 3.5](#), and the position corresponds well with the circumferential position of the volute tongue. Given injection was executed through a hole located underneath the impeller inlet, the position of appearing labyrinth leakage can not be confirmed as a result of volute pressure buildup, but it is a strong indication.

Performed experiments can not conclude whether labyrinth leakage is the sole purpose of the witnessed annulus ring or not, but leakage is seen as a definite contributor to the phenomenon. Further research is needed on order to fully determine the cause of formation.

7.2.2.2 *Impeller channel flow regime*

The witnessed delayed instability onset in wet conditions is believed to occur as a result of slower pressure buildup through the volute as well as phase segregation in the impeller channels. In order to detect possible phase segregation, the impeller was coated with a water soluble green paint, and subjected to wet operation. The test procedure was clearly explained in [Section 6.4](#). In [Section 3.2](#) force equations for flow through the impeller were derived, which indicated a liquid phase concentration on the hub/pressure side of the impeller channel.

In [Figure 57](#) the inducer is depicted before and after test execution. Coating has not been removed from the suction side of the inducer blades, indicating a segregation of the phases in the inducer. Coating is

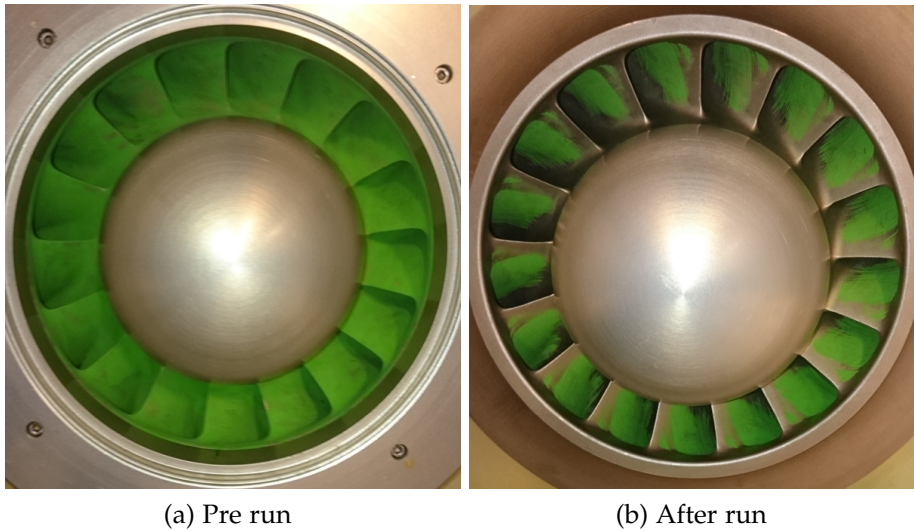


Figure 57: Inducer before and after 5 minute run at 6000 rpm, 90% GMF

seen to be removed at the leading edge of the blades, which is expected as the leading edge will hit incoming water droplets.

In [Figure 58](#) a close-up photo of the inducer is given. No coating is visible at the hub and pressure side of the impeller channel, indicating water flow at these surfaces. Coating is still visible at the shroud initiation, a further sign of segregation.

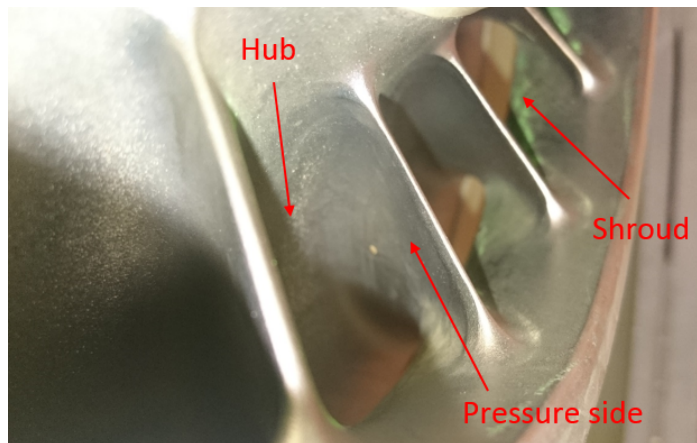


Figure 58: Impeller inlet section after 5 minute run at 6000 rpm, 90% GMF

Another close-up picture is given in [Figure 59](#), depicting the hub, shroud and suction side of the impeller channel. It is clearly visible that no water has flown along the shroud/suction side of the impeller blade, while the hub indicates an opposite trend. The same phenomenon was observed in all inspected channels.

The last picture, [Figure 60](#), display the impeller outlet section before and after test execution. Again, the hub and pressure side of the im-

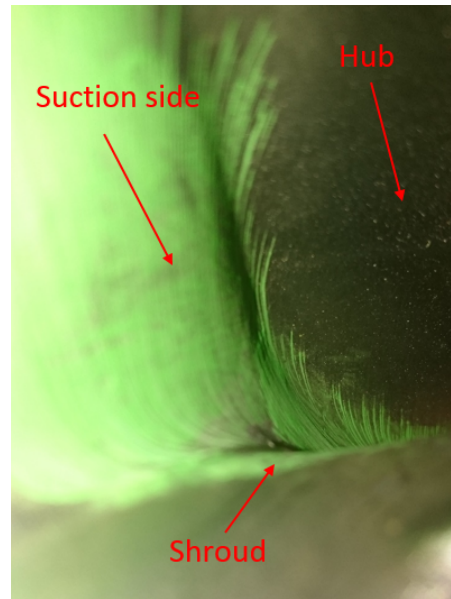


Figure 59: Impeller channel after 5 minute run at 6000 rpm, 90% GMF

Impeller channel is cleared of coating, implying water flow at the surfaces, while the suction side has coating intact.

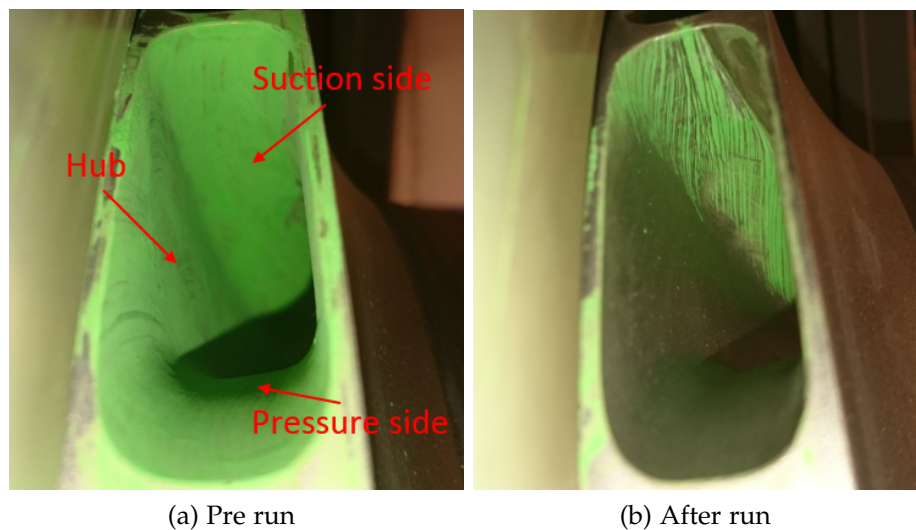


Figure 60: Impeller outlet section before and after 5 minute run at 6000 rpm, 90% GMF

Results give a clear indication of a segregated flow regime in the impeller. Water appears to flow along the pressure/hub-side of the impeller channel, while the shroud/suction-side shows little sign of water contact. Presented results only indicate flow regime at the impeller channel surfaces, but prove a segregation of the phases, which can help explain delayed onset of instability. The test was performed at $\phi = 0.065$ and further testing should be initiated in order to investigate potential

changes in flow regime at lower flows. In order to get an overview of the entire channel flow regime, optical visualization techniques, discussed in [Chapter 5](#) should be applied, and is subject for further testing.

7.2.2.3 Diffuser flow regime

Flow phenomena in the diffuser was documented at 90% GMF and 9000 rpm from stable operation down to initiation of surge; previously documented by spectral analysis to occur at $\phi = 0.024$. As discussed in [Section 6.6](#), stroboscope and different light settings were used in order to capture multiphase impact on diffuser flow phenomena.

In [Figure 61](#) still photos of flow leaving the impeller, captured with the use of a stroboscope, are given for reduced ϕ .

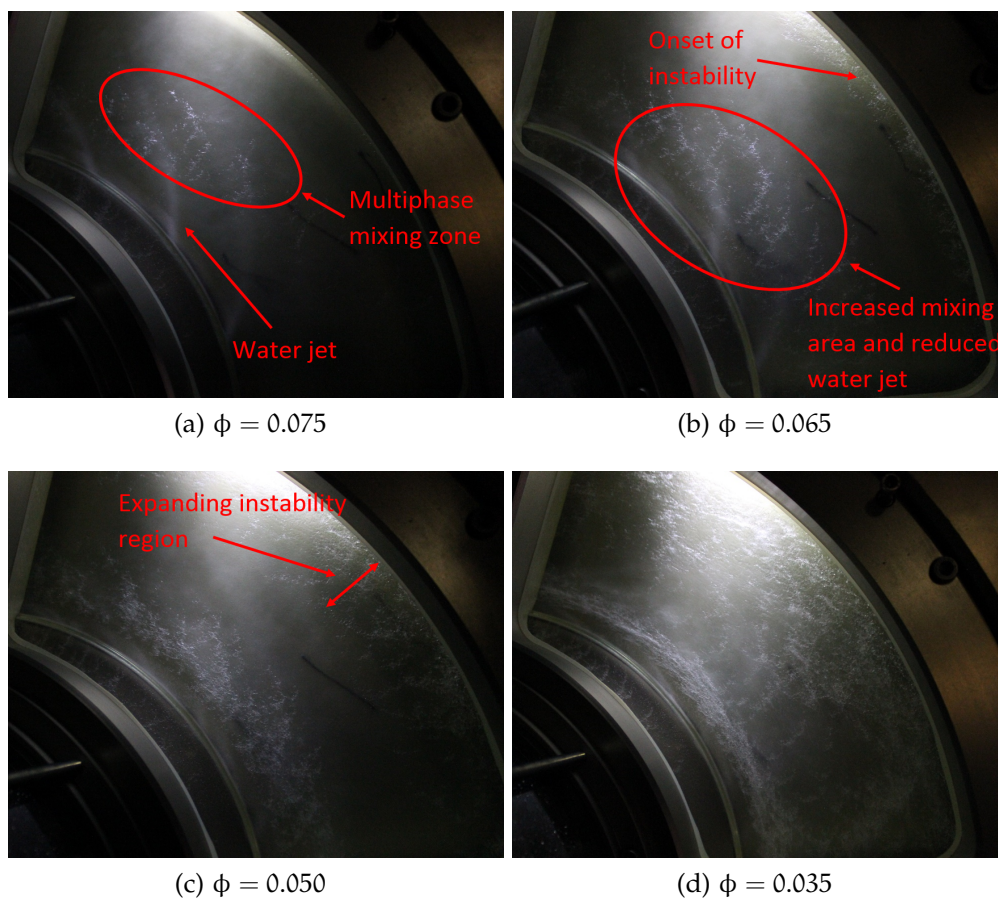


Figure 61: Stroboscope induced impeller outlet flow regime at 9000 rpm, 90% GMF

Distinct water jets are visible in [Figure 61a](#). Results confirming phase segregation in the impeller was presented in the previous section, and witnessed water jets further confirms the findings. The jets are seen to disperse after a certain distance into the diffuser resulting in a distorted flow area indicating mixing of the phases. As ϕ is reduced, indicated

wakes are observed to shorten in length, and detected mixing area is increasing. The effect is explained by the different behaviour of the phases through the diffuser, as discussed in [Chapter 3](#). The higher inertia of the water and absent compressibility effects will shorten the water's flow path. Air will however tend to follow a larger logarithmic spiral angle, and collides with passing water particles. The effect will be more apparent at lower flow, as the reduced relative velocity at impeller outlet will greatly increase the air's flow path while at the same time increase its absolute velocity entering the diffuser.

In addition to a larger mixing area, the occurrence of an unstable region is detectable in the outer parts of the diffuser. The observed instability region is seen to form in [Figure 61b](#), and expand further down through the diffuser as ϕ is reduced. At $\phi = 0.035$ a completely distorted flow regime is visible, indicating highly unstable flow in the diffuser.

Detected flow regime in the diffuser is given in [Figure 62](#).

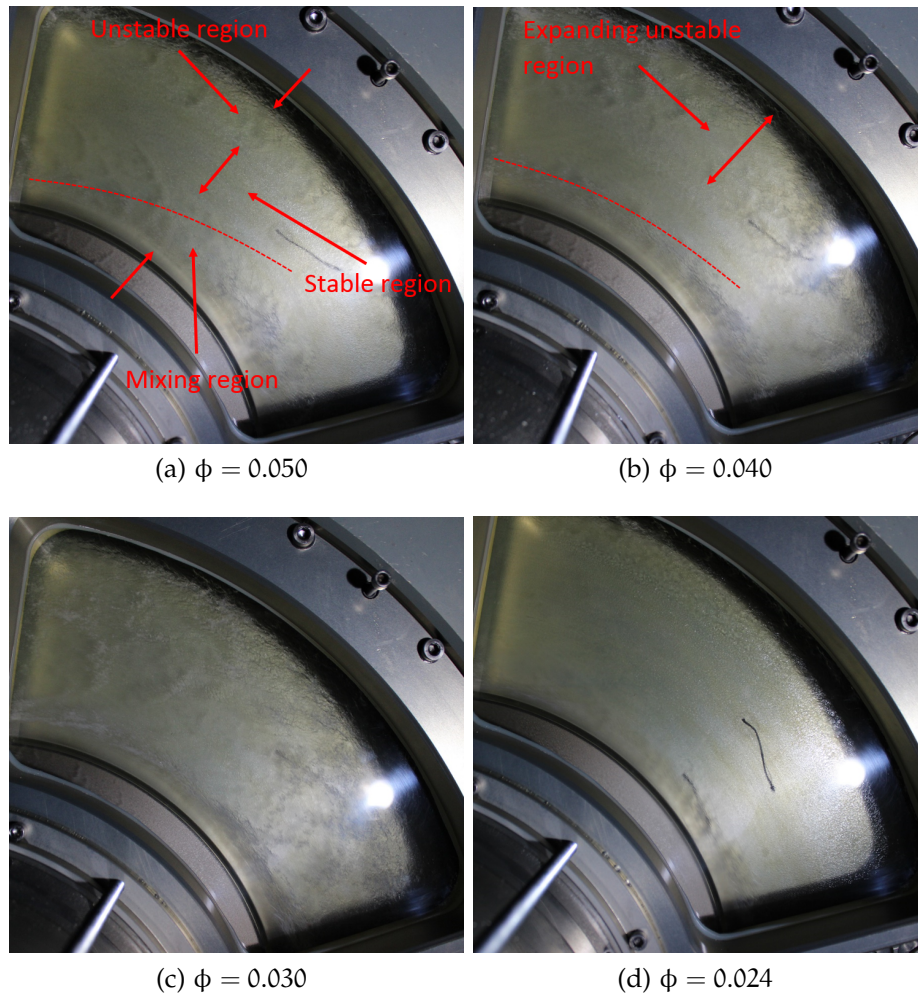


Figure 62: Diffuser flow regime at 9000 rpm, 90% GMF

As was seen in [Figure 61](#), a distinct mixing and unstable region is visible at $\phi = 0.05$. The dotted line in [Figure 62a](#) and [Figure 62b](#) indicates the flow direction, and the flow angle is seen to increase at reduced ϕ . In between the mixing and unstable region, a band of stable flow is observed. As ϕ is reduced, the unstable region expands further down the diffuser and a completely distorted flow regime is visible at $\phi = 0.03$. Spectral analysis indicated onset of modified surge at $\phi = 0.024$. A distinct change in diffuser flow regime is visible in [Figure 62d](#), as the flow changes from highly distorted to what seems like a vibrating stationary regime. The change in flow regime indicates rapid radial fluctuation in the diffuser, resulting from compressor surge. What is also clearly visible is that water accumulates in the low energy region at diffuser shroud, as was concluded by Lars Brenne [5].

Increased slip at low flows was mentioned as a possible scenario when multiphase effects on impeller channel flow was discussed in [Section 3.2.4](#). Acquired results does not provide sufficient data in order to document this, as a potential change in water jet angle is difficult to observe. Another shortcoming of gathered results is the documentation of flow regime in the traverse direction over the diffuser. Dry gas results indicated a separated flow region along the shroud side of the diffuser. Wet gas results indicate a similar phenomena, but further research is needed in order to confirm this.

CONCLUSION AND RECOMMENDED WORK

This thesis has documented occurring impeller stage instabilities at the NTNU wet gas compressor test rig. Documentation has been based on a thorough literature review and performed tests. The flow regime in dry and wet conditions has been documented up to initiation of instability, and the following conclusions can be drawn from presented results.

8.1 DRY OPERATION

8.1.1 *Instability onset*

Instability was observed to initiate through a stationary stall region circumferentially aligned with the volute tongue's location. A characteristic stall frequency of 75 Hz was detected at $\phi = 0.032$, which indicated impeller rotating stall to be the occurring phenomena. Reduction of ϕ initiated modified surge, thus confirming stall as a precursor to witnessed surge onset. Signs of diffuser rotating stall was found prior to impeller instabilities, however no sign of reduced compressor performance was witnessed at onset. Diffuser rotating stall is thus not regarded as a limiting operational parameter.

8.1.2 *Flow regime*

Detected dynamic pressure was found to increase in sync with measured logarithmic spiral angle at the impeller outlet for reduced flow. The result corresponded with expected behaviour from performed literature review. A substantial flow angle increase was detected at the diffuser inlet shroud, resulting from a characteristic wake formation in the shroud-section of the impeller. A fully separated wake region was detected at instability onset, which spread towards the hub side at further flow reduction.

Diffuser flow regime displayed an expected deceleration close to the hub and shroud wall, as well as an overall velocity decrease at lower flows. Large fluctuations in detected dynamic pressure was visible at the shroud area, indicating possible diffuser rotating stall prior to impeller instability. At instability onset, a tangential flow region appeared in the diffuser shroud area, indicating boundary layer separation and flow fluctuation.

8.2 WET OPERATION

8.2.1 *Multiphase instability onset*

A delayed instability onset was documented for wet operation as detected initiation point moved from $\phi = 0.032$ in dry conditions to $\phi = 0.024$ at 90% GMF. An absence of pre-occurring rotating stall was witnessed, and direct transition into modified surge was observed. Delayed onset was believed to occur as a result of postponed volute pressure buildup and detected phase segregation taking place in the impeller channels.

8.2.2 *Multiphase flow regime*

The previously documented annulus ring of liquid forming at impeller inlet in relation to wet instability has been subject for thorough investigation. Leakage from the labyrinth seal has been documented as a major contributor to the phenomenon, as significant leakage was detected at low flows.

A segregated flow regime in the impeller channels was documented at stable operation. Water was found to flow along the hub/pressure side of the impeller channels, while air was reserved to the shroud/suction region. Further indication of segregated flow was visible at impeller outlet, displaying significant water jets leaving the impeller. A mixing region was observed at the jets' dispersal point, increasing in size as flow was reduced. Diffuser instabilities were first witnessed in the outer parts of the diffuser, expanding inwards at reduced flow. A significant change in diffuser flow phenomena was documented at the onset of surge, shifting from a highly distorted flow, to a radially fluctuating regime, visible at the diffuser shroud.

8.3 RECOMMENDED FURTHER WORK

A strong indication of volute interference on instability onset in dry conditions has been indicated in this thesis. A recommendation for further work is detailed pressure measurements around the volute and inducer circumference in order to verify occurring pressure buildup and its detectability through the compressor. A similar investigation is encouraged for wet operation, in order to further verify delayed volute pressure buildup as a contributor to delayed instability onset in wet conditions.

A segregated flow regime has been documented on the impeller channel walls at stable operation in wet conditions. Further research is needed

i order to establish a complete blade channel flow regime. The impeller investigated in this thesis was shrouded, and visibility of occurring flow phenomena was thus limited. Investigation of an unshrouded or transparently shrouded impeller is highly recommended, and will allow for further investigation of multiphase impeller channel flow phenomena. A continuation of presented coating tests, establishing any difference in detected phase segregation at low flow is of further relevance.

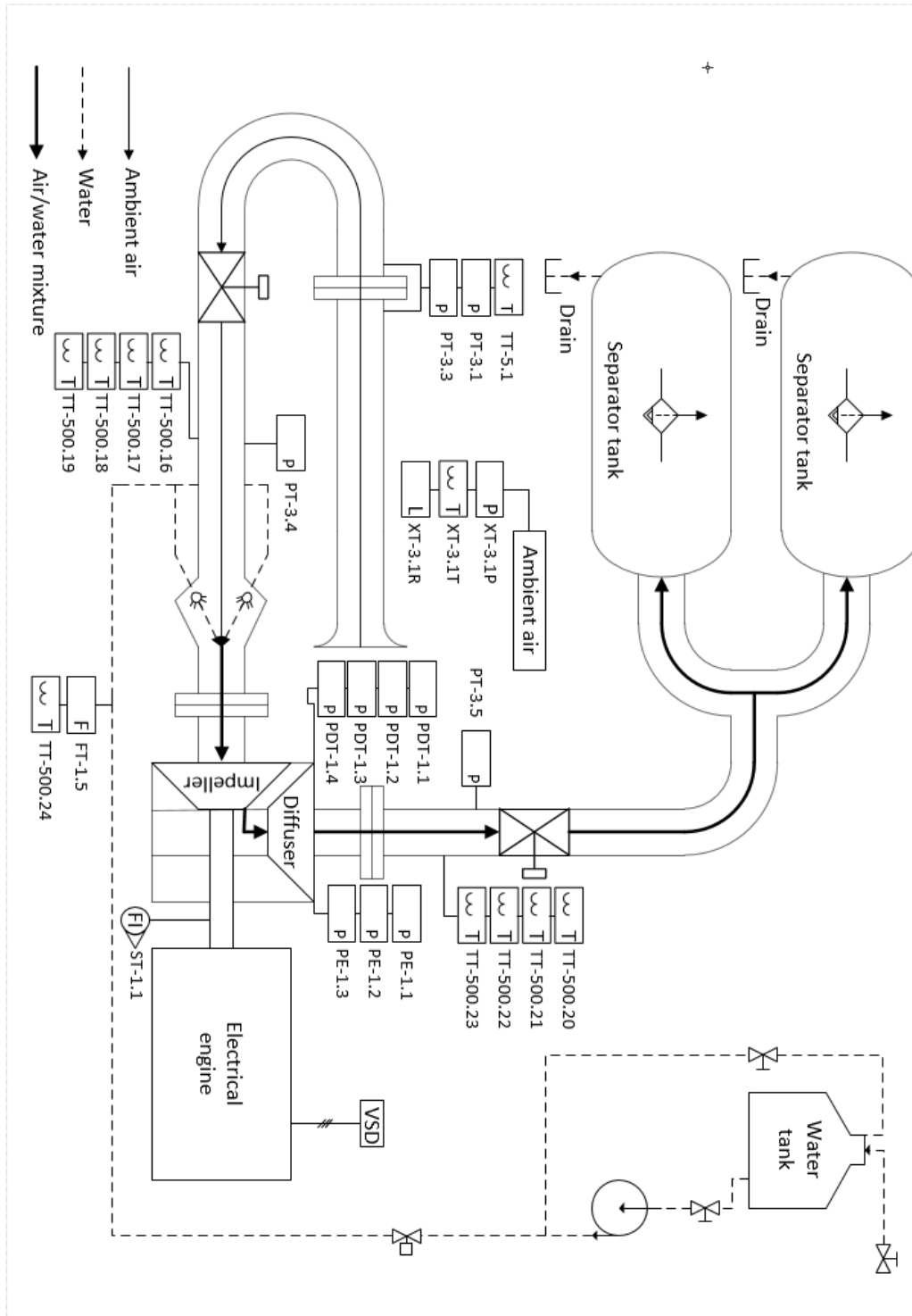
Detected diffuser flow regime is limited to observations made on the diffuser shroud wall. Further investigation to document flow angle and traverse phase behaviour is of significant importance in order to fully understand multiphase effects on diffuser flow.

The influence of labyrinth leakage on impeller inlet flow regime has been thoroughly documented in this thesis. Leakage was found to contribute to documented annulus ring formation in wet conditions. Further research is needed in order to fully understand the cause of formation. Recommended further work is removal of leakage by suction, in order to detect any changes in occurring flow phenomenon.

Part IV

APPENDIX

PIPE AND INSTRUMENTATION DIAGRAM



CALCULATIONS

B.1 MASS FLOW CALCULATION

The air flow in this thesis is calculated with an orifice plate located upstream of the compressor inlet. An orifice plate is a head-type flow meter, which causes a velocity increase in the flow by a sudden area reduction. This creates a differential static pressure, which is measurable [29]. Based on the continuity equation and the Bernoulli principle, the mass flow can be calculated from the measured differential pressure. Accounting for frictional and compressibility effects, the mass flow can be expressed as:

$$\dot{m}_{\text{air}} = C_D Y \rho_{\text{ori}} \frac{\pi}{4} D_{\text{pipe}}^2 \sqrt{\frac{2 \delta P_{\text{ori}}}{\rho_{\text{ori}}} (1 - \zeta^4)} \quad (37)$$

ζ represents the ratio of the orifice diameter to the pipe diameter and ρ_{ori} is the fluid density upstream the orifice plate. The pipe diameter is expressed as D_{pipe} and δp_{ori} is the measured differential pressure over the orifice plate. C is defined as the volume flow coefficient, accounting for frictional effects and is given by Equation 38. This is a simplification of the empirical relation provided in the ASME standard.

$$C_D = 0.5959 + 0.0312\zeta^{2.1} - 0.184\zeta^8 \quad (38)$$

The expansion factor Y takes into account the compressibility effects and is given by:

$$Y = 1 - \frac{\delta p_{\text{ori}}}{P_{\text{ori}} \kappa} (0.41 + 0.35\zeta^4) \quad (39)$$

κ denotes the specific heat ratio and P_{ori} is the static pressure upstream of the orifice plate. κ for ambient air was assumed constant, and equal to 1.4. In the authors pre project [35] the effect of varying humidity on κ was investigated. The effect was seen to be negligible.

B.2 VOLUME FLOW CALCULATION

The air volume flow is calculated from determined mass flow by the relation given in [Equation 40](#).

$$\dot{Q}_{\text{air}} = \frac{\dot{m}_{\text{air}}}{\rho_1} \quad (40)$$

ρ_1 represents the density at the compressor inlet and is given as

$$\rho_1 = \frac{P_1}{R_{\text{air}}(T_1 + 273.15)} \quad (41)$$

where P_1 is the static pressure at impeller inlet and R_{air} represents the specific gas constant for air.

B.3 NON DIMENSIONAL FLOW COEFFICIENT CALCULATION

The non dimensional flow coefficient ϕ is used for volume flow reference in this thesis, and is given by [Equation 42](#).

$$\phi = \frac{4\dot{Q}_{\text{air}}}{\pi^2 D_2^2 U_2^2} \quad (42)$$

D_2 and U_2 represents the impeller outlet diameter and the rotational velocity at impeller outlet respectively.

SENSOR ACCURACY

Every measurement has error. The error causes the measured value to deviate from the true value. In ASME PTC 19.1 Test Uncertainty [32], procedures for calculating test uncertainty are given. The difference between the measured value and the true value is called the total error. The total error ϵ_{tot} consists of two components, namely the random error ϵ_R and the systematic error ϵ_S . In Figure 63 an illustration of a normally distributed sample range with the different errors are given.

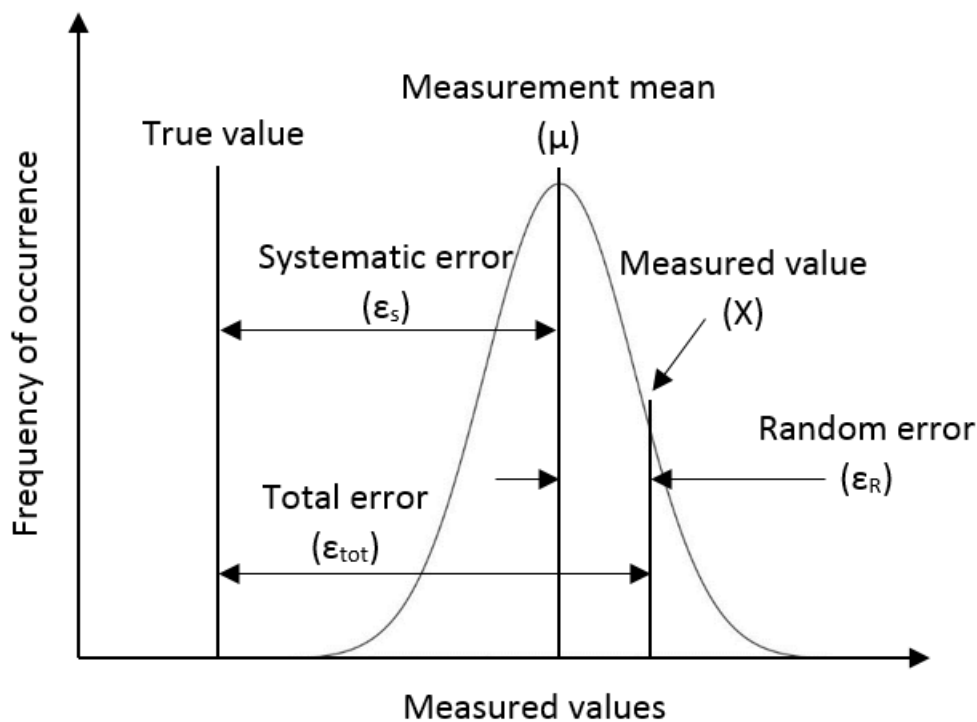


Figure 63: Illustration of measurement errors

In order to acquire accurate measurement data, both the random and the systematic error has to be minimized. The systematic error is minimised by performing through sensor calibration. The random error is more difficult to control as it usually consists of the sum of several elemental random error sources.

C.1 DIFFERENTIAL PRESSURE SENSORS

A through calibration and uncertainty analysis was performed on the GE UNIK 5000 differential pressure sensors prior to test initiation. Cali-

bration was performed using a GE Druck PACE5000 Modular Pressure Controller-Calibrator. Calibration was focused on the region between 0-100 mbar, as test readings were expected in this range. Points for the calibration curve can be found in [Table 11](#) and [Table 12](#).

Table 11: Points on calibration curve (0-100 mbar)

SENSOR	Gauge Pressure [mbar]									
PDT.1-1	0	5	10	15	20	25	30	40	50	70
PDT.1-2	0	5	10	15	20	25	30	40	50	70
PDT.1-3	0	±5	±10	±15	±20	±25	±30	±40	±50	±70
PDT.1-4	0	±5	±10	±15	±20	±25	±30	±40	±50	±70

Table 12: Points on calibration curve (100-500 mbar)

SENSOR	Gauge Pressure [mbar]				
PDT.1-1	100	200	300	400	500
PDT.1-2	100	200	300	400	500
PDT.1-3	±100	±200	±300	±400	±500
PDT.1-4	±100	±200	±300	±400	±500

Each sensor is connected to the lab PXI, and an error estimation for the whole loop is wanted. The uncertainty analysis was thus performed while reading values from the PXI, providing a combined random error estimation. In order to calculate the error, the pressure controller-calibrator was set to specific pressures, and connected to the high-pressure input of the differential pressure sensors. The pressure set on the calibrator is assumed as true pressure, allowing estimation of the systematic error. Number of readings were set to 600, ensuring a good estimation of the random error. PDT.1-1 and PDT.1-2 have a range of 0-500 mbar, and are used for velocity calculations. These are tested for increasing differential pressures, and a mean value of estimated errors will be used. PDT.1-3 and PDT.1-4 have a range of -500-500 mbar, and are used for probe alignment to the flow direction. These are tested for values close to zero, both negative and positive, and a mean of the estimated errors will be used. In [Table 13](#) the pressure values for the error estimation on each sensor are shown.

In order to calculate the sensor accuracy range, the random error ϵ_R is treated as part of the sample standard deviation σ . This means that the measured value can be said to be in the range of $-3\sigma < \mu < +3\sigma$ with a certainty of 99.73%. From [Figure 64](#) it is then clear that the total

Table 13: Error estimation pressure values

SENSOR	Gauge Pressure [mbar]		
	VALUE 1	VALUE 2	VALUE 3
PDT.1-1	0	10	20
PDT.1-2	0	10	20
PDT.1-3	-10	0	10
PDT.1-4	-10	0	10

error ϵ_{tot} can be said to be in the range of $-3\sigma < \epsilon_s < +3\sigma$, providing an estimate for the sensor accuracy.

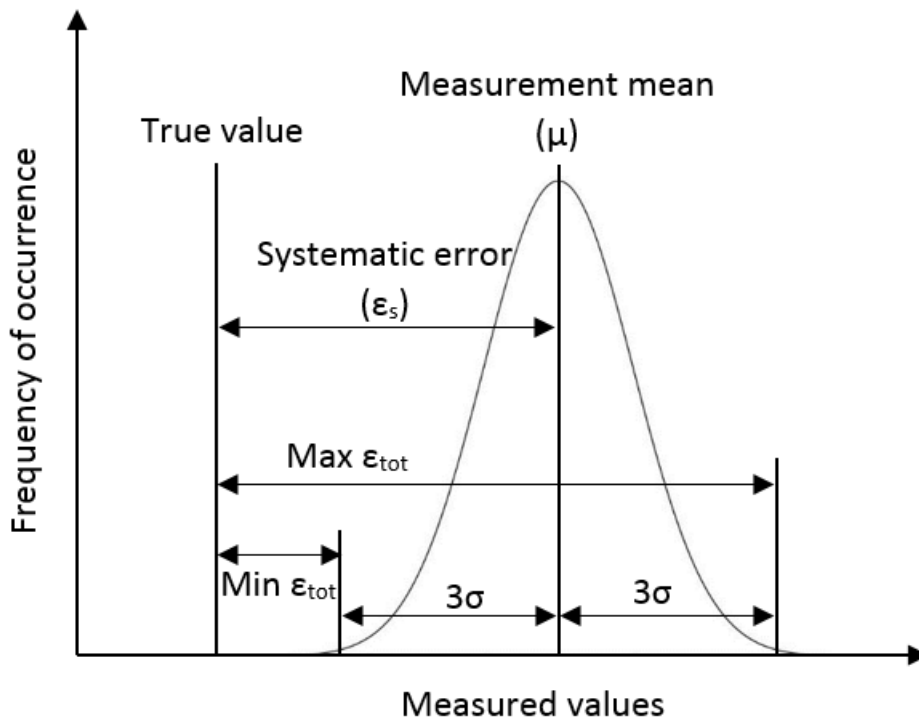


Figure 64: Illustration of measurement error range

The calculation procedure can be seen in the following equations,

$$\mu = \frac{\sum_{i=1}^N X_i}{N} \tag{43}$$

$$\sigma = \frac{\sqrt{\sum_{i=1}^N \frac{(X_i - \mu)^2}{N-1}}}{\sqrt{N}} \tag{44}$$

$$\epsilon_s = \mu - \text{True value} \tag{45}$$

where X_i represents the value of each individual measurement in the sample and N is the number of measurements in the sample. The results from the sensor accuracy test are given in [Table 14](#).

Table 14: Differential pressure accuracy test results

SENSOR	ε_S	3σ	MAX ε_{tot}	MIN ε_{tot}
PDT.1-1	-0.02 [mbar]	0.02 [mbar]	-0.04 [mbar]	0.00 [mbar]
PDT.1-2	-0.10 [mbar]	0.02 [mbar]	-0.12 [mbar]	-0.08 [mbar]
PDT.1-3	-0.22 [mbar]	0.05 [mbar]	-0.27 [mbar]	-0.17 [mbar]
PDT.1-4	-0.39 [mbar]	0.07 [mbar]	-0.46 [mbar]	-0.32 [mbar]

C.2 REMAINING SENSORS

Calibration was performed on all relevant sensors prior to test initiation. The only sensors subject for a detailed uncertainty analysis was the GE UNIK 5000 differential pressure sensors, as it was necessary to calculate error in 3-hole probe measurements. Error for remaining sensors are based on manufacturer data, and given in [Table 15](#).

Table 15: Sensor accuracy

INSTRUMENT	DESCRIPTION	RANGE	ACCURACY
KHROME OPTILUX 5000	Water flow meter	0 – 4.17L/S	$\pm 0.15\%$
Apilsen PCE 28	Water flow meter	0 – 3bar	$\pm 0.2\%$
SMAR LD-301	Static pressure	0 – 250mbar	$\pm 0.04\%$
ASL F500 (RTD)	Inlet/outlet temperature	-200 – 962°C	$\pm 0.005^\circ\text{C}$
Class A PT-100 (RTD)	Orifice inlet temperature	0 – 100°C	$\pm 0.2^\circ\text{C}$

CERTIFICATES

High resolution ICP pressure sensor calibration certificates

CALIBRATION CERTIFICATE

BS

Model: 102A05
Serial #: 32969
Description: Pressure Sensor
Type: ICP

Time Constant: 2.4 sec

Date: 9/14/2011
By: Brad Swanson, Cal. Tech.
Station: 903 Pulse #4 (Test procedure AT 601-6)

Sensitivity*: 50.59 mV/PSI
 7.338 mV/kPa

Temp: 72 deg F [22deg C]
Humidity: 43 %

Linearity*: 0.2% FS
Uncertainty:** +/- 1 %

Cert #: 410360

Bias: 10.2 VDC

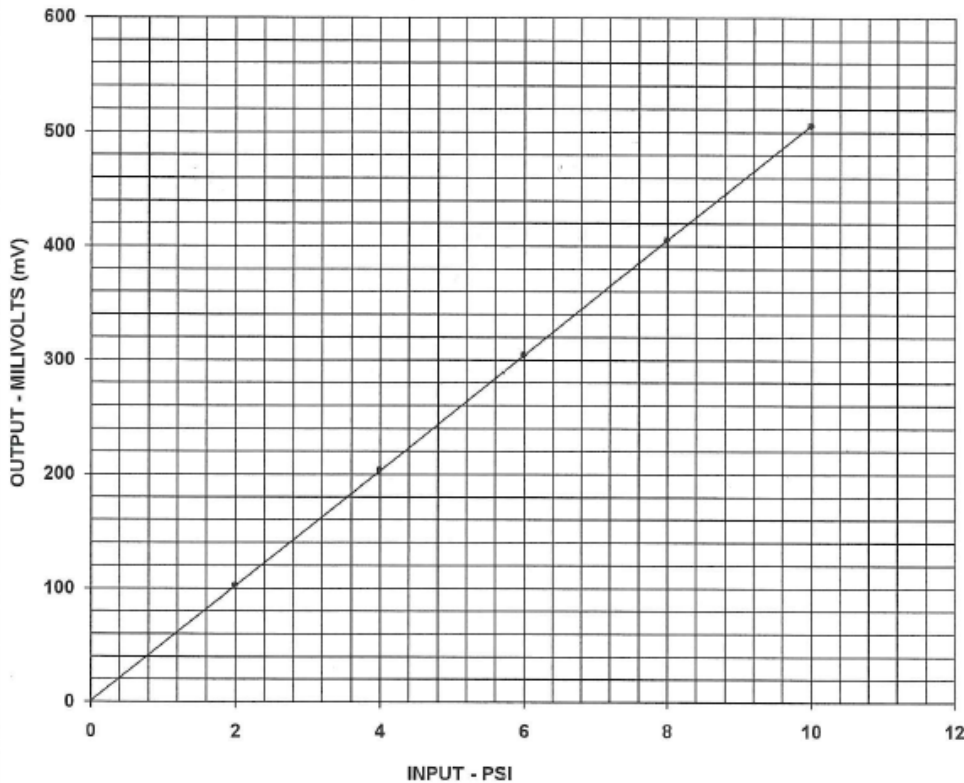
* Zero based, least-squares straight line.

** Measurement uncertainty represented using a coverage factor of k=2 which provides a level of confidence of approximately 95 %.

Condition of Unit:

As Found: Not applicable

As Left: In tolerance, new unit



TEST DATA

INPUT (PSI)	OUTPUT (mV)
2.00	102
4.00	203
6.00	304
8.00	405
10.0	505

Notes:

- 1 STATION #16
- 2 Calibration is traceable to NIST and is accredited to ISO 17025 and ANSI/NC SL Z540-1-1994.
- 3 NIST traceability through PCB control # CA 519.
- 4 This certificate may not be reproduced, except in full, without written approval from PCB Piezotronics, Inc.




CALIBRATION CERT #1862.01



Tel: 716-684-0001 Fax: 716-684-0987 Email: sales@pcb.com
 3425 Walden Avenue, Depew NY 14043

CALIBRATION CERTIFICATE

Model: 102A05
Serial #: 34435
Description: Pressure Sensor
Type: ICP

Date: 5/18/2012
By: Eric Kachermeyer, Cal. Tech 
Station: 903 Pulse #2 (Test procedure AT601-6)

Sensitivity*: 49.23 mV/PSI
 7.141 mV/kPa

Temp: 77 deg F [25deg C]
Humidity: 39 %

Linearity*: 0.3% FS
Uncertainty:** +/- 1 %

Cert #: 437278

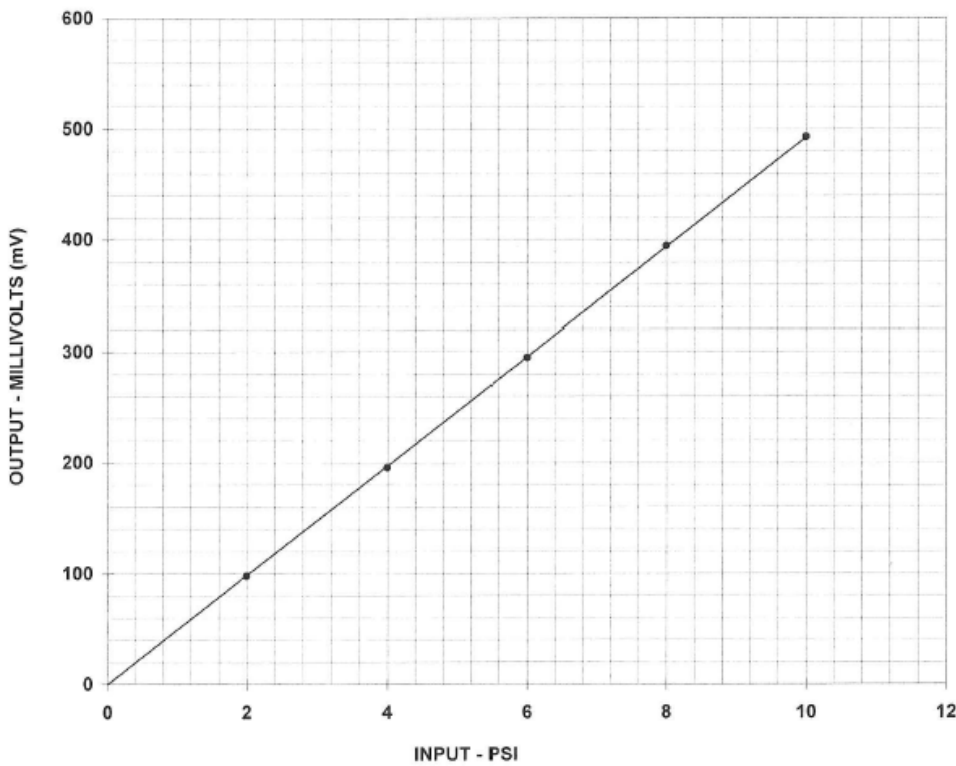
Bias: 10.4 VDC

* Zero based, least-squares straight line.

** Measurement uncertainty represented using a coverage factor of k=2 which provides a level of confidence of approximately 95 %.

Condition of Unit:

As Found: Not applicable
As Left: In tolerance, new unit



TEST DATA

INPUT (PSI)	OUTPUT (mV)
2.00	97.8
4.00	195.6
6.00	294.7
8.00	394.5
10.0	492.9

- Notes:**
- 1 STATION #17
 - 2 Calibration is traceable to NIST and is accredited to ISO 17025 and ANSI/NCCL Z540-1-1994.
 - 3 NIST traceability through PCB control # ME127.
 - 4 This certificate may not be reproduced, except in full, without written approval from PCB Piezotronics, Inc.



CALIBRATION CERT #1862.01



Tel: 716-684-0001 Fax: 716-684-0987 Email: sales@pcb.com
 3425 Walden Avenue, Depew NY 14043

GHANT CHART

Week	4	5	6	7	8	9	10	11	12	13	14	15	16	17	18	19	20	21	22	23	24
Literature review	-	-	-	-	-	-	-	-	-	-	-	-	-	-	-	-	-	-	-	-	-
-Impeller flow phenomena	X	X			X	X															
-Visualization techniques		X			X	X															
-Flow in curved channel			X	X	X	X															
-Impeller/diffuser interaction				X	X	X															
Testing				-	-	-	-	-	-	-	-	-	-	-	-	-	-	-	-	-	-
-Test design					X	X															
-Modification of test rig					X	X															
-Performing tests							X	X													
-Evaluate data							X	X	X												
-Reedo tests								X	X	X											
-Evaluate data								X	X	X											
-Tests of specific interest											X	X	X	X	X	X	X	X	X	X	X
Thesis finalization											-	-	-	-	-	-	-	-	-	-	-
-Finnish writing											X	X	X	X	X	X	X	X	X	X	X
-Feedback 1																					
-Cosmetic work and improvements																					
-Feedback 2																					
-Improvements and delivery																					
Milestones																					
-1) Finished with all testing																					
-2) Finished with first draft																					
-3) Delivery																					

EXCERPT OF RISK ASSESSMENT REPORT

Project: Wet Gas Compressor				
Node: 2 Compressor system				
Ref	Guideword	Causes	Consequences	Safeguards
1	No flow	Engine not running	None	
		Valve closed	Overtemperature	Temperature measurements with alarm and shutdown if overtemperature
		Inlet blocked	See pkt: "valve closed"	Grid in front of inlet. Control of inlet in procedure for running experiment
2	Reverse flow	Bug in program, wrong wiring.	None	Maintenance routines
3	More flow	Over speeding	Deformation of impeller	Speed limit and ramp time restrictions in VSD
4	Less flow	Ref:1		
5	More level	NA		
6	Less level	NA		
7	More pressure	Blocked outlet. Valve closed.	Ref:1 Surge. Deformation of transparent parts of diffusor	Over pressure alarm (1.7 bar) and shut down (1.8 bar) in outlet tube. FE analyses give glases at least 70 bar. Status of windows are to be checked visually before experiments.
8	Less pressure	Ref:1 and 7		
9	More temperature	Ref:1	Open hot surfaces, (< 70 °C). Overheating of acrylic windows, (70 °C).	Rig area is limited for participants to the experiment. Temperature alarms in outlet and bearings.
10	Less temperature	NA		
11	More viscosity	Inlet overfilled with water before start up. Too much water injection	Water spill, Pressure surge. Acryl windows loosen	Inspection of in and outlet in startup procedure. Not possible to water fill the diffusor more than 40%. Speed limitations in control program. Very low start up speed is demand in procedure
12	Less viscosity	NA		
13	Composition Change	NA		
14	Contamination	Rusty water, dirt and dust in inlet tube	Scratches in acrylic windows. Error in measurements. Ref:7	Maintenance procedures. Filter in water supply system. Ref 7, 11
15	Relief	Temperate air with lot of moisture from experiments.	Unfortunate influence on equipment and surroundings.	Frequently inspections.
16	Instrumentation	Unfortunate placement of sensors. Not assembled properly	Error in measurements, overloading of equipment.	Control and maintenance procedures. Manuel control of temperatures and unexpected sounds.

Project: Wet Gas Compressor				
Node: 2 Compressor system				
Ref	Guideword	Causes	Consequences	Safeguards
17	Sampling	NA		
18	Corrosion/erosion	NA		
19	Service failure	Instrumentation black out. Wire cut, vibrations, mechanical breakdown, deformed	Measurements and control system signals disappears.	Experiments will not be performed unattended. Equipment and casing are dimensioned to handle more than possible charge. Safety system is coupled in fail safe mode.
20	Abnormal operation	Emergency shutdown, electrical cut Ref:1 and node 1	None	Training of operators, maintenance procedures. Emergency shutdown is safe
21	Maintenance	Maintenance of compressor, bearings.	Not properly Assembly. Scratches in acrylic windows.	Maintenance procedures. Maintenance and inspections done by experienced operators
22	Ignition	NA		
23	Spare equipment	NA		
24	Safety	Ref: 21, 16 and node 1.		Fail safe, emergency shutdown buttons, procedures, safety gear, rig surroundings signed with related danger. Enclosed rig area. Rotating parts are covered.

BIBLIOGRAPHY

- [1] N Aretakis, K Mathioudakis, M Kefalakis, and K Papailiou. Turbocharger unstable operation diagnosis using vibroacoustic measurements. In *ASME Turbo Expo 2003, collocated with the 2003 International Joint Power Generation Conference*, pages 361–369. American Society of Mechanical Engineers, 2003.
- [2] E Ayder and R Van den Braembussche. Numerical analysis of the three-dimensional swirling flow in centrifugal compressor volutes. *Journal of turbomachinery*, 116(3):462–468, 1994.
- [3] Alessandro Bianchini, Davide Biliotti, Marco Giachi, Elisabetta Belardini, Libero Tapinassi, Lorenzo Ferrari, and Giovanni Ferrara. Some guidelines for the experimental characterization of vaneless diffuser rotating stall in stages of industrial centrifugal compressors. In *ASME Turbo Expo 2014: Turbine Technical Conference and Exposition*, pages V02DT42A028–V02DT42A028. American Society of Mechanical Engineers, 2014.
- [4] Meherwan P Boyce. *Gas turbine engineering handbook*. Elsevier, 2012.
- [5] Lars Brenne. Straight-walled diffuser performance. 2004.
- [6] Lars Brenne, Tor Bjørge, Jose L Gilarranz, J Koch, and Harry Miller. Performance evaluation of a centrifugal compressor operating under wet-gas conditions. In *Proceedings of the 34th Turbomachinery Symposium*, pages 111–120, 2005.
- [7] Lars Brenne, Tor Bjørge, Lars E Bakken, and Øyvind Hundseid. Prospects for sub sea wet gas compression. In *ASME Turbo Expo 2008: Power for Land, Sea, and Air*, pages 671–677. American Society of Mechanical Engineers, 2008.
- [8] William B Bryan and Sanford Fleeter. An investigation of unsteady impeller-diffuser interactions in a centrifugal compressor. Technical report, DTIC Document, 1992.
- [9] Nicholas A Cumpsty. *Compressor aerodynamics*. Longman Scientific & Technical, 1989.
- [10] Norwegian Petroleum Directorate. Facts 2014 - the norwegian petroleum sector. 2014.

- [11] D Eckardt. Detailed flow investigations within a high-speed centrifugal compressor impeller. *Journal of Fluids Engineering*, 98(3): 390–399, 1976.
- [12] Michelangelo Fabbrizzi, Ciro Cerretelli, Francesco Del Medico, and Maria D Orazio. An experimental investigation of a single stage wet gas centrifugal compressor. In *ASME Turbo Expo 2009: Power for Land, Sea, and Air*, pages 443–453. American Society of Mechanical Engineers, 2009.
- [13] Veronica Ferrara and Lars E Bakken. Wet gas compressor surge stability. In *ASME Turbo Expo 2015: Power for Land, Sea and Air*. American Society of Mechanical Engineers, 2015.
- [14] DA Fink, NA Cumpsty, and EM Greitzer. Surge dynamics in a free-spool centrifugal compressor system. *Journal of Turbomachinery*, 114(2):321–332, 1992.
- [15] P Frigne and R Van den Braembussche. Distinction between different types of impeller and diffuser rotating stall in a centrifugal compressor with vaneless diffuser. *Journal of Engineering for Gas Turbines and Power*, 106(2):468–474, 1984.
- [16] Jan Tommy Gravdahl and Olav Egeland. *Compressor surge and rotating stall: modeling and control*. Springer Publishing Company, Incorporated, 1999.
- [17] Trond G Grüner and Lars E Bakken. Instability characteristic of a single-stage centrifugal compressor exposed to dry and wet gas. In *ASME Turbo Expo 2012: Turbine Technical Conference and Exposition*, pages 881–890. American Society of Mechanical Engineers, 2012.
- [18] Trond G Grüner, Lars E Bakken, Lars Brenne, and Tor Bjørge. An experimental investigation of airfoil performance in wet gas flow. In *ASME Turbo Expo 2008: Power for Land, Sea, and Air*, pages 575–584. American Society of Mechanical Engineers, 2008.
- [19] Trond Gammelsæter Grüner. Wet gas compression. 2012.
- [20] Øyvind Hundseid and Lars E Bakken. Wet gas performance analysis. In *ASME Turbo Expo 2006: Power for Land, Sea, and Air*, pages 625–632. American Society of Mechanical Engineers, 2006.
- [21] Øyvind Hundseid, Lars E Bakken, Trond G Grüner, Lars Brenne, and Tor Bjørge. Wet gas performance of a single stage centrifugal compressor. In *ASME Turbo Expo 2008: Power for Land, Sea, and Air*, pages 661–670. American Society of Mechanical Engineers, 2008.

- [22] M Inoue and NA Cumpsty. Experimental study of centrifugal impeller discharge flow in vaneless and vaned diffusers. *Journal of Engineering for Gas Turbines and Power*, 106(2):455–467, 1984.
- [23] National Instruments. Fft use in ni diadem.
- [24] Marie R Jellum. Wet gas compressor stall and surge. 2012.
- [25] Blair G McLachlan and James H Bell. Pressure-sensitive paint in aerodynamic testing. *Experimental Thermal and Fluid Science*, 10(4): 470–485, 1995.
- [26] Wolfgang Merzkirch. *Flow visualization*. Elsevier, 2012.
- [27] J Moore. A wake and an eddy in a rotating, radial-flow passage part 1: Experimental observations. *Journal of Engineering for Gas Turbines and Power*, 95(3):205–212, 1973.
- [28] J Moore. A wake and an eddy in a rotating, radial-flow passage part 2: Flow model. *Journal of Engineering for Gas Turbines and Power*, 95(3):213–219, 1973.
- [29] Erik Natås. Wet gas compressor performance. 2014.
- [30] S Ohuchida, T Kawakubo, and H Tamaki. Experimental study of rotating stall in vaneless diffuser of a centrifugal compressor. In *ASME Turbo Expo 2013: Turbine Technical Conference and Exposition*, pages V06CT40A014–V06CT40A014. American Society of Mechanical Engineers, 2013.
- [31] ASME PTC. 10, 1997, performance test code on compressors and exhausters. *American Society of Mechanical Engineers, New York, New York*, .
- [32] ASME PTC. 19.1, 2005, test uncertainty. *American Society of Mechanical Engineers, New York, New York*, .
- [33] Herbert Ian Howard Saravanamuttoo, Gordon Frederick Crichton Rogers, Henry Cohen, and PV Straznicky. *Gas Turbine Theory*. Pearson Education, 2009.
- [34] Herrmann Schlichting and Klaus Gersten. *Boundary-layer theory*. Springer Science & Business Media, 2000.
- [35] Håvard S Skjefstad. Wet gas compression - surge instability. 2014.
- [36] Anish Surendran and Heuy Dong Kim. Effects of wet compression on the flow behavior of a centrifugal compressor: A cfd analysis. In *ASME Turbo Expo 2014: Turbine Technical Conference and Exposition*,

pages Vo2DT42A002–Vo2DT42A002. American Society of Mechanical Engineers, 2014.

- [37] RA Van den Braembussche and BM Hande. Experimental and theoretical study of the swirling flow in centrifugal compressor volutes. *Journal of turbomachinery*, 112(1):38–43, 1990.
- [38] Mark P Wernet, Michelle M Bright, and Gary J Skoch. An investigation of surge in a high-speed centrifugal compressor using digital piv. *Journal of turbomachinery*, 123(2):418–428, 2001.